UNIVERSITY OF CALIFORNIA,
IRVINE

Development of Novel Preclinical Models and Repair Approaches for Urogenital Tissue Reconstruction

DISSERTATION

submitted in partial satisfaction of the requirements
for the degree of

DOCTOR OF PHILOSOPHY

in Biomedical Engineering

by

Travis Nguyen

Dissertation Committee:
Associate Professor Joshua Mauney, Chair
Associate Professor Michelle Digman
Associate Professor Anna Grosberg
Assistant Professor Sadeghi Zhina
Associate Professor Tim Downing

2024

TABLE OF CONTENTS

LIST OF FIGURES

LIST OF TABLES

ACKNOWLEDGEMENTS

Throughout my time in graduate school, I was able to achieve some of my greatest accomplishments with the unwavering support of numerous people and organizations I would like to recognize. All studies would not have been completed without the financial support from the NIH's grant (R01DK119240 & R01DK131211) as well as the generous support from Randy Douthit and Jerry D. Choate Tissue Engineering Fund.

My deepest gratitude firstly goes toward my mentor, Dr. Joshua Mauney for your wonderful guidance throughout my time in your lab. All your support and candid feedback will forever be cherished as superb mentorship that contributed to me becoming the scientist I am today in the growing field of tissue engineering. The time I had with your lab throughout graduate school was nothing short of rewarding as the interpersonal skills I acquired along the way emphasized true teamwork, trust and compartmentalization in the intricate process of research. I will forever revere all the kind interactions I have had with you and wish you the best within your lab and your personal life.

I am also incredibly grateful for all the associated people that were a part of Mauney's Lab for their lab contributions of making the lab enjoyable. Thank you to the animal surgeons, Dr. Gokhan Gundogdu, Dr. David Barham and Dr. Hossein Sharifi for educating me in surgery; the lab managers, Charlotte Morgan and Stephanie Starek for your tenderness toward me and animals; the lab technicians, Kyle Costa and Faith Veneri for equipping me with skills to progress my projects; my successor, Madison Rivero for assisting me in my experiments; and the undergraduate students, Ambika Chaudhuri, Christina Bottini, Shubhang Rajpara and Hanh Nguyen for handling my projects while I'm away. Every day in the lab was full of enthusiasm and excitement with everybody involved that was unique in their own ways.

Lastly, I would like to recognize my family for their unrequited love throughout graduate school. Their unending support has provided me with a nurturing environment for me to excel in my career and reinforce my aspiration to do what I can in order to advance healthcare for humanity. My friends that are part of Amino Acids 22, Steamed Buns, Torrance Crew, Cream Pan, CSULB BUILD, UCI BME and A-Hideout were equally critical to my personal development as they encouraged me to have compassion for others, embody patience and garner perseverance throughout my arduous moments. I will invariably appreciate the myriad of social events I had with all my friends from different parts of my life with congenial sentiment.

VITA

Travis Nguyen

EDUCATION

University of California, Irvine (UCI)

Doctor of Philosophy in Biomedical Engineering — Sept 2020 – June 2024

Master of Science in Biomedical Engineering — Sept 2020 – June 2023

California State University, Long Beach (CSULB)

Bachelor of Science in Biomedical Engineering — August 2017 – May 2020

- Minor in Chemistry

Orange Coast College (OCC)

Associate in Engineering — August 2014 – May 2017

RESEARCH PUBLICATIONS

Directing Crystal Structure of Porous Inorganic Materials in Drug Releasing

- Authors: Hao Pham, Kimberly Ramos, Andy Sua, Jessica Acuna, Katazyna Slowinska, Travis Nguyen, Angela Bui, Mark D. R. Weber, Fangyuan Tian
- Journal: American Chemistry Society Omega

Iron-containing metal-organic framework thin film as a drug delivery system

- Authors: Angela Bui, Steven G. Guillen, Andy Sua, Travis Nguyen, Angel Ruiz, Lester Carachure, Mark D.R. Weber, Araseli Cortez, Fangyuan Tian
- Journal: Colloids and Surfaces A: Physicochemical and Engineering Aspects

DNA Methylation Dynamics during esophageal epithelial regeneration following repair with acellular silk fibroin grafts in rat

- Authors: Lauren A. Urban, Jiachun Li, Gokhan Gundogdu, Annie Trinh, Hanjuan Shao, Travis Nguyen, Joshua R. Mauney, Timothy L. Downing
- Journal: Advanced Biology

Evaluation of Silk Fibroin-based Urinary Conduits in a Porcine Model of Urinary Diversion

- Authors: Gokhan Gundogdu, Travis Nguyen, Seyed Hossein Sharifi, Stephanie Starek, Kyle Costa, Clara E. Jones, David Barham, Joel Gelman, Ralph Clayman, Joshua Mauney
- Journal: Biomed research International

Characterization of a Novel Rabbit Model of Peyronie's Disease

- Authors: Gokhan Gundogdu, Travis Nguyen, Aarthi Namasivayam, Stephanie Starek, Joel Gelman, Joshua Mauney

- Journal: Your Sexual Medicine Journal

Development of Male and Female Models of Long Urethral Strictures in Swine

- Authors: Gokhan Gundogdu , Travis Nguyen, Mando Eijansantos, Ambika Chaudhuri, David Barham, Joel Gelman, Joshua Mauney
- Journal: SURGERY Open Science

Evaluation of Bi-layer Silk Fibroin Grafts for Inlay Vaginoplasty in a Rat Model

- Authors: Travis Nguyen, Gokhan Gundogdu, Christina Bottini, Ambika K. Chaudhuri, Joshua R. Mauney
- Journal: Tissue Engineering and Regenerative Medicine

FELLOWSHIPS, HONORS AND AWARDS

UCI Samueli School of Engineering October 2020 – May 2021

This fellowship is a financial support for my studies. The total amount of support offered is approximately $44,504.60, consisting of: $20,083.50 in stipend for the academic year, $17,726.60 to cover all tuition, fees, and health insurance, $6,694.50 in summer 2021 stipend.

CSULB BUILD Scholar June 2018 – May 2020

(BUilding Infrastructure Leading to Diversity) is a two-year NIH-funded program designed for students who are working toward their PhD programs. As part of the second cohort, my BUILD mentor is Dr. Fangyuan Tian. Awards include $36620 for travel grant, GRE preparation, monthly stipend, tuition funding and lab funding.

SERVICES OR DEMONSTRATED COMMITMENT TO DIVERSITY

Fountain Valley Regional Hospital May 2015 – Sep 2020

Escort patients, update operation room, training, central command and take department call to send other volunteers to assist in multiple departments. Finished with exactly 1021 hours.

ABSTRACT OF THE DISSERTATION

Development of Novel Preclinical Models and Repair Approaches for Urogenital Tissue Reconstruction

by

Travis Nguyen
Doctor of Philosophy in Biomedical Engineering
University of California, Irvine, 2024
Professor Joshua Mauney, Chair

The lower urinary tract, consisting of the bladder and urethra, functions to facilitate storage and voiding of urine while maintaining low intravesical pressures to prevent renal damage. A variety of congenital and acquired pathologies including spinal cord injury and urethral stricture disease can lead to anatomical or functional obstruction of the lower urinary tract which can elevate urinary storage pressures and ultimately cause renal deterioration. In addition, malignant conditions such as bladder cancer and developmental abnormalities including bladder exstrophy can also result in tissue loss or malformed urogenital tissues which can compromise organ continuity, disrupt normal micturition, and in some cases negatively impact patient fertility. Surgical correction of urogenital defects is conventionally accomplished with autologous tissue grafts derived from extragenital sources, however this strategy is encumbered by donor site morbidity, limited tissue availability, and failure to restore native tissue functionality. Tissue engineering approaches utilizing acellular biomaterials composed of decellularized tissue grafts or synthetic polymers either alone or seeded with ex vivo expanded primary or progenitor

cell sources have been previously explored as alternatives to autologous tissue grafts for urogenital reconstruction in both preclinical studies and clinical trials. Despite the successful performance of these constructs in non diseased animal models, none of these technologies have been adopted into widespread clinical practice due to poor functional outcomes, abnormal tissue formation, and serious adverse events encountered in human studies. Clinically viable biomaterial configurations must possess optimal structural, mechanical and degradative characteristics sufficient to provide for initial defect reinforcement, but allow for gradual scaffold dissipation and subsequent formation of site-appropriate functional tissue (constructive remodeling). Moreover, validation of prospective tissue engineered implant designs in diseased animal models which mimic underlying patient pathology is necessary to accurately evaluate graft potential prior to clinical translation. Alterations in the regenerative capacity of host tissues can occur as a function of disease or past injury and can ultimately influence implant functional performance. Therefore, advancements in urinary tract reconstruction are dependent on new scaffold designs which can promote host regenerative responses in diseased settings and overcome deficiencies related to autologous tissue deployment.

The focus of my thesis is centered on 2 main areas of investigation: (1) creation of novel preclinical models of urinary tract disease for medical device testing and (2) evaluation of bi-layer silk fibroin (BLSF) grafts for urogenital tissue reconstruction. My first goal will be accomplished by developing and characterizing new rabbit and swine models which respectively recapitulate clinical phenotypes of Peyronie's disease and urethral stricture disease. My second goal will involve testing the efficacy of protein-based, BLSF grafts to serve as urinary conduits for management of bladder cancer following radical

cystectomy as well as biological substitutes for repair of focal vaginal defects and long urethra stricture defects in male and female porcine models.

Chapter 0: Prologue

0.1 Creation of Novel Preclinical Models of Urinary Tract Disease

Significance of Peyronie's Disease and Need for Improved Preclinical Models

Peyronie's disease (PD) is a benign connective tissue pathology that affects between 0.4% and 13% of the male population.[1-2] This condition can result in penile curvature and subsequent erectile dysfunction due to localized formation of fibrotic plaques in the penile tunica albuginea surrounding the corpus cavernosum.[3] The etiology of PD is poorly understood, however inflammation of the tunica albuginea in response to recurrent sexual trauma has been implicated as a putative driver of scar tissue formation and subsequent plaque development.[4] In addition, PD fibrogenesis is also exacerbated by imbalances between extracellular matrix (ECM) proteolytic enzymes including matrix metalloproteinases (MMP) and tissue inhibitors of metalloproteinases (TIMP) which lead to abnormal degradation and accumulation of ECM components within the plaque microenvironment.[5] Overall, PD is a debilitating disease which significantly impacts patient quality of life due to declines in sexual activity from pain and penile deformity as well as adverse psychological effects from disruptions in partner intimacy.[6]

Minimally invasive, first line treatment options for acute PD include intralesional injection of collagenase clostridium histolyticum (CCH) as well as penile traction

approaches.[7] The goal of these modalities is to prevent disease progression by promoting collagen degradation and remodeling within PD plaques. However, the success of penile traction is often hampered by poor patient compliance[8] and CCH administration has been reported to have limited efficacy in treating patients with extensive plaque calcification and curvature >90 degrees.[9] For chronic PD, surgical management represents the gold standard of care and involves plaque incision or partial plaque excision in combination with corporoplasty for iatrogenic defect repair and penile straightening utilizing autologous tissues or grafts from allogenic or xenogenic sources.[9-10] Unfortunately, erectile dysfunction, curvature recurrence and penile shortening represent significant adverse outcomes associated with these grafting procedures.[11-13] These studies highlight the critical need to develop new treatment options for PD as well as an increased understanding of disease mechanisms for therapeutic targeting.

Preclinical animal models of PD represent valuable tools for studying the pathophysiology of disease progression as well as provide an in vivo setting for evaluating prospective therapeutic interventions prior to human translation. Current animal models available for PD investigations are predominantly based in rats.[14] These systems involve induction of focal inflammatory events in the tunica albuginea via injection of pro-fibrotic agents such as transforming growth factor-β1 (TGF-β1), cytomodulin, fibrin or myostatin as well as surgical trauma to elicit myofibroblast differentiation and subsequent abnormal collagen deposition and elastin fiber degradation culminating in plaque development.[15-18] Unfortunately, these rodent models are limited by inconsistencies in the timing and duration of plaque formation and do not recapitulate severe penile curvature or plaque calcification observed in humans.[14] Moreover, the small size of the rat penis precludes

corporoplasty studies needed to evaluate the performance of novel surgical grafts for resolution of chronic PD following plaque excision. We have developed a new PD model in male rabbits via subtunical injection of recombinant TGF-β1 protein and characterized erectile function and histopathological outcomes following plaque formation. Rabbits are a promising species for PD evaluations since they are commonly used for penile and urethral reconstructive studies[19-20] and the size of the penis allows for targeted tunica albuginea injections of fibrotic cytokines with minimal risk of extravasation into the penile corpora. In addition, male rabbits lack a baculum[21], similar to humans and in contrast to rats[22], thus allowing for assessments of penile curvature during PD progression without mechanical resistance from rigid osseous structures.

Significance of Urethral Stricture Disease and Need for Improved Preclinical Models

Urethral stricture disease is a significant public health issue which occurs due to scarring in or around the urethra that restricts or blocks urine flow. The total cost of urethral stricture disease in the USA in 2010 was ~$300 million.[1] Patients with urethral strictures are also responsible for 5,000 hospital and 1.5 million office visits per year in the USA and are considered a vulnerable population as they experienced high rates of urinary tract infections (41%) and incontinence (11%) as sequelae of the disease.[2,3] In addition, yearly costs for health care expenditures are increased by more than $6,000 per insured individual following urethral stricture diagnosis.[3] Urethral stricture disease is also well documented to significantly reduce patient quality of life,[4] particularly in men wherein up to 44% of individuals experience sexual dysfunction.[5] Immediate family members of patients with urethral strictures are also adversely impacted by the disease with

prospective studies reporting substantial quality of life distress among respondents including sleep disturbances (56.9%), diminished social lives (43.1%), and negative effects on partner intimacy (83.9%).[6] Urethral strictures are relatively common in males (~400 per 100,000) with increased incidence after 55 years of age.[7] Men with symptomatic stricture disease will typically present with obstructive voiding symptoms such as straining, incomplete emptying, weak stream, recurrent urinary tract infections, prostatitis, epididymitis, hematuria, or bladder stones.[8] The average stricture length in men has been reported to be 4.8 cm with stricture location dispersed along the anterior (83.1%), posterior (12.3%), or pan-urethral (4.6%) segments.[9] Stricture etiologies in men include iatrogenic caused by prolonged catheterization and prior hypospadias repair; infection or inflammation due to sexually transmitted diseases or lichen sclerosis; trauma including straddle injuries or pelvic fractures; and congenital or idiopathic origins.[10] Urethral strictures in women are less frequent compared to men due to their shorter urethral length (~5 cm in women versus 20 cm in men), with a prevalence of 3–8% overall, 4–13% in women with bladder outlet obstruction (BOO),[11-14] and 0.1–1% in women with lower urinary tract voiding symptoms.[15] Women with urethral stricture disease often present with a weak stream, dribbling, recurrent urinary tract infections, pain localized to the urethra, urgency, frequency, dysuria, hesitancy, overflow urinary incontinence, urinary retention, and/or elevated postvoid residual.[16,17] Etiologies of urethral strictures in women include iatrogenic causes resulting from urogynecological procedures such as sling procedures, transvaginal urinary fistula repair, diverticulum repair, vaginal deliveries, pelvic radiation, and urethral dilation as well as chronic cystitis and urethritis, idiopathic, trauma, and inflammation.[18]

A crucial step in developing potential implant configurations for the repair of long urethral strictures is to assess their ability to promote tissue regeneration and support functional voiding in large animal models which mimic clinical phenotypes. This is important since alterations in the regenerative capacity of host tissues can occur as a function of disease or past injury and can ultimately influence implant functional performance.[19-21] Unfortunately, the vast majority of preclinical studies used to assess biomaterial potential for urethroplasty are in small scale, traumatic urethral defects created in nondiseased, male rabbit models which fail to recreate the fibrotic microenvironment and dimensions of long urethral strictures.[22,23] Moreover, no published preclinical models of female urethral strictures currently exist. Rabbit and dog models of short urethral strictures in males (~1-2 cm in length) have been produced by open surgery, electroresection using a pediatric resectoscope, and electrocoagulation with or without endoscopy.[24-29] The male rabbit urethra, composed of epithelium and corpus spongiosum, has similar histological morphology and structure to that of humans, however the penile urethra is ~3 cm long and therefore is anatomically limited in its capacity to create a 5 cm long urethral stricture encountered in patients.[30,31] Canine models do possess urethras >5 cm[27] and are potential candidates for the creation of a long urethra stricture model, however their status as companion animals raises ethical issues which restricts their widespread use in research settings.[32] We will develop and characterize both male and female porcine models of long urethral strictures (5-6 cm in length) which recapitulate histological and functional aspects of clinical pathology. We will utilize an electrocoagulation approach to induce urethral damage in swine and will monitor changes in urethral caliber as well as determine host tissue responses following injury using

histological, immunohistochemical, and histomorphometric outcome evaluations. We predict these novel models will be useful to the research community to study mechanisms of urethral stricture formation as well as vet therapeutic interventions in clinical-scale urethral defects.

0.2 Evaluation of Bi-Layer Silk Fibroin Grafts for Urogenital Tissue Reconstruction

Overview of Tissue Engineering Constructs for Urogenital Reconstruction

Numerous biomaterial constructs have been researched for their versatile properties to treat urogenital defects with the goal of reconstructing native phenotypes and functionalities.[1] Natural biomaterials including decellularized bladder matrix (BAM), urinary bladder submucosa (UBS) and SIS are deployed in surgical reconstruction as an attempt to induce vascularized and innervated neotissues. However, these conventional grafts are fraught with limitations with rates of complications can be as high as 40% in certain cases.[2] Similar to tissue grafts, chronic inflammatory responses, stricture recurrence and fistula formation were reported as adverse effects from SIS grafts.[3,4] Unfortunately with these kinds of complications, risk of implant failure primarily from foreign body reaction imply clinical translation to only be marginally successful. The root cause of why allografts exhibit complications is partially from the fabrication process. Decellularization processes require extensive use of chemical media resulting in altering the graft's structural integrity and its compatibility with the host.[5] Synthetic biomaterials that make up porous foams, meshes, matrices and hydrogels are also effective biomaterials.

However, synthetic biomaterials can only regenerate tissue structures and restore organ functions in short term cases.[6] In long term cases, deteriorating synthetic biomaterial negatively modify elasticity and porosity secondary to structural integrity.[7] Inevitably, accumulating metabolites from synthetic biomaterials will elicit chronic inflammatory responses that will display mechanical in vivo failure and negatively impact organ functionality from constant foreign body reactions. To prevent unwanted foreign body reaction, biomaterial scaffolds are seeded with cells derived from the patient to create biocompatibility with low immunogenicity. Autologous cell seeded constructs with tunable degradation release harmless metabolites without hampering scaffold properties. Fabricating cell seeded constructs are unlike synthetic and natural biomaterials. Usage of tissue biopsies and exorbitant laboratory instruments for propagating ex vivo cells to seed the scaffold is a financial obstacle for the general population rendering it not practical to adopt as the standard treatment. With varying disadvantages in synthetic, natural and cell seeded biomaterials, there is a need for alternative biomaterial constructs that can promote regeneration, be biocompatible, optimizable mechanical properties and minimize adverse drawbacks.

Protein-based, bi-layer silk fibroin (BLSF) grafts represent an ideal platform for urogenital tissue repair due to their high tensile strength and elasticity, low immunogenicity, and tunable biodegradability.[7] These matrices can be easily sutured and utilized as sheets or tubes for urinary tract reconstruction.[8,9] The structural architecture of the bi-layer matrix prevents urinary extravasation at scaffold integration sites via a fluid-tight film component, while an annealed porous foam layer supports surrounding tissue ingrowth.[7,10] Previous studies from our laboratory have demonstrated the utility of these

scaffolds for augmentation cystoplasty, urethroplasty, corporoplasty and ureteroplasty in preclinical animal models.[5,8,9,11] BLSF grafts have also been shown to promote formation of innervated, vascularized neotissues with functional contractile/relaxation properties and less inflammatory reactions compared to traditional decellularized matrices such as SIS scaffolds.[12-14]

Evaluation of silk fibroin - based urinary conduits in a porcine model of urinary diversion

Urinary diversion with autologous gastrointestinal (GI) segments represents the primary treatment option for functional renal preservation in bladder cancer patients subjected to radical cystectomy as well as in the pediatric population afflicted with spina bifida and bladder exstrophy.[1,2] Several modes of urinary diversion exist including the commonly used, incontinent ileocutaneostomy which serves as a urinary conduit with exterior skin level drainage, and continent diversions such as non-orthotopic and orthotopic approaches including neobladders.[3,4] Despite use as a front line therapy, urinary diversions are fraught with complications. Following cystectomy with urinary diversion, the early complication rate is estimated to be 50%–70%, with a 25% likelihood of readmission within 90 days, a 20% chance of intensive care unit admission, and a 3% risk of perioperative death.[5] In addition, post-operative complications related to bowel harvesting for conduit creation include anastomosis insufficiency leading to digestive fistulae, concomitant peritonitis, and sepsis which occur in 18% of patients and required re-intervention in 50% of cases.[6] Transposition of GI segments into the urinary tract following urostomy implantation is also associated with deleterious side - effects including

chronic urinary tract infections, urinary calculi, and metabolic abnormalities.[7-9] These studies highlight the significant need for the development of non-enteric, urinary diversion techniques which can overcome limitations associated with current approaches.

Over the past 15 years, tissue engineering strategies for urinary diversion have been investigated as alternatives to bowel tissue for the creation of urinary conduits.[1,2,10] Scaffold designs for tissue engineered urinary conduits (TEUC) have been primarily constructed from porous, biodegradable biomaterials capable of facilitating host tissue ingrowth from ureteral anastomotic borders. The goal of these technologies is to create durable, vascularized neotissues containing contractile smooth muscle layers and a urothelial-lined lumen sufficient to promote urine peristalsis and prevent urinary extravasation, respectively.[1,2] TEUC composed of natural biomaterials including decellularized bladder matrices, decellularized small intestinal submucosal (SIS) scaffolds, and collagen foams, as well as synthetic polymer meshes such as polyglycolic acid (PGA), poly(lactic-co-glycolic acid) (PLGA), and polypropylene meshes have been previously explored in animal models and/or clinical studies either as acellular grafts or exogenously seeded with autologous primary or stem cell sources.[11-23]

In general, preclinical assessments of cell-seeded TEUC were found to promote superior tissue regenerative responses and preserve upper urinary tract function in comparison to acellular graft configurations which routinely elicit scar tissue formation and lead to severe hydronephrosis secondary to conduit obstruction.[10,15,16] However, cell-seeded strategies require secondary surgeries and substantial laboratory infrastructure for cell isolation and expansion, respectively, which may limit their widespread adoption.[2] In

the case of urologic malignancies, urinary tract-derived, primary cell populations can also be compromised by disease and therefore unsuitable for cell-seeded, construct development.[13] Moreover, first in man trials of a TEUC composed of tubular PLGA grafts seeded with adipose mesenchymal stem cell-derived, smooth muscle cells demonstrated significant adverse events including conduit stenosis and stricture formation in half of study participants.[18,19] Given the limitations with conventional TEUC devices, we hypothesized that an acellular urinary conduit with structural, mechanical, and degradative properties sufficient to maximize host ureteral ingrowth, minimize fibrosis, and support renal function would serve as a superior candidate for urinary diversion. In the present study, we evaluated the efficacy of acellular, tubular BLSF grafts to function as urinary conduits in a porcine model of urinary diversion.

Evaluation of BLSF grafts for onlay vaginoplasty in rats.

Congenital malformations of the uterus and vagina such as Mayer-von Rokitansky-Küster-Hauser's Syndrome (MRKH), transverse vaginal septum, vaginal atresia and agenesis pose an adverse drawback in quality of life, fertility as well as genital functions and development.[1-3] Commonly known to be the second leading cause of primary amenorrhoea, MRKH syndrome occurs between one in 1500 female births to one in 4000 female births.[4] Conventional treatment for MRKH syndrome usually require reconstruction surgery to create neovagina if non invasive methods like passive dilation from Frank's method and Ingram's method display suboptimal results.[5] While reports favorably highlight passive dilation method as an effective treatment, its success primarily depends on patient's comfortability, compliance, motivation by current sexual relationship, and

constant psychological support to encourage consistent use of vagina dilator.[6] Additionally, other difficulties patients have reported includes lack of privacy, time constraints, pain and discomfort.[7] Various psychological difficulties and prolonged treatment from non-invasive methods made the surgical option more appealing.

Although surgery might appear to be an effective and straightforward resolution to reconstruct the vagina, obstacles related to psychological factors regarding psycho-sexuality still remains.[8] Resulting in emotional avoidance, patient's inadequate ability to self-manage post-surgical dilation or during vaginal dilation could potentially hinder the patient's goal of normalizing the vagina in the long run, as scarring could undermine the efficacy of future reconstruction. Surgical complications from vaginoplasty such as infections, hematoma, necrosis, fistula, urinary incontinence and vaginal stenosis still persist with incidence of up to 73% in pediatric population where stenosis is the most common issue which may lead to dyspareunia or apareunia.[9,10] Similar to issues in using vaginal dilators, incurring these complications without sufficient self-management is a risk to successfully creating the neovagina surgically.

Recent evidence in regenerative medicine suggests the incorporation of biomaterials in reconstruction surgery could minimize complication rates.[11] New tissue engineering approach to treat MRKH syndrome and other vaginal malformation uses autologous tissues to create functional neotissue as a substitute for the vagina. Numerous tissue grafts including skin grafts, decellularized matrices from intestinal mucosa, buccal mucosa and vaginal epithelia were evaluated as potential to line the pelvic canal to restore phenotypes of the vagina.[12] However, deleterious effects are to be considered when

harvesting autologous tissues for graft fabrication. Aside from only having a limited amount of tissue to use, donor site morbidity leading to patient discomfort is an ongoing issue when undergoing the tissue engineering route. These complications can be diverted by fabricating a graft that does not originate from tissues. Protein-based materials like the bi-layer silk fibroin (BLSF) grafts made of silk, is a versatile platform having extensive strength and elasticity with considerable adjustability. The matrix's architecture is optimized with a fluid-tight film to prevent fluid leakage and support tissue ingrowth at the site of integration. BLSF mediated neotissues were found to be innervated and vascularized with functional muscle properties. Displaying fewer inflammatory reactions compared to other decellularized matrices, the BLSF is a superior graft to reconstruct the vagina while also minimizing complication rates.

Chapter 1: Novel Rabbit Model of Peyronie's Disease

1.1 Objective

Our objective is to create a rabbit model Peyronie's disease and characterize the functional and histological outcomes of disease progression.

1.2 Methods

Ten adult male, New Zealand white rabbits (Western Oregon Rabbit Co. Philomath, OR USA) weighing 3.5–4 kg were randomized into three experimental cohorts including nonsurgical controls (NSC, N = 3) and those receiving subtunical injections of vehicle (N = 3) consisting of 4 mM hydrochloric acid and 1 mg/ml bovine serum albumin or recombinant human TGF-β1 protein (N = 4). Sample sizes for each group were determined based on our past reported experiments which utilized similar animal replicates per group to determine significance in quantitative assessments.[20] Rabbits were single housed postoperatively, fed with regular rabbit food and allowed free access to water throughout the study. The Institutional Animal Care and Use Committee (IACUC) of University of California, Irvine approved the study protocol (# AUP-20-077) and all experimental procedures adhered to the National Institutes of Health's Guidelines for the Care and Use of Laboratory Animals. This study was also conducted in compliance with ARRIVE guidelines (https://arriveguidelines.org).

1.2.1 Surgical Procedures

Anesthesia was induced by subcutaneous injection of 35 mg/kg Ketamine and 5 mg/kg Xylazine and maintained by isoflurane via mask inhalation. Animals were placed in a supine position and excess fur was trimmed around the genital area. The surgical field was scrubbed with povidone-iodine solution and 70% ethanol three times and sterilely draped. A 5-0 polyprolene stay suture was positioned at the tip of the distal penile skin to facilitate surgical manipulations. The skin web located between the penis and anus was divided and a ventral incision was made longitudinally between the penile skin and Buck's fascia. Subtunical injection (50 µl) of saline vehicle or TGF-β1 protein (0.5 µg, R&D Systems, Minneapolis, MN) was performed with a 30 gauge needle at a single location in the tunica albuginea ~1.5 cm above the penile radix and between the urethra and lateral neurovascular bundle (**Figure 1**). Absorbable polyglactin sutures (5-0) were then utilized to close skin incisions. Rabbits were dressed with Elizabethan collars for 5 days to avoid self-mutilation of the surgical site. For 7 days post-op, animals were evaluated daily to assess any potential surgical complications and then monitored weekly thereafter until scheduled euthanasia at 1 month. Pain management was facilitated by a single subcutaneous injection of Buprenorphine SR (0.12 mg/kg, ZooPharm, Laramie, WY, United States) immediately after the surgery as well as daily subcutaneous injections of Banamine (1 mg/kg, Merck Animal Health, Kenilworth, NJ, United States) for 3 days. Rabbits were also given subcutaneous injection of Enrofloaxacin (5 mg/kg, Baytril®100; Bayer Healthcare LLC, KA, United States) prior to surgery and for 3 days postoperatively to prevent bacterial infection.

Figure 1: Rabbit Peyronie's Disease Model

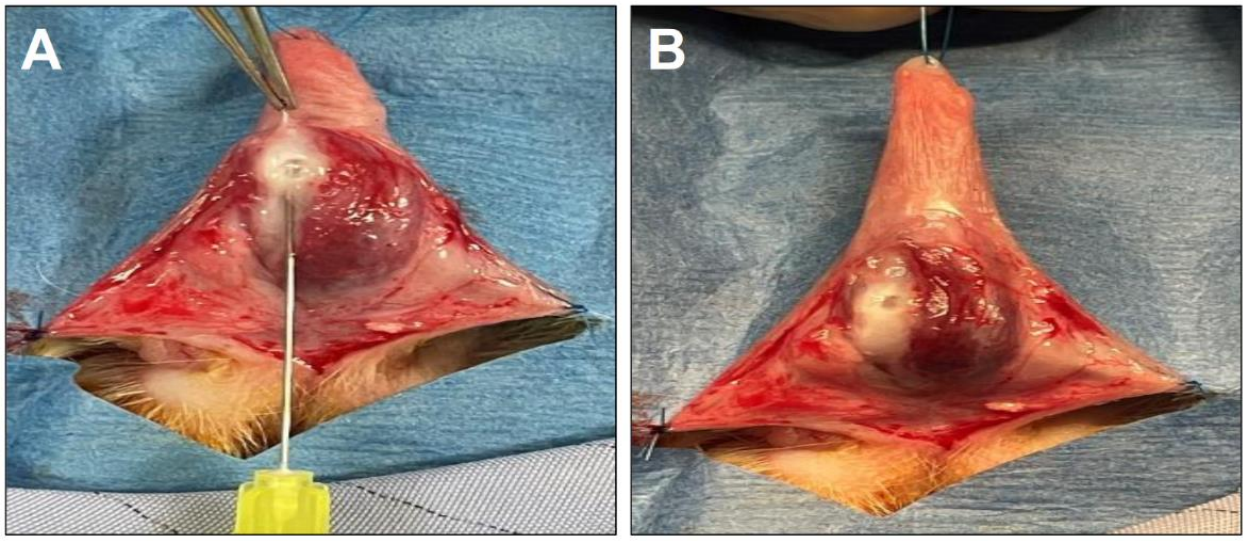

Overview of surgical stages of model creation. **[A]** Penile skin and Buck's fascia were incised longitudinally in male rabbits (N=7). A 30-gauge needle was slightly inserted into the penile tunica albuginea between the urethra and right lateral vascular structures and vehicle and TGF-β1 injections were performed. **[B]** Prominent white discoloration with central bullae were observed at injection sites of all study animals. Source: Gundogdu, Gokhan et al. International journal of impotence research vol. 36,3 (2024): 269-274. Used with permission.

1.2.2 Cavernosography and Cavernosometry

Cavernosographic and cavernosometric evaluations were performed 1 month following subtunical injections in experimental animals to assess erectile function using previously reported protocols.[20,23] Rabbits were supine positioned under general anesthesia described above and a stay suture was placed at the tip of glans. The penile skin was degloved and a 22-gauge IV catheter was inserted into the right cavernous body below the subtunical injection site at the level of penile radix. For cavernosography, contrast medium (Omnipaque 300; GE Healthcare Inc., Marlborough, MA, USA) diluted with 1:1 saline was infused into the cavernous body through the IV catheter. Serial X-ray images were acquired in the anterior/posterior and lateral directions by using a C-arm fluoroscope (BV Pulsera; Philips, Eindhoven, Netherlands) while the penis was at its maximal erection point during contrast infusion. For cavernosometry, a second 22-gauge IV catheter was inserted into the left cavernous body adjacent to the penile radix. A urodynamics system

(Goby CT; Laborie, ON, Canada) was connected to the right catheter for continuous recording of intracorporal pressures (ICP). Baseline ICP levels were recorded and then heparinized saline (10 U/ml) was infused (1 ml/min) into the corporal bodies in combination with the vasodilator, Papaverine-HCl (25 mg/ml, Sigma-Aldrich, Inc; MO, USA) to induce penile erection. Maximum ICP values were acquired and maintained for a period of 10 min with saline infusion. Photomicrographs of penile erections were captured at maximum ICP levels. Rabbits in both experimental groups as well as NSC were euthanized by intravenous injection of 0.2 ml/kg pentobarbital sodium and phenytoin sodium euthanasia solution (Euthasol; Virbac AH, Westlake, TX, USA) and tissues were collected for histological, immunohistochemical (IHC), and histomorphometric analyses.

1.2.3 Histological, Immunohistochemical, and Histomorphometric Analyses

Penile tissues harvested from NSC as well as vehicle and TGF-β1-treated cohorts following 1 month post- op were excised for routine histological procedures following animal harvest. Tissue specimens were fixed in 10% neutral-buffered formalin for 12 hours, dehydrated in graded alcohols, and paraffin embedded using standard protocols. Five micron sections were stained with Masson's trichrome (MTS) and picrosirius red (PSR) to visualize total collagen content as previously described.[24,25] Parallel sections in all groups were also evaluated for the presence of elastin fibers in control tissues and PD plaques using a commercially available, Verhoeff Van Gieson (VVG) staining kit (ab150667, Abcam, Cambridge, MA, USA). IHC evaluations were performed on tissue sections following antigen retrieval (10 mM sodium citrate buffer, pH 6.0) and incubation in phosphate-buffered saline with 0.3% Triton X-100, 5% fetal bovine serum, and 1% bovine serum

albumin for 1 hour at room temperature. Sections were then independently stained with primary antibodies including anti- collagen type I (ab34710, 1:200 dilution, Abcam), anti-collagen type III (ab7778, 1:50 dilution, Abcam), anti- MMP1 (10371-2-AP, 1:200 dilution, Proteintech, Rosemont, IL, USA), anti-MMP2 (436000, 1:150 dilution, Invitrogen, Waltham, MA), anti-MMP9 (AV33090, 1:200 dilution, Sigma-Aldrich), anti-MMP12 (22989-1-AP, 1:100 dilution, Proteintech), anti-TIMP1 (BS-0415R, 1:200 dilution, Bioss, Woburn, MA, USA), and anti- elastase 2B (orb183368, 1:100 dilution, Biorbyt, St Louis, MO, USA). Samples were then incubated with species- matched, horseradish peroxidase (HRP)-conjugated secondary antibodies and 3,3'Diaminobenzidine (DAB) substrate followed by hematoxylin counterstain. Sample visualization was performed with a Zeiss Axio Imager M2 model (Carl Zeiss MicroImaging, Thornwood, NY) and representative fields were captured with Zen software (version 3.1). Parallel specimens stained with secondary antibodies alone served as negative controls and led to no detectable background signal. For histomorphometric evaluations, quantitation of selective marker expression was calculated across 2-3 independent global sections per group replicate and displayed as a proportion of stained area per total field area examined utilizing ImageJ software. Analyses were performed with nonblinded observers.

1.2.4 Statistics

Statistical analyses of quantitative data between groups was performed using the Mann–Whitney U test considering a value of $p \leq 0.05$ as significant. Quantitative data were represented as mean ± standard deviation (SD).

1.3 Results

There were no intraoperative or immediate postoperative complications encountered in any rabbits following subtunical injections except transient mild edema and swelling in the original surgical area. Papaverine-induced, penile erectile function was assessed by cavernosography and cavernosometry in vehicle and TGF-β1-treated animals at 1 month post-op (**Figure 2**). Following injection of contrast agent, the corpora cavernosa in each group filled with fluid in a homogenous pattern resulting in an erection in the absence of leakage, filling defects or substantial curvature. Cavernosometric evaluations were performed to ascertain the maximum vascular pressure in the corpus cavernosum following papaverine-induced erection. Full erections were achieved and sustained for 10 min in all animals. No significant differences in maximum ICP values were observed between vehicle (275 ± 23 cmH2O) and TGF-β1-treated rabbits (291 ± 14 cmH2O) (Mann–Whitney U test, $p = 0.211$). These results demonstrate that subtunical TGF-β1 injections did not lead to deficiencies in papaverine-induced, erectile function during the study period.

Figure 2: Cavernosometric and Cavernosographic Assessments of Erectile Function

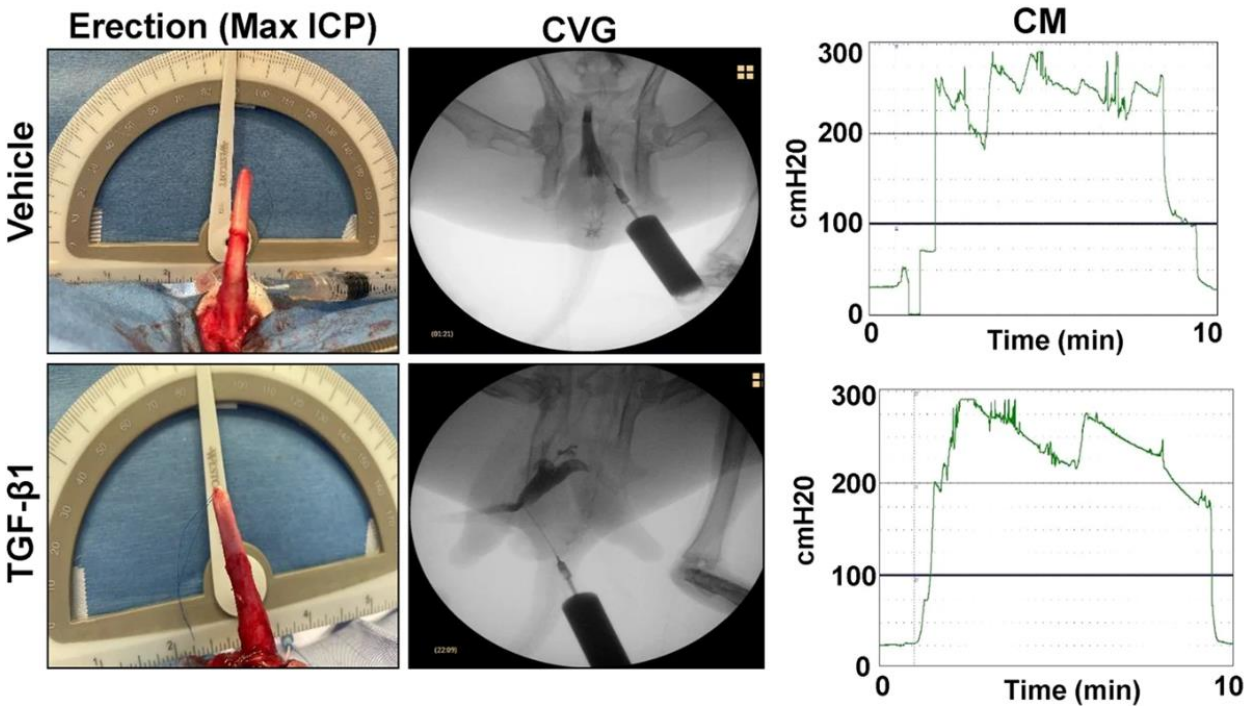

Representative photomicrographs of penile erections (first column) and cavernosographic (CVG) images (second column) at maximum intracorporal pressure (ICP) levels following contrast instillation in vehicle and TGF-β1-treated rabbits following 1 month post-op. Representative intracorporal pressure (ICP) tracings from animals described above subjected to cavernosometric analysis (CM, third column). Data are representative of N = 3–4 animals for each analysis. Source: Gundogdu, Gokhan et al. International journal of impotence research vol. 36,3 (2024): 269-274. Used with permission.

Histological (MTS, PSR, VVG), IHC and histomorphometric evaluations of the tunica albuginea in penile cross-sections from NSC as well as vehicle and TGF-β1-treated rabbits were performed to characterize levels of ECM components (collagens I and III, elastin fibers), proteolytic enzymes (MMP1, 2, 9, 12, and elastase 2B) and associated inhibitors (TIMP1). MTS (**Figure 3A**) and PSR (**Figure 3B**) analyses revealed that all rabbits treated with TGF-β1 protein displayed the formation of a focal fibrous plaque at the subtunical injection site which was composed of disorganized collagen fibrils. IHC assessments (**Figure 4**) demonstrated that fibrous plaques in the TGF-β1 group contained collagens type I and III with relative expression levels which were respectively 91% (Mann–Whitney U test, $p = 0.378$) and 80% (Mann–Whitney U test, $p = 0.00030$) of vehicle controls. In addition, quantitation of MMP/TIMP expression levels in TGF-β1 induced plaques revealed

significant reductions in MMP2 and MMP9 proteins corresponding to 54% (Mann–Whitney U test, p = 0.00000069) and 85% (Mann–Whitney U test, p = 0.0058) of vehicle controls. However, the expression patterns of MMP1, MMP12, and TIMP1 proteins were not significantly different between the cohorts (Mann–Whitney U test: MMP1, p = 0.204; MMP12, p = 0.769; TIMP1, p = 0.097). Elastin degradation (VVG) within the fibrous plaques was evident following TGF-β1 treatment with relative elastin fiber density observed at ~3% of vehicle controls (Mann–Whitney U test, p = 0.05). Elastase 2B protein expression was also significantly elevated in fibrous plaques to levels 124% relative to the vehicle group (Mann–Whitney U test, p = 0.0021). These data highlight the changes in ECM composition as well as proteolytic enzyme and inhibitor expression which occur during plaque formation following subtunical TGF-β1 injection in rabbits.

Figure 3: Histological Evaluations of Plaque Formation

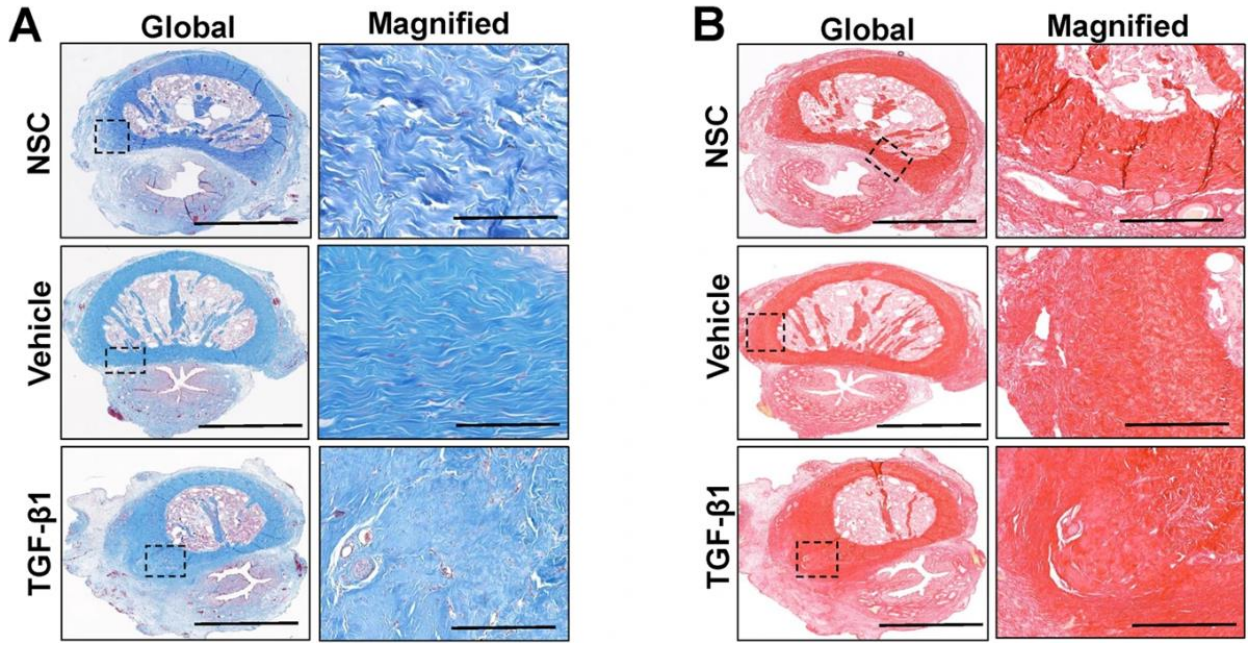

Representative photomicrographs of global and magnified rabbit penile cross-sections stained with **[A]** Masson's trichrome (MTS) or **[B]** Picrosirius red (PSR) in nonsurgical controls (NSC) as well as vehicle and TGF-β1-treated groups at 1 month post-op. Boxed areas denote magnified native and vehicle-treated tunica albuginea or fibrotic plaques induced by TGF-β1 injection. Scale bars for photomicrographs in global and magnified panels are 3 mm and

400 µm, respectively. Data are representative of N = 3–4 animals per group. Source: Gundogdu, Gokhan et al. International journal of impotence research vol. 36,3 (2024): 269-274. Used with permission.

Figure 4: Immunohistochemical and Histomorphometric Analyses of ECM Components and Proteolytic Enzymes in Vehicle and TGF-β1-treated Specimens

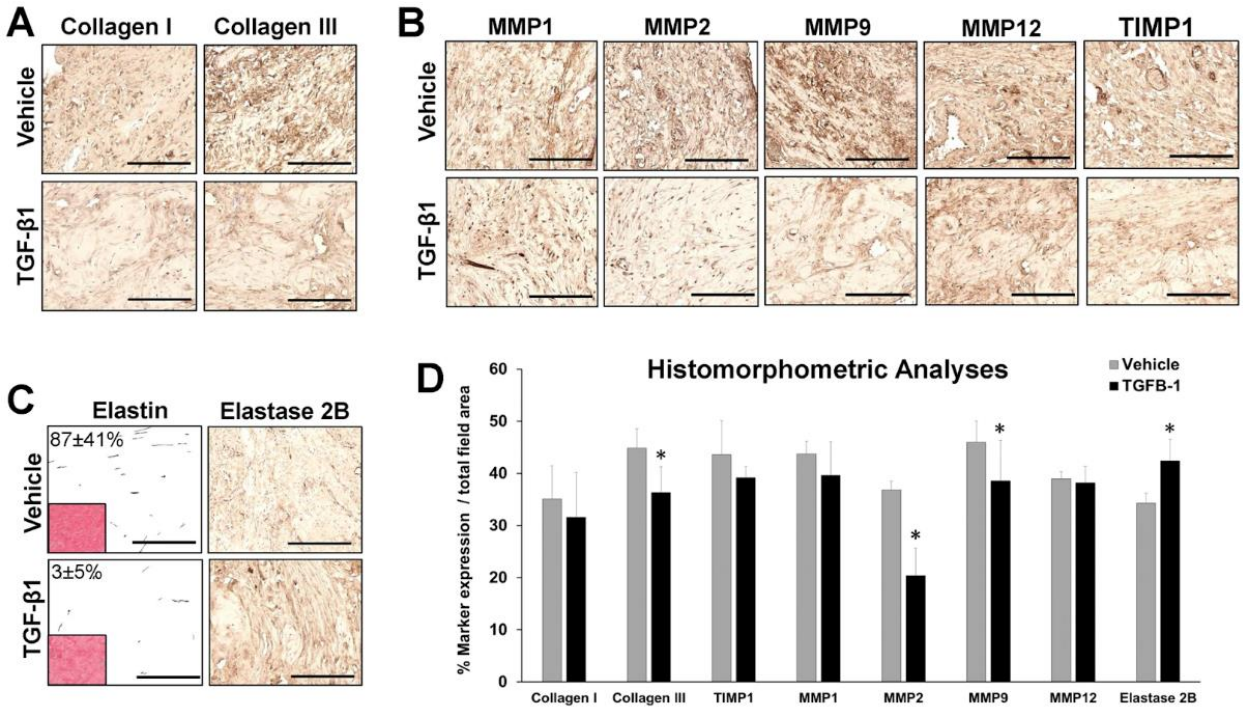

Representative photomicrographs of collagen I and III expression **[A]** as well as associated proteolytic enzymes (MMP) and their inhibitors (TIMP) **[B]** in the penile tunica albuginea of vehicle-treated samples and TGF-β1-induced plaques. Marker expression is denoted in brown (HRP labeling). **[C]** Relative elastin fiber density (VVG stain, inset; grayscale converted fibers) and elastase 2B expression (HRP labeling) in samples described in **[A-B]**. Scale bars for all panels in **[A-C]** are 400 µm. **[D]** Quantitative assessments of marker expression described in **[A–C]**. *p ≤ 0.05 in comparison to respective vehicle controls. N = 3–4 samples per data point. Results from all groups were analyzed with the Mann–Whitney U test. Values displayed as means ± SD. Source: Gundogdu, Gokhan et al. International journal of impotence research vol. 36,3 (2024): 269-274. Used with permission.

1.4 Discussion

The goal of this study was to create a novel rabbit model of PD and to characterize the functional and histological changes which occur in the penis during fibrotic remodeling of the tunica albuginea in response to TGF-β1 treatment. The choice to utilize TGF-β1 protein as a disease inducer was based on previous observations demonstrating this pro-fibrotic cytokine is overexpressed in human PD lesions.[15] In addition, overactivation of TGF-β1 signaling seems to be a pathogenetic factor in the development of PD since the

expression and activity of TGF-β1-induced Smad transcription factors is increased in fibroblasts of patients with PD.[26] Moreover, subtunical injection of TGF-β1 protein also leads to the formation of PD plaques in rats[14, 27], while regression of these lesions can be achieved through inhibition of TGF-β1 type I receptor activation.[28, 29] In response to repeated sexual trauma, TGF-β1 signaling in combination with oxidative stress[30] and platelet and coagulation pathway activation[31] serve as major regulators of fibrotic and inflammatory processes governing plaque development in PD.[32]

Our results demonstrated the formation of focal fibrous plaques composed of disorganized collagen type I and III bundles as well as fragmented elastin fibers at TGF-β1 injection sites following 1 month post-op. These histopathological features were similar to those previously observed in human PD plaques which display significant elastin fiber degradation as well as fenestration and disorganization of collagen bundles.[15, 33] However, there was no detectable plaque calcification or apparent penile curvature in TGF-β1-treated specimens as previously observed in patients with chronic PD[34] suggesting our model system leads to acute disease progression. Past studies have demonstrated that repeated subtunical injection of adenovirus expressing TGF-β1 in rodents results in features reminiscent of chronic PD including severe penile deformities and calcified plaques.[35] Therefore, future experiments will investigate the ability of recurrent subtunical injections of TGF-β1 protein in rabbits to induce a chronic PD phenotype.

Erectile dysfunction secondary to PD in humans is often a consequence of plaque-associated, penile structural alterations and/or corporal veno-occlusive abnormalities which lead to disruptions in normal penile hemodynamics during sexual activity.[36,37]

Evaluation of papaverine-induced, penile erectile function in TGF-β1-treated rabbits revealed no filling defects or significant differences in maximum ICP values in comparison to vehicle controls. These results are consistent with a lack of corporal fibrosis and severe penile angulation in the TGF-β1-treated cohort. In rat models of PD, TGF-β1-induced fibrotic plaques extend into cavernosal tissues and mitigate peak ICP values during erectile stimulation via excessive ECM deposition and loss of smooth muscle cells in the corpus cavernosa.[38] However, this situation is markedly different in humans afflicted with PD wherein corporal fibrosis is rare and plaques are normally sequestered in the tunica albuginea.[39] Due to the relatively small size of the rat penis, corporal fibrosis in rat PD models is likely due to imprecise injection of TGF-β1 into the subtunical space which then permeates into the corpus cavernosa activating myofibroblasts and aberrant ECM formation. In contrast, the larger size of the rabbit penis in our PD model allows for more accurate targeting of the tunica albuginea for pathological insult without compromising the integrity of corpus cavernosa. Therefore, our rabbit model has the potential advantage of decoupling corporal fibrosis from plaque development allowing for direct assessments of the impact of PD on erectile function. Moreover, the dimensions of the rabbit phallus also allow for corporoplasty procedures to be performed with autologous tissue grafts or tissue engineered constructs[20] to vet prospective repair strategies for PD patients who fail to respond to minimally invasive treatment approaches. This feature highlights another potential attribute of using rabbits to develop a PD model in comparison to rats wherein the small size of the penis precludes therapeutic graft screening in the latter.

Plaque fibrosis in PD is a consequence of dysregulation of ECM proteolytic enzymes and their inhibitors which leads to aberrant ECM production and subsequent scar tissue

formation. Previous profiling studies of human PD plaques has revealed increases in collagen types I and III with concurrent reductions in elastin fiber density relative to healthy tissues.[40-43] The putative cause for excessive collagen accumulation in PD patients has been linked to alterations in the balance between MMP/TIMP activities in the plaque microenvironment wherein increases in TIMP expression occur in the absence of perturbations of MMP family members thus favoring collagen stability.[43, 44] In our model, no significant increases in collagen types I and III were detected in TGF-β1-induced plaques relative to controls despite significant reductions in MMP2 and MMP9 expression in the diseased cohort. The absence of significant increases in TIMP1 expression in TGF-β1-treated rabbits over control levels may explain the lack of collagen accumulation in these specimens. The discrepancy in collagen and MMP/TIMP variations observed in human and rabbit PD lesions may reflect different states of disease progression since analysis of clinical specimens is often performed on patients with advanced disease following corporoplasty.[43 ,44] In contrast, our data did reflect a significant upregulation of elastase 2B in the TGF-β1 cohort in comparison to controls which may explain the reductions in elastin fiber density in this group. Indeed, enrichment of elastase 2B has been previously identified in gene expression screens of human PD plaques[45] and degradation and disorganization of elastin fiber networks are known to contribute to scar tissue development in skin diseases.[46] Taken together, activation of elastase 2B and subsequent degradation of elastin fibers in the tunica albuginea may play a more pronounced role in acute phases of PD plaque formation than MMP/TIMP dysregulation.

There were several key limitations in our experimental design which will be addressed in future studies. Although papaverine-induced, cavernosometric and

cavernosometric assessments revealed no detectable penile anomalies following TGF-β1 treatment, our assay methodology was not physiological in nature. Therefore, validation of in vivo erectile function with ICP normalized to mean arterial pressure following electrical stimulation of the cavernosal nerve is needed for further characterization.[47] In addition, one month following TGF-β1 injection, endpoint analyses revealed our rabbit PD model primarily mimicked acute stages of plaque formation without evidence of tunica albuginea calcification or serve angulation seen in chronic pathologies. Improvements in our rabbit PD model will focus on delineating experimental conditions such as frequency, dose, and duration of subtunical fibrotic insults which can promote further disease development into severe phenotypes for potential therapeutic testing.

In summary, we have established a new model of PD in rabbits wherein subtunical injection of TGF-β1 protein leads to the formation of fibrotic plaques reminiscent of acute stages of human pathology. Our results demonstrate that elevations in elastase 2B expression and elastin fiber degradation are significantly associated with initial plaque development and may represent potential therapeutic targets for disease intervention. Future investigations will focus on the efficacy of elastase inhibitors to mitigate TGF-β1-induced plaques in rabbits.

1.5 References

1) Carson, Culley C, and Laurence A Levine. “Outcomes of surgical treatment of Peyronie's disease.” BJU international vol. 113,5 (2014): 704-13. doi:10.1111/bju.12565

2) Ziegelmann, Matthew J et al. “Restoration of Penile Function and Patient Satisfaction with Intralesional Collagenase Clostridium Histolyticum Injection for Peyronie's Disease.” The Journal of urology vol. 195,4 Pt 1 (2016): 1051-6. doi:10.1016/j.juro.2015.10.065

3) Langston, Joshua P, and Culley C Carson 3rd. “Peyronie's disease: review and recent advances.” Maturitas vol. 78,4 (2014): 341-3. doi:10.1016/j.maturitas.2014.05.024

4) Jarow, J P, and F C Lowe. “Penile trauma: an etiologic factor in Peyronie's disease and erectile dysfunction.” The Journal of urology vol. 158,4 (1997): 1388-90. doi:10.1016/s0022-5347(01)64222-8

5) Krakhotkin, Denis V et al. “New insights into the pathogenesis of Peyronie's disease: A narrative review.” Chronic diseases and translational medicine vol. 6,3 165-181. 27 Jul. 2020, doi:10.1016/j.cdtm.2020.06.001

6) Goldstein, Irwin et al. “The Impact of Peyronie's Disease on the Patient: Gaps in Our Current Understanding.” Journal of sex & marital therapy vol. 42,2 (2016): 178-90. doi:10.1080/0092623X.2014.985351

7) Levine, Laurence A, and Stephen M Larsen. “Surgery for Peyronie's disease.” Asian journal of andrology vol. 15,1 (2013): 27-34. doi:10.1038/aja.2012.92

8) Valenzuela, Robert et al. “The use of penile traction therapy in the management of Peyronie's disease: current evidence and future prospects.” Therapeutic advances in urology vol. 11 1756287219838139. 29 Mar. 2019, doi:10.1177/1756287219838139

9) Capoccia, Edward, and Laurence A Levine. “Contemporary Review of Peyronie's Disease Treatment.” Current urology reports vol. 19,7 51. 17 May. 2018, doi:10.1007/s11934-018-0800-5

10) Levine, Laurence A. “Partial plaque excision and grafting (PEG) for Peyronie's disease.” The journal of sexual medicine vol. 8,7 (2011): 1842-5. doi:10.1111/j.1743-6109.2011.02370.x

11) Taylor, Frederick L, and Laurence A Levine. “Surgical correction of Peyronie's disease via tunica albuginea plication or partial plaque excision with pericardial graft: long-term follow up.” The journal of sexual medicine vol. 5,9 (2008): 2221-8; discussion 2229-30. doi:10.1111/j.1743-6109.2008.00941.x

12) Usta, Mustafa F et al. “Patient and partner satisfaction and long-term results after surgical treatment for Peyronie's disease.” Urology vol. 62,1 (2003): 105-9. doi:10.1016/s0090-4295(03)00244-9

13) Montorsi, F et al. “Evidence based assessment of long-term results of plaque incision and vein grafting for Peyronie's disease.” The Journal of urology vol. 163,6 (2000): 1704-8.

14) Chung, E et al. “Rat as an animal model for Peyronie's disease research: a review of current methods and the peer-reviewed literature.” International journal of impotence research vol. 23,6 (2011): 235-41. doi:10.1038/ijir.2011.36

15) El-Sakka, A I et al. “An animal model of Peyronie's-like condition associated with an increase of transforming growth factor beta mRNA and protein expression.” The Journal of urology vol. 158,6 (1997): 2284-90. doi:10.1016/s0022-5347(01)68236-3

16) Bivalacqua, T J et al. “A rat model of Peyronie's disease associated with a decrease in erectile activity and an increase in inducible nitric oxide synthase protein expression.” The Journal of urology vol. 163,6 (2000): 1992-8.

17) Davila, H H et al. “Fibrin as an inducer of fibrosis in the tunica albuginea of the rat: a new animal model of Peyronie's disease.” BJU international vol. 91,9 (2003): 830-8. doi:10.1046/j.1464-410x.2003.04224.x

18) Cantini, Liliana P et al. “Profibrotic role of myostatin in Peyronie's disease.” The journal of sexual medicine vol. 5,7 (2008): 1607-22. doi:10.1111/j.1743-6109.2008.00847.x

19) Algarrahi, Khalid et al. “Repair of injured urethras with silk fibroin scaffolds in a rabbit model of onlay urethroplasty.” The Journal of surgical research vol. 229 (2018): 192-199. doi:10.1016/j.jss.2018.04.006

20) Gundogdu, Gokhan et al. “Evaluation of Bi-Layer Silk Fibroin Grafts for Penile Tunica Albuginea Repair in a Rabbit Corporoplasty Model.” Frontiers in bioengineering and biotechnology vol. 9 791119. 7 Dec. 2021, doi:10.3389/fbioe.2021.791119

21) Skonieczna, Joanna et al. “Histological and morphometric evaluation of the urethra and penis in male New Zealand White rabbits.” Anatomia, histologia, embryologia vol. 50,1 (2021): 136-143. doi:10.1111/ahe.12611

22) Goyal, H O et al. “Abnormal morphology of the penis in male rats exposed neonatally to diethylstilbestrol is associated with altered profile of estrogen receptor-alpha protein, but not of androgen receptor protein: a developmental and immunocytochemical study.” Biology of reproduction vol. 70,5 (2004): 1504-17. doi:10.1095/biolreprod.103.026328

23) Chen, Kuo-Liang et al. “Bioengineered corporal tissue for structural and functional restoration of the penis.” Proceedings of the National Academy of Sciences of the United States of America vol. 107,8 (2010): 3346-50. doi:10.1073/pnas.0909367106

24) Junqueira, L C et al. “Picrosirius staining plus polarization microscopy, a specific method for collagen detection in tissue sections.” The Histochemical journal vol. 11,4 (1979): 447-55. doi:10.1007/BF01002772

25) Davis, C J Jr. “The microscopic pathology of Peyronie's disease.” The Journal of urology vol. 157,1 (1997): 282-4.

26) Haag, Simone M et al. “Alterations in the transforming growth factor (TGF)-beta pathway as a potential factor in the pathogenesis of Peyronie's disease.” European urology vol. 51,1 (2007): 255-61. doi:10.1016/j.eururo.2006.05.002

27) Gokce, A et al. “Adipose tissue-derived stem cell therapy for prevention and treatment of erectile dysfunction in a rat model of Peyronie's disease.” Andrology vol. 2,2 (2014): 244-51. doi:10.1111/j.2047-2927.2013.00181.x

28) Piao, Shuguang et al. “Transforming growth factor (TGF)-β type I receptor kinase (ALK5) inhibitor alleviates profibrotic TGF-β1 responses in fibroblasts derived from Peyronie's plaque.” The journal of sexual medicine vol. 7,10 (2010): 3385-95. doi:10.1111/j.1743-6109.2010.01753.x

29) Ryu, Ji-Kan et al. “IN-1130, a novel transforming growth factor-beta type I receptor kinase (activin receptor-like kinase 5) inhibitor, promotes regression of fibrotic plaque and

corrects penile curvature in a rat model of Peyronie's disease." The journal of sexual medicine vol. 6,5 (2009): 1284-96. doi:10.1111/j.1743-6109.2009.01216.x

30) Sikka, S C, and W J G Hellstrom. "Role of oxidative stress and antioxidants in Peyronie's disease." International journal of impotence research vol. 14,5 (2002): 353-60. doi:10.1038/sj.ijir.3900880

31) Gonzalez-Cadavid, Nestor F, and Jacob Rajfer. "Mechanisms of Disease: new insights into the cellular and molecular pathology of Peyronie's disease." Nature clinical practice. Urology vol. 2,6 (2005): 291-7. doi:10.1038/ncpuro0201

32) Zhang, Fuxun et al. "Molecular Mechanisms and Current Pharmacotherapy of Peyronie's Disease: A Review." Frontiers in pharmacology vol. 12 643641. 20 May. 2021, doi:10.3389/fphar.2021.643641

33) Moreland, R B, and A Nehra. "Pathophysiology of Peyronie's disease." International journal of impotence research vol. 14,5 (2002): 406-10. doi:10.1038/sj.ijir.3900875

34) Wymer, Kevin et al. "Plaque Calcification: An Important Predictor of Collagenase Clostridium Histolyticum Treatment Outcomes for Men With Peyronie's Disease." Urology vol. 119 (2018): 109-114. doi:10.1016/j.urology.2018.06.003

35) Piao, Shuguang et al. "Repeated intratunical injection of adenovirus expressing transforming growth factor-beta1 in a rat induces penile curvature with tunical fibrotic plaque: a useful model for the study of Peyronie's disease." International journal of andrology vol. 31,3 (2008): 346-53. doi:10.1111/j.1365-2605.2007.00780.x

36) Gasior, B.L., Levine, F.J., Howannesian, A. et al. Plaque-associated corporal veno-occlusive dysfunction in idiopathic Peyronie's disease: A pharmacocavernosometric and pharmacocavernosographic study. World J Urol 8, 90–96 (1990). https://doi.org/10.1007/BF01576355

37) Levine, L A, and K C Latchamsetty. "Treatment of erectile dysfunction in patients with Peyronie's disease using sildenafil citrate." International journal of impotence research vol. 14,6 (2002): 478-82. doi:10.1038/sj.ijir.3900912

38) Li, Jinhong et al. "Reduction in Peyronie's-like plaque size using a vacuum erection device in a rat model of Peyronie's disease via the TGF-β/SMAD signalling pathway." Andrologia vol. 50,7 (2018): e13051. doi:10.1111/and.13051

39) Ro JY, Divatia MK, Kim KR, Amin MB, Ayala AG. Penis and scrotum. In: Cheng L, MacLennan GT, Bostwick DG, editors. Urologic surgical pathology. 4th ed. Philadelphia: Elsevier; 2020. p. 853–901.

40) Chiang, P H et al. "Study of the changes in collagen of the tunica albuginea in venogenic impotence and Peyronie's disease." European urology vol. 21,1 (1992): 48-51. doi:10.1159/000474800

41) Brock, G et al. "The anatomy of the tunica albuginea in the normal penis and Peyronie's disease." The Journal of urology vol. 157,1 (1997): 276-81.

42) Ten Dam, Evert-Jan P M et al. “Glimpses into the molecular pathogenesis of Peyronie's disease.” The aging male : the official journal of the International Society for the Study of the Aging Male vol. 23,5 (2020): 962-970. doi:10.1080/13685538.2019.1643311

43) Del Carlo, Marcello et al. “Differential calcium independent regulation of matrix metalloproteinases and tissue inhibitors of matrix metalloproteinases by interleukin-1beta and transforming growth factor-beta in Peyronie's plaque fibroblasts.” The Journal of urology vol. 179,6 (2008): 2447-55. doi:10.1016/j.juro.2008.01.093

44) Watanabe, Marcelo Silva et al. “Extracellular matrix alterations in the Peyronie's disease.” Journal of advanced research vol. 8,4 (2017): 455-461. doi:10.1016/j.jare.2017.06.004

45) Magee, Thomas R et al. “Gene expression profiles in the Peyronie's disease plaque.” Urology vol. 59,3 (2002): 451-7. doi:10.1016/s0090-4295(01)01578-3

46) Baumann, Leslie et al. “Clinical Relevance of Elastin in the Structure and Function of Skin.” Aesthetic surgery journal. Open forum vol. 3,3 ojab019. 14 May. 2021, doi:10.1093/asjof/ojab019

47) Traish, A M et al. “Effects of castration and androgen replacement on erectile function in a rabbit model.” Endocrinology vol. 140,4 (1999): 1861-8. doi:10.1210/endo.140.4.6655

Chapter 2: Novel Porcine Models of Long Urethral Strictures

2.1 Objective

The objective of this study is to create novel male and female models of long urethral strictures for vetting prospective scaffold designs for urethroplasty.

2.2 Methods

Surgical, imaging and animal husbandry protocols were reviewed and approved by the University of California, Irvine Animal Care and Use Committee in accordance with protocol AUP-19-150. All animal procedures were carried out in compliance with the National Institutes of Health's Guidelines for the Care and Use of Laboratory Animals and ARRIVE guidelines (https://arriveguidelines.org). Creation of long urethra stricture was performed in five adult male, Yucatan mini-swine and short urethra stricture was performed on five adult female, Yucatan mini-swine (~24 weeks of age, 30–40 kg, Premier BioSource, Ramona, CA) utilizing a electrocoagulation setting of the collins knife to create the electro resection injury. Prior to operative manipulations, animals were withheld food for a minimum of 12 hours with free access to water. General anesthesia was induced by intramuscular injections of 0.4 mg/kg atropine, 2.2 mg/kg Anased (Lloyd Inc.; IA, United States), and 4.4 mg/kg Telazol (Zoetis Inc.; Parsippany, NJ, United States) and maintained with 1–4% isoflurane inhalation following endotracheal intubation. Animals were then

fixed in the supine or prone position with the hair around the urethra trimmed and the skin scrubbed with povidone iodine and 70% ethanol three times and draped sterilely.

2.2.1 Animals and Surgical Manipulations

Four castrated male (Pigs 1-4 M) and four female (Pigs 1-4F) adult Yucatan mini-swine (~24 weeks of age, 30–40 kg, PremierBioSource, Ramona, CA) were subjected to vesicostomy creation as well as urethral electrocoagulation injury for formation of long urethral strictures using the methods described below.

2.2.2 Vesicostomy

Prior to surgery, both male and female animals were fasted overnight and permitted free allowance of water. General anesthesia was initiated by intramuscular injection of 2.2 mg/kg Anased (Lloyd Inc.; IA, United States) and 4.4 mg/kg Telazol (Zoetis Inc.; Parsippany, NJ, United States), and continued by endotracheal 1–4 % isoflurane inhalation. Swine were supine positioned for creation of the vesicostomy opening. The lower abdomen was scrubbed with betadine and 70 % ethanol and covered with a sterile drape. A vertical paramedian incision (3–10 cm in length) was made on the right lower abdominal wall skin and layers were dissected separately to access the abdominal cavity. The bladder dome was grasped with forceps and suspended with stay sutures. A second 5 mm vertical incision positioned 2 cm below the first incision was made and a 22 French Foley catheter was inserted through this orifice into the abdomen. A 1 cm opening was created in the bladder dome and the Foley catheter was introduced into the bladder, followed by filling the balloon with 20 ml saline and subsequently the stoma was closed with 2 purse strings. The bladder was then anchored to the abdominal wall at the vesicostomy site with three 4–

0 polyglactin sutures to prevent detachment. Abdominal wall layers and skin incisions were suture closed. The foley catheter was then anchored to the lateral abdominal wall with multiple non-absorbable sutures and fitted with one way check valves (Heimlich, Mila Int. Inc., Florence, KY, United States) to allow for external urine flow.

2.2.3 Urethral Injury

Following vesicostomy creation, electrocoagulation was performed to induce luminal urethral damage and promote stricture formation in both sexes. For male swine, the animals were kept in the supine position and a 1–2 cm vertical skin incision was made below the urethral opening to expose the distal penile shaft. The glans was manually extruded from the foreskin and a 9.5 French rigid cystoscope (Karl Storz 27,030 KB Pediatric Operating Cysto-Urethroscope; Tuttlingen, Germany) was advanced through the urethral meatus. Normal urethral anatomy and length was confirmed using imaging modalities detailed below. Under direct visualization, a 6 cm long and 2–3 mm wide electrocoagulation injury was made from the 3–9 o'clock position ~2 cm proximal to the external meatus in the anterior urethral spongiosum using a bugbee electrode from the cystoscope. Two small incisions were made on the skin over the penile body and the injury borders were marked with subcutaneous steel rings for longitudinal surveillance of wound healing outcomes. In female swine, animals were maintained in the prone position and the genital confluence was sterilized by betadine application. The length of the urethra was measured using a 5 French ureteral stent and normal anatomy was confirmed prior to injury via cystoscopic evaluations described in following sections. A 23 French urethral resectoscope (AED, Model 8805B-SC, CA, United States) was then introduced into the

urethral meatus and electrocoagulation injury ~5 cm in length in the ventral anterior urethra was performed from the 3–9 o'clock position. The distal urethra located ~1 cm from the external meatus was kept intact to preserve external urinary sphincter function. Both female and male swine were recovered from anesthesia and maintained on a warming table. Intramuscular Banamine (1.1 mg/kg) was administered post-operatively and a transdermal fentanyl patch (1–4 μg/kg) was applied 24 h prior to the surgery for pain management. In addition, a 3.9 mg/day Oxytrol patch (Merck; Rahway, NJ, United States) was administered to all animals postoperatively to mitigate bladder spasms.

2.2.4 Retrograde Urethrography (RUG) and Urethroscopy

Urethroscopic and RUG evaluations were performed prior to surgical manipulations and weekly following electrocoagulation injury to visualize urethral anatomy and the degree of stricture severity. Male and female animals were sedated and anesthesia as well as post-operative analgesics were administered as described above. For male swine, animals were maintained in the supine position, the glans was exposed and a 9.5 rigid cystoscope was inserted through the urethral meatus. Video images were subsequently acquired by an imaging system (Image 1 HUB; Karl Storz, Tuttlingen, Germany) throughout the length of the organ. Following urethroscopy, a 6–8 French silicone catheter was inserted into the external urethral meatus and 1:1 diluted iohexol contrast agent (Omniopaque 300; GE Healthcare, Milwaukee, WI, United States) was instilled. Anterior-posterior retrograde urethrograms were acquired with C-arm fluoroscopy (BV Pulsera; Philips, Eindhoven, Netherlands). For female swine, animals set in the prone position and a speculum was placed into the genital confluence to access the urethral orifice.

Urethroscopic surveillance was performed in a similar fashion as described for males. Next, an open ended 14 French catheter was introduced ~1 cm into the external urethral orifice and the 1:1 diluted contrast agent was instilled, and serial anterior-posterior images were acquired as detailed above. Following confirmation of urethral stricture formation, animals were euthanized and urethral tissues were harvested for histological, immunohistochemical (IHC) and histomorphometric evaluations.

2.2.5 Histological, IHC, and Histomorphometric Analyses

Following necropsy, male and female urethras (N = 4 per gender) were resected en bloc and divided into proximal, central, and distal segments of equal length dispersed along the axis of the original electrocoagulation injury. Control specimens were isolated from uninjured urethral segments located distally from the site of initial damage. Specimens were then fixed in 10 % neutral-buffered formalin, dehydrated in graded alcohol solutions, and embedded in paraffin. Five micron sections were cut and samples were stained with Masson's trichrome (MTS) using routine histological methods. IHC analyses were performed on parallel sections following antigen retrieval in 10 mM sodium citrate buffer (pH 6.0) and incubation in blocking buffer containing phosphate-buffered saline with 5 % fetal bovine serum, 1 % bovine serum albumin, and 0.3 % Triton X-100 for 1 h at room temperature. Specimens were then stained for 12 h at 4 °C with the following primary antibodies: anti-α-smooth muscle actin (SMA) (1:200 dilution; Sigma-Aldrich, St. Louis, MO), anti-pan-cytokeratin (CK) (1:150 dilution; Dako, Carpinteria, CA), anti-myeloperoxidase (MPO, Abcam, Cambridge, MA, 1:100 dilution), anti-CD68 (Thermo Fisher Scientific, Cambridge, MA, 1:200 dilution), anti-neurofilament 200 (NF200) (Sigma-Aldrich,

1:250 dilution], and anti-CD31 (1:100 dilution; Abcam). For MPO and CD68 detection, specimens were incubated with species-matched, horseradish peroxidase (HRP)-conjugated secondary antibodies and 3,3'Diaminobenzidine (DAB) substrate and then counterstained with hematoxylin. For all other markers, samples were probed with species-matched Alexa Fluor 594-conjugated secondary antibodies (Thermo Fisher Scientific, Waltham, MA) and 4′, 6-diamidino-2-phenyllindole (DAPI) nuclear counterstain. Visualization of stained tissues was carried out with a Zeiss Axio Imager M2 model (Carl Zeiss MicroImaging, Thornwood, NY) and representative fields were acquired with Zen software (version 3.1). Negative controls consisting of parallel tissue specimens incubated with secondary antibodies in the absence of primary antibodies were carried out similarly and produced no significant signal above background.

Histomorphometric evaluations (N = 4 per gender and urethral segment) were performed on proximal, central, distal, and control urethral specimens described above using previously published methods.[33,34] Area measurements and image thresholding were carried out on global 5× microscopic fields encompassing the urethral cross-section acquired from 3 serial sectioned specimens per region with ImageJ software (version 1.47). Quantitation of urethral luminal area following electrocoagulation injury was calculated in each damaged segment relative to corresponding control area for each animal following MTS. For IHC analyses, the relative percentages of tissue area stained for markers of interest per total field area was performed in parallel using similar protocols. In addition, the number of NF200+ nerve trunks and CD31+ vessels were calculated across four independent microscopic fields (10×) per urethral sample using comparable methods and normalized to total field area to calculate maker densities.

2.2.6 Statistical Evaluations

Statistical evaluations of quantitative data between groups was performed using the Kruskal Wallis test in combination with the post hoc Dunn's test considering a value of $p < 0.05$ as significant. Quantitative data were reported as mean ± standard deviation (SD).

2.3 Results

In both sexes, normal urethral anatomy was confirmed in all animals (N = 4 male/female swine) prior to surgery by RUG and urethroscopic analyses (**Figure 1A, B, left columns**). Following vesicostomy creation, a focal, partial thickness urethral injury was performed via electrocoagulation over a 6 cm long segment of the male penile urethra. This surgical strategy was utilized since it avoids the tortuosity of the sigmoid flexure present in proximal male urethra thus permitting transurethral instrumentation with a standard urethroscope. Electrocoagulation of female swine urethra was performed in a similar fashion, however due to the shorter length of the female urethra relative to males, the injury region was 5 cm long. All animals survived primary urethral damage and were evaluated weekly for up to 6 weeks by RUG and urethroscopic analyses to determine the kinetics of stricture formation. There were no intraoperative complications noted during vesicostomy and electrocoagulation procedures and all animals were successfully recovered from anesthesia and survived to harvest. External urine flow from suprapubic catheters was apparent in all animals throughout the study period, however catheter reinsertion was necessary in 2 pigs (1F and 2 M) following dislodgement from the vesicostomy.

Figure 1: Imaging Evaluations of Iatrogenic Urethral Injury and Stricture Formation

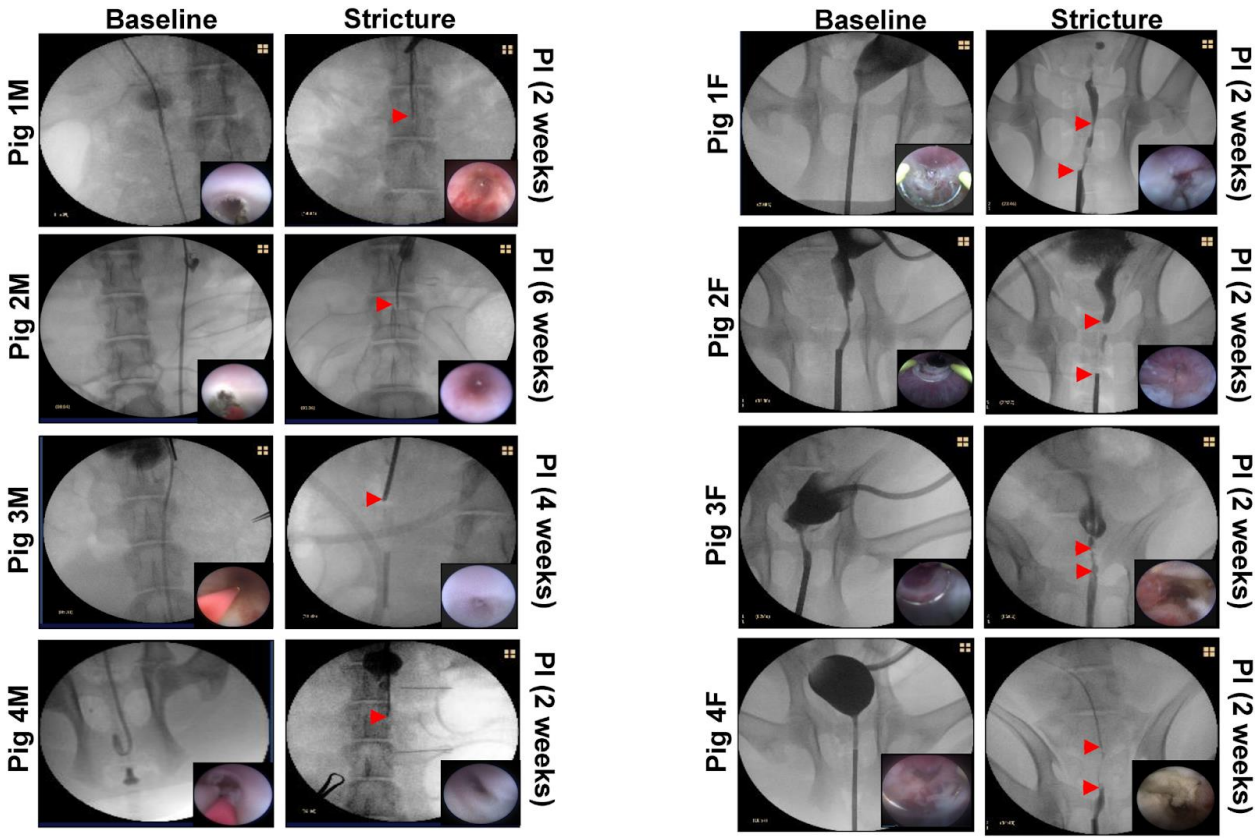

1. Representative RUG analyses in male **[A]** and female **[B]** swine at baseline prior to electrocoagulation (left columns) and at 2–6 weeks post-injury (PI) demonstrating urethral stricture formation (right columns). Arrowheads in both panels demarcate the proximal and distal borders of strictured regions. Insets display endoscopic assessments of injured segments following primary urethral damage (left columns) and at terminal timepoints (right columns). Source: Gundogdu, Gokhan et al. Surgery open science vol. 16 (2024): 205-214. Used with permission.

Post-operative outcomes in swine are summarized in **Table 1**. All female swine exhibited urinary straining 3–10 days following initial urethral injury which resulted in rectal prolapses <2 cm in length. Prolapses were managed with non-invasive methods including analgesics and constipation mitigation. Urethral stricture formation was detected by imaging modalities in all female swine by 2 weeks following urethral damage (**Figure 1B, right column**). In particular, strictures presented as limited extension of contrast agent and/or stenosis along the length of the original electrocoagulation injury following RUG analysis. In addition, Pigs 2F and 3F displayed dilated urethral segments proximal to

the injured regions due to putative hydrodistension. Moreover, urethroscopic observations revealed prominent red and edematous areas throughout the injured urethral mucosa in all female swine indicative of chronic inflammatory processes. The mean length of urethral strictures in female swine calculated from RUG photomicrographs was 4 ± 1.4 cm (N = 4) with a range from 2 to 5 cm. In males, stricture formation occurred in 100 % of animals (**Figure 1A, right column**). However, the onset of urethral stenosis was delayed relative to the female cohort and occurred between 2 and 6 weeks following injury with a mean duration of 3.2 ± 1.8 weeks. In addition, male swine tolerated urethral damage without any clinical presentations of urinary straining or rectal prolapse in contrast to females. Injured urethral mucosa in males also contained red and edematous tissues consistent with ongoing stages of wound healing. RUG and urethroscopic analyses at terminal timepoints revealed all male animals exhibited discrete regions of luminal ablation scattered along the original injury site which impeded extension of contrast agent into the bladder. This scenario precluded quantitation of urethral stricture length from in situ imaging observations since the proximal region of the original injury site could not be penetrated by contrast instillation.

Table 1: Post-operative Outcomes in Male and Female Swine Following Urethral Injury

Animals	Study Period	Complications and Management	Imaging Outcomes	Stricture Length
Pig 1F	2 Weeks	Dislodgement and reinsertion of vesicostomy catheter at post-op day 11. Rectal prolapse observed at post-op day 13 due to urinary straining.	Mild/Moderate stenosis and inflammed mucosa detected. Limited extension of contrast agent in injured segments.	5cm

Pig 2F	2 Weeks	Rectal prolapse observed at post-op day 12 due to urinary straining.	Mild/Moderate stenosis and inflammed mucosa detected. Limited extension of contrast agent in injured segments.	5cm
Pig 3F	2 Weeks	Rectal prolapse observed at post-op day 13 due to urinary straining.	Mild/Moderate stenosis and inflammed mucosa detected. Limited extension of contrast agent in injured segments.	2cm
Pig 4F	2 Weeks	Rectal prolapse observed at post-op day 3 due to urinary straining.	Mild/Moderate stenosis and inflammed mucosa detected. Limited extension of contrast agent in injured segments.	4cm
Pig 1M	2 Weeks	None	Complete urethral occlusion and inflammed mucosa observed.	4cm
Pig 2M	6 Weeks	Dislodgement and reinsertion of vesicostomy catheter at post-op day 18.	Complete urethral occlusion and inflammed mucosa observed.	4cm
Pig 3M	6 Weeks	None	Complete urethral occlusion and inflammed mucosa observed.	4cm
Pig 4M	2 Weeks	None	Complete urethral occlusion and inflammed mucosa observed.	4cm

Source: Gundogdu, Gokhan et al. Surgery open science vol. 16 (2024): 205-214. Used with permission.

Global histological (MTS) evaluations were performed on injured urethral segments as well as control regions to characterize the extent of tissue remodeling and degree of stricture severity (**Figure 2**). In contrast to control segments, spongiofibrosis was apparent throughout the proximal, central, and distal areas of injured male urethras with varying degrees of stenosis noted secondary to luminal invasion of collagenous tissues consistent

with imaging findings (**Figure 2A**). In addition, all male swine demonstrated significant reductions in relative luminal area within central regions of the original injury site relative to controls, whereas 2/5 animals displayed significant attenuation of either proximal (Pigs 1 M, 3 M) or distal (Pig 2 M, 4 M) luminal areas compared to uninjured segments (**Figure 2C, E**). Therefore, the mean length of urethral strictures in all males was ~4 cm based on the length of urethral segments exhibiting significant declines in luminal area relative to controls. In contrast to males, stricture severity was less pronounced in female swine with no significant differences in relative luminal areas noted in injured regions in respect to control segments except for dilation of the central region of Pig 4F (**Figure 2B, D**). These data suggest that obstructive uropathy encountered in porcine urethral strictures is primarily due to anatomical obstruction in males, while female pathology is a result of putative functional obstruction.

Figure 2: Histological Assessments of Long Urethral Stricture Formation in Male and Female Swine

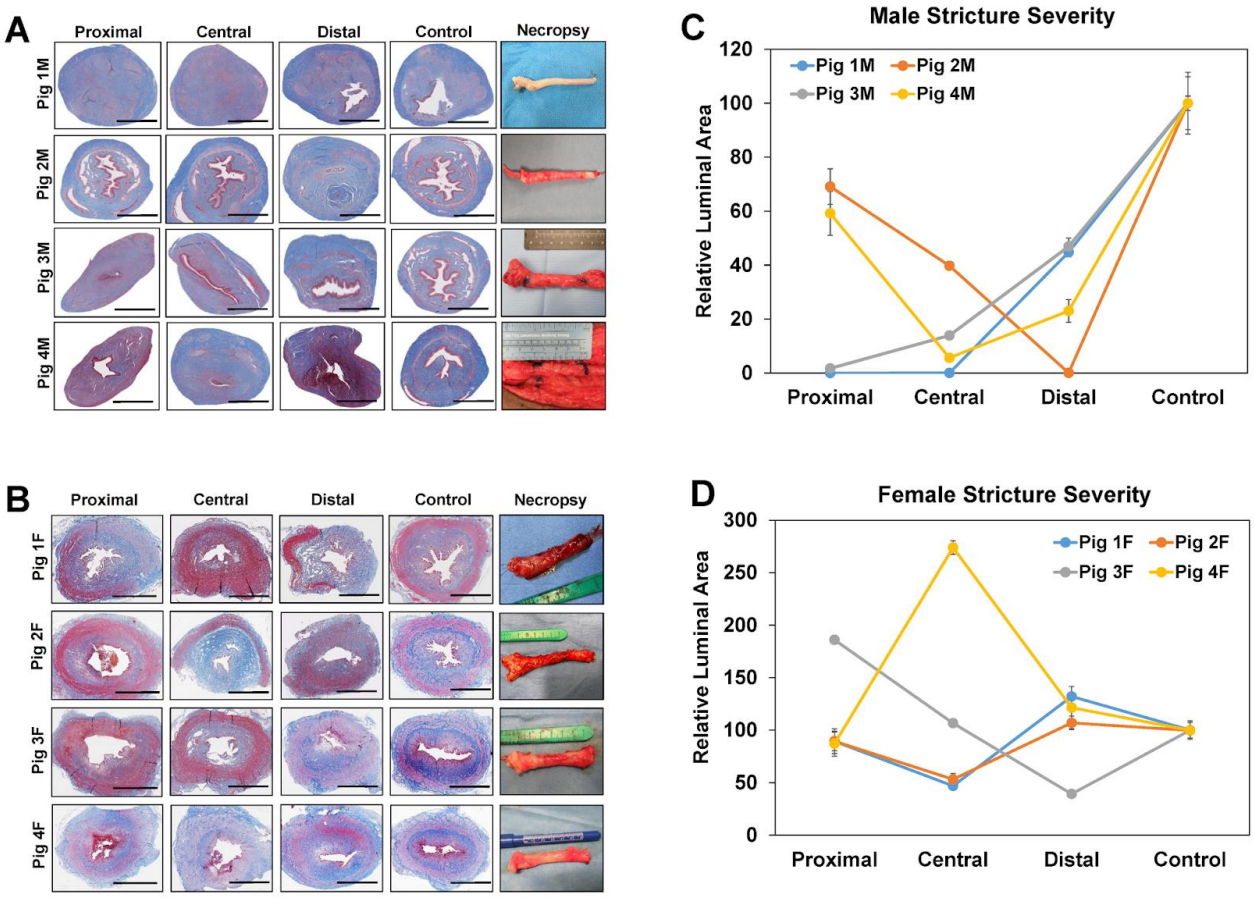

E

Relative Luminal Area			
Animals	Dunn's Tests, *p* values		
	Proximal vs Control	Central vs Control	Distal vs Control
Pig 1M	0.003	0.02	0.30
Pig 2M	0.31	0.04	0.002
Pig 3M	0.002	0.04	0.31
Pig 4M	0.31	0.002	0.04
Pig 1F	0.57	0.07	0.21
Pig 2F	0.82	0.09	0.21
Pig 3F	0.07	0.41	0.41
Pig 4F	0.43	0.03	0.26

[A, B] Gross necropsy specimens and cross-sectional views of MTS-stained, strictured segments (proximal, central, distal) and control regions from male and female urethras. Scale bars = 7 mm for histological panels. **[C, D]** Quantitation of relative luminal areas in control and injured groups described in panels A and B. Data are presented as means ± standard deviations. **[E]** Kruskal-Wallis and post hoc Dunn's tests were performed on data described in **C.** Table displays p values from Dunn's analysis with significant regional differences ($p < 0.05$) between strictured regions and respective controls for each animal noted in green highlighted fields. (For interpretation of the references to colour in this figure legend, the reader is referred to the web version of this article.) Source: Gundogdu, Gokhan et al. Surgery open science vol. 16 (2024): 205-214. Used with permission.

In both genders, focal regions of epithelial sloughing as well as submucosal fibrosis and infiltration of mononuclear inflammatory cells were observed throughout the walls of damaged urethral sections (**Figure 2A, B**). IHC assessments (**Figures. 3A, 4A**) revealed

CD68 + macrophages and MPO+ neutrophils were primarily distributed in the mucosa of injured regions in both male and female urethras. Histomorphometric outcomes of immunostained specimens (**Figures 3B, 4B**) demonstrated that 50 % of male and female replicates displayed significant reductions in Pan-CK+ epithelia as well as alterations in vascular density within discrete strictured regions in comparison to relative controls. In addition, proximal and central regions of urethral strictures in 50 % of the male cohort displayed significant declines in SMA + smooth muscle bundles from control levels, whereas no significant changes in smooth muscle content were observed in damaged female urethras. Assessments of nerve densities in experimental groups did not uncover significant alterations between injured and control segments in either sex. These data demonstrate that electrocoagulation injury results in long (~4 cm in length) urethral stricture formation in both male and female swine, however the extent of pathology severity is dependent on gender, injury location and individual wound healing response.

Figure. 3. Immunohistochemical and Histomorphometric Analyses of Long Urethral Strictures in Male Swine

A

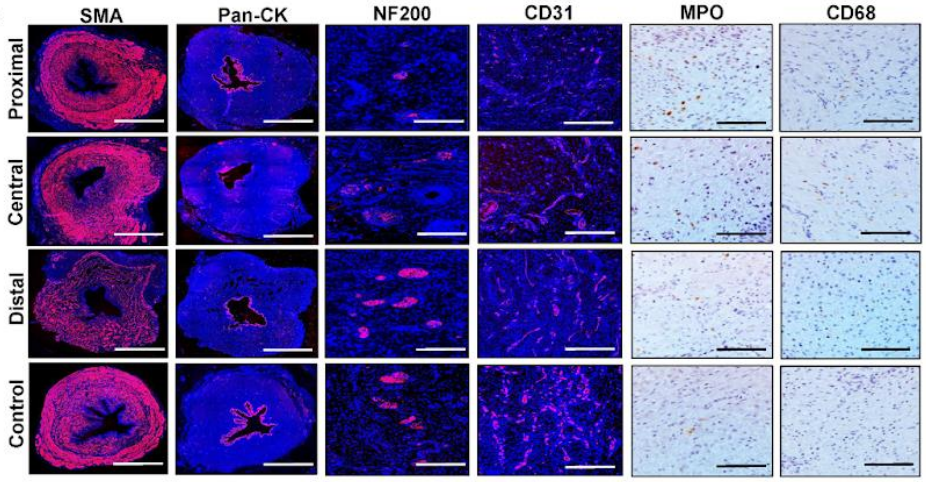

B

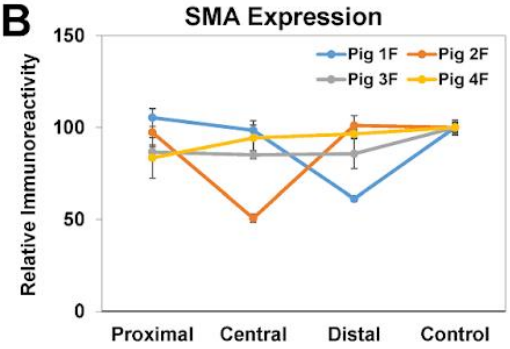

D

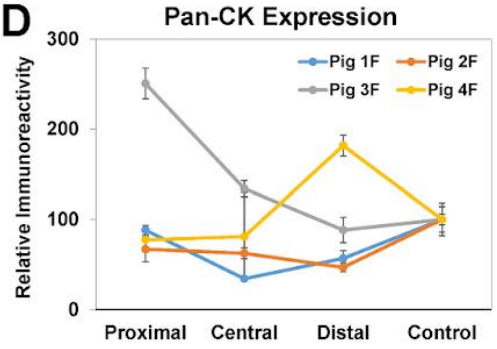

C

SMA Expression			
Animals	Kruskal-Wallis and Dunn's Tests, *p* values		
	Proximal vs Control	Central vs Control	Distal vs Control
Pig 1F	0.26	0.91	0.09
Pig 2F	0.09 (KW)	0.09 (KW)	0.087 (KW)
Pig 3F	0.08 (KW)	0.08 (KW)	0.08 (KW)
Pig 4F	0.20 (KW)	0.20 (KW)	0.20 (KW)

E

Pan-CK Expression			
Animals	Kruskal-Wallis and Dunn's Tests, *p* values		
	Proximal vs Control	Central vs Control	Distal vs Control
Pig 1F	0.57	0.02	0.15
Pig 2F	0.14	0.11	0.002
Pig 3F	0.02	0.21	0.57
Pig 4F	0.06 (KW)	0.06 (KW)	0.06 (KW)

F

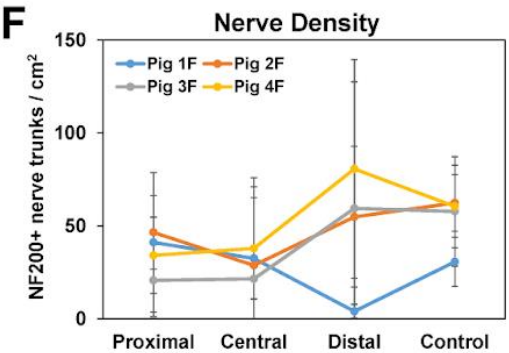

H

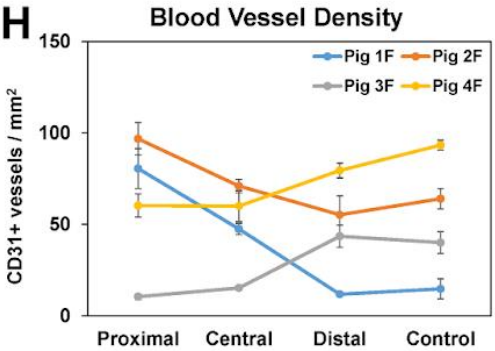

G

Nerve Density			
Animals	Kruskal-Wallis and Dunn's Tests, *p* values		
	Proximal vs Control	Central vs Control	Distal vs Control
Pig 1F	0.25 (KW)	0.25 (KW)	0.25 (KW)
Pig 2F	0.52 (KW)	0.52 (KW)	0.52 (KW)
Pig 3F	0.38 (KW)	0.38 (KW)	0.38 (KW)
Pig 4F	0.37 (KW)	0.37 (KW)	0.37 (KW)

I

Blood Vessel Density			
Animals	Kruskal-Wallis and Dunn's Tests, *p* values		
	Proximal vs Control	Central vs Control	Distal vs Control
Pig 1F	0.001	0.02	0.31
Pig 2F	0.31 (KW)	0.31 (KW)	0.31 (KW)
Pig 3F	0.02	0.10	0.91
Pig 4F	0.11 (KW)	0.11 (KW)	0.11 (KW)

[A] Representative photomicrographs of selective protein expression in strictured segments (proximal, central, distal) and control regions from Pig 4 M. Markers include smooth muscle contractile protein (SMA), epithelial protein (pan-CK), vascular endothelial CD31 protein, neuronal NF200 protein and neutrophil (MPO) and macrophage (CD68) antigens. For columns 1–4, respective marker expression is labeled in red (Alexa Fluor 594 labeling) with blue representing DAPI nuclear counterstain. For columns 5–6, positive marker labeling is in brown (horseradish peroxidase) with hematoxylin nuclear counterstain in blue. Scale bars for 1st and 2nd columns are 7 mm, 3rd and 4th columns are 600 μm, and 5th and 6th columns are 200 μm. SMA, smooth muscle actin; Pan-CK, pan-cytokeratin; NF200, neurofilament 200; MPO, myeloperoxidase; DAPI, 4′, 6-diamidino-2-phenyllindole. **[B, D, F, G]** Quantitative assessments of markers displayed in panel A for Pigs 1 M–4 M. Data are presented as means ± standard deviations. **[C, E, G, I]** Kruskal-Wallis (KW) and post hoc Dunn's tests were performed on data described in panels **B, D, F** and **G**. Tables display p values from KW or Dunn's analyses with significant regional differences ($p < 0.05$) between strictured regions and respective controls for each animal noted in green highlighted fields. (For interpretation of the references to colour in this figure legend, the reader is referred to the web version of this article.) Source: Gundogdu, Gokhan et al. Surgery open science vol. 16 (2024): 205-214. Used with permission.

Figure 4: Immunohistochemical and Histomorphometric Assessments of Long Urethral Strictures in Female Swine

A

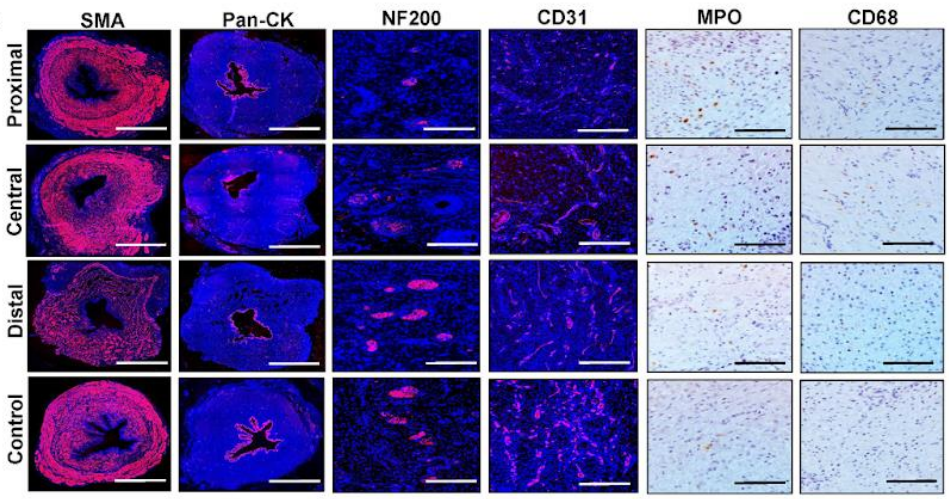

B

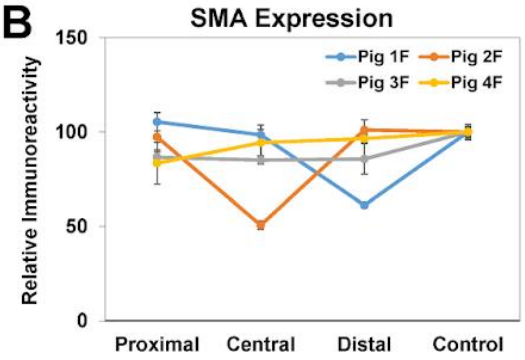

D

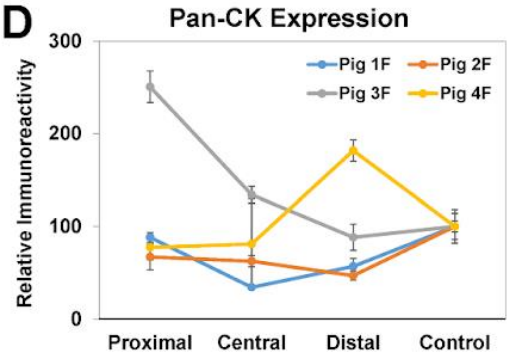

C

SMA Expression			
Animals	Kruskal-Wallis and Dunn's Tests, *p* values		
	Proximal vs Control	Central vs Control	Distal vs Control
Pig 1F	0.26	0.91	0.09
Pig 2F	0.09 (KW)	0.09 (KW)	0.087 (KW)
Pig 3F	0.08 (KW)	0.08 (KW)	0.08 (KW)
Pig 4F	0.20 (KW)	0.20 (KW)	0.20 (KW)

E

Pan-CK Expression			
Animals	Kruskal-Wallis and Dunn's Tests, *p* values		
	Proximal vs Control	Central vs Control	Distal vs Control
Pig 1F	0.57	0.02	0.15
Pig 2F	0.14	0.11	0.002
Pig 3F	0.02	0.21	0.57
Pig 4F	0.06 (KW)	0.06 (KW)	0.06 (KW)

F

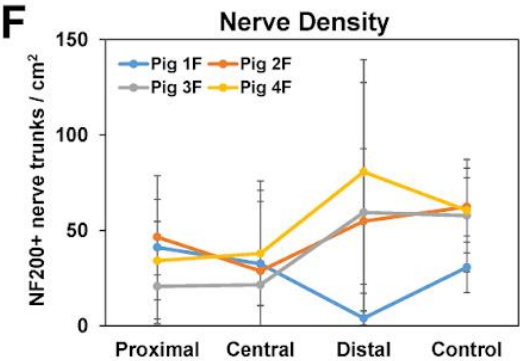

H

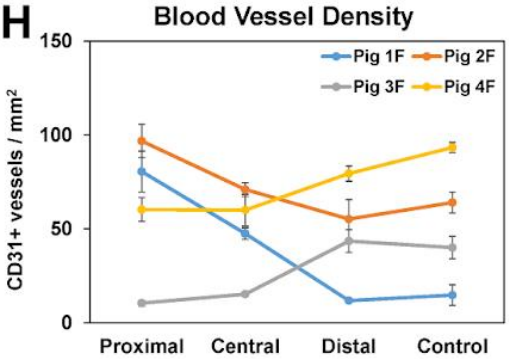

G

Nerve Density			
Animals	Kruskal-Wallis and Dunn's Tests, *p* values		
	Proximal vs Control	Central vs Control	Distal vs Control
Pig 1F	0.25 (KW)	0.25 (KW)	0.25 (KW)
Pig 2F	0.52 (KW)	0.52 (KW)	0.52 (KW)
Pig 3F	0.38 (KW)	0.38 (KW)	0.38 (KW)
Pig 4F	0.37 (KW)	0.37 (KW)	0.37 (KW)

I

Blood Vessel Density			
Animals	Kruskal-Wallis and Dunn's Tests, *p* values		
	Proximal vs Control	Central vs Control	Distal vs Control
Pig 1F	0.001	0.02	0.31
Pig 2F	0.31 (KW)	0.31 (KW)	0.31 (KW)
Pig 3F	0.02	0.10	0.91
Pig 4F	0.11 (KW)	0.11 (KW)	0.11 (KW)

[A] Representative photomicrographs of selective protein expression in strictured segments (proximal, central, distal) and control regions from Pig 1F. Markers include smooth muscle contractile protein (SMA), epithelial protein (pan-CK), vascular endothelial CD31 protein, neuronal NF200 protein and neutrophil (MPO) and macrophage (CD68) antigens. For columns 1–4, respective marker expression is labeled in red (Alexa Fluor 594 labeling) with blue representing DAPI nuclear counterstain. For columns 5–6, positive marker labeling is in brown (horseradish peroxidase) with hematoxylin nuclear counterstain in blue. Scale bars for 1st and 2nd columns are 7 mm, 3rd and 4th columns are 600 μm, and 5th and 6th columns are 200 μm. SMA, smooth muscle actin; Pan-CK, pan-cytokeratin; NF200, neurofilament 200; MPO, myeloperoxidase; DAPI, 4′, 6-diamidino-2-phenyllindole. **[B, D, F, G]** Quantitative assessments of markers displayed in panel A for Pigs 1Fsingle bond4F. Data are presented as means ± standard deviations. **[C, E, G, I]** Kruskal-Wallis (KW) and post hoc Dunn's tests were performed on data described in panels **B, D, F and G**. Tables display p values from KW or Dunn's analyses with significant regional differences ($p < 0.05$) between strictured regions and respective controls for each animal noted in green highlighted fields. (For interpretation of the references to colour in this figure legend, the reader is referred to the web version of this article.)
Source: Gundogdu, Gokhan et al. Surgery open science vol. 16 (2024): 205-214. Used with permission.

2.4 Discussion

The aims of this study were to establish male and female porcine models of iatrogenic long (≥4 cm) urethral strictures and determine the impact of gender on wound healing responses to urethral injury. Urinary diversion via vesicostomy was performed in all animals to mitigate deleterious elevation of urinary storage pressures secondary to stricture formation. Longitudinal imaging was conducted to monitor the rate and severity of stricture formation, while histological, IHC and histomorphometric evaluations were carried out to profile gender-specific wound healing patterns. We utilized focal electrocoagulation to induce urethral damage in swine based on past findings in porcine and rabbit models demonstrating this mode of injury was sufficient to generate short urethral strictures (1–2 cm in length) with histopathological features similar to human disease.[35] The length of primary urethral injury was 5 cm in females and 6 cm in males which represented ~63 % and ~ 38 % of the total urethral length, respectively based on mean lengths reported for each gender (8 cm in females versus 16 cm in males).[36,37] Clinical presentations of urethral injury following electrocoagulation were substantially different between male and female cohorts with the latter experiencing severe straining and rectal prolapses. The discrepancy in post-operative outcomes between sexes may be

related to the greater proportion of the urethra subjected to injury in females which could have exacerbated urethritis and pain resulting in increased straining during voiding attempts. In addition, putative damage to the pudendal nerve in females during model creation may have also contributed to the higher incidence of rectal prolapse secondary to pelvic floor dysfunction.[38]

The mean onset of stricture formation in both sexes (2–3 weeks post-op) was comparable to previous studies in male rabbits and swine which demonstrated the development of short strictures 1–2 weeks post-electrocoagulation injury.[35,39] Despite variations in the size of the original injury site, both genders exhibited urethral strictures with a mean length of ~4 cm presumably due to axial wound contracture. Similar to human pathology, mucosal damage was evident throughout stricture segments in both cohorts characterized by focal loss of Pan-CK+ epithelia, perturbations in vascular density as well as invasion of CD68 + macrophages and MPO+ neutrophils.[35] However, our results also showed marked variations in the degree of stricture severity between male and female groups. Specifically, male urethras contained stenotic regions with significantly reduced luminal areas compared to controls, while female counterparts showed modest declines in organ caliber and primarily exhibited functional obstruction. Male urethras were also more susceptible to smooth muscle loss following injury than females and displayed qualitatively higher levels of spongiofibrosis in damaged segments. In addition, the smaller caliber of the urethra in males (9.5 French) relative to females (23 French) likely predisposed the former to anatomical obstruction due to aberrant collagen deposition and radial wound contraction in the urethral wall. On the other hand, the presence of filling defects in female strictures may be explained by declines in urethral wall elasticity from poor mucosal

healing which could have restricted fluid flow.[40,41] Indeed, functional urethral obstruction has also been observed in hypospadias patients following tubularized incised plate procedure wherein the reconstructed urethral wall exhibits impaired epithelialization and a contracted groove develops which impedes urine transport, but allows for free passage of a rigid catheter.[41]

There were a number of limitations in our present study. First, we utilized castrated male swine in our protocols to mitigate aggressive behavior during animal husbandry operations.[42] However, Hofer and colleagues previously showed that testosterone supplementation in castrated rats following urethrotomy led to increased inflammatory responses and myofibroblast proliferation; conditions which may predispose urethras to stricture formation.[43] Therefore, the impact of androgen signaling should be considered in male models of urethral stricture disease to account for the effects of testosterone on urethral healing. Secondly, the use of RUG evaluations alone to quantify stricture length in males was insufficient due to distal luminal obstructions which impeded visualization of the proximal stricture border. Future evaluations of long urethral strictures in swine will also deploy antegrade urethrograms and voiding cystourethrograms to more precisely define stricture dimensions in proximal urethral segments as previously described.[44] Finally, the sample sizes deployed in our investigation were small and primarily focused on histological and imaging assessments from one terminal timepoint. Follow-up mechanistic studies on larger scale cohorts which include early and late stage assessments of stricture formation may shed light on signaling processes that govern pathology development in both genders.

2.5 References

1) Caneparo C, Chabaud S and Bolduc S. Challenges and Perspectives in Male Anterior Urethra Reconstruction Using Tissue Engineering. Urology: Research And Therapeutics Journal. 2019; 2(1):127.

2) Anger, Jennifer T et al. “The morbidity of urethral stricture disease among male medicare beneficiaries.” BMC urology vol. 10 3. 18 Feb. 2010, doi:10.1186/1471-2490-10-3

3) Santucci, Richard A et al. “Male urethral stricture disease.” The Journal of urology vol. 177,5 (2007): 1667-74. doi:10.1016/j.juro.2007.01.041

4) Lubahn, Jessica D et al. “Poor quality of life in patients with urethral stricture treated with intermittent self-dilation.” The Journal of urology vol. 191,1 (2014): 143-7. doi:10.1016/j.juro.2013.06.054

5) Erickson, Bradley A et al. “Prospective analysis of ejaculatory function after anterior urethral reconstruction.” The Journal of urology vol. 184,1 (2010): 238-42. doi:10.1016/j.juro.2010.03.038

6) Weese, Jonathan R et al. “Anterior Urethral Stricture Disease Negatively Impacts the Quality of Life of Family Members.” Advances in urology vol. 2016 (2016): 3582862. doi:10.1155/2016/3582862

7) Gallegos, Maxx A, and Richard A Santucci. “Advances in urethral stricture management.” F1000Research vol. 5 2913. 23 Dec. 2016, doi:10.12688/f1000research.9741.1

8) Hampson, Lindsay A et al. “Male urethral strictures and their management.” Nature reviews. Urology vol. 11,1 (2014): 43-50. doi:10.1038/nrurol.2013.275

9) Kinnaird, Adam S et al. “Stricture length and etiology as preoperative independent predictors of recurrence after urethroplasty: A multivariate analysis of 604 urethroplasties.” Canadian Urological Association journal = Journal de l'Association des urologues du Canada vol. 8,5-6 (2014): E296-300. doi:10.5489/cuaj.1661

10) Mundy, Anthony R, and Daniela E Andrich. “Urethral strictures.” BJU international vol. 107,1 (2011): 6-26. doi:10.1111/j.1464-410X.2010.09800.x

11) Carr, L K, and G D Webster. “Bladder outlet obstruction in women.” The Urologic clinics of North America vol. 23,3 (1996): 385-91. doi:10.1016/s0094-0143(05)70319-0

12) Groutz, A et al. “Bladder outlet obstruction in women: definition and characteristics.” Neurourology and urodynamics vol. 19,3 (2000): 213-20. doi:10.1002/(sici)1520-6777(2000)19:3<213::aid-nau2>3.0.co;2-u

13) Kuo, Hann-Chorng. “Videourodynamic characteristics and lower urinary tract symptoms of female bladder outlet obstruction.” Urology vol. 66,5 (2005): 1005-9. doi:10.1016/j.urology.2005.05.047

14) Osman, Nadir I, and Christopher R Chapple. “Contemporary surgical management of female urethral stricture disease.” Current opinion in urology vol. 25,4 (2015): 341-5. doi:10.1097/MOU.0000000000000186

15) Faiena, Izak et al. “Female Urethral Reconstruction.” The Journal of urology vol. 195,3 (2016): 557-67. doi:10.1016/j.juro.2015.07.124

16) Osman, Nadir I et al. “A systematic review of surgical techniques used in the treatment of female urethral stricture.” European urology vol. 64,6 (2013): 965-73. doi:10.1016/j.eururo.2013.07.038

17) Keegan, Kirk A et al. “Female urethral stricture disease.” Current urology reports vol. 9,5 (2008): 419-23. doi:10.1007/s11934-008-0071-7

18) Agochukwu-Mmonu, Nnenaya et al. “Female Urethral Strictures: Review of Diagnosis, Etiology, and Management.” Current urology reports vol. 20,11 74. 8 Nov. 2019, doi:10.1007/s11934-019-0933-1

19) Algarrahi, Khalid et al. “Repair of injured urethras with silk fibroin scaffolds in a rabbit model of onlay urethroplasty.” The Journal of surgical research vol. 229 (2018): 192-199. doi:10.1016/j.jss.2018.04.006

20) Akbal, Cem et al. “Bladder augmentation with acellular dermal biomatrix in a diseased animal model.” The Journal of urology vol. 176,4 Pt 2 (2006): 1706-11. doi:10.1016/j.juro.2006.04.085

21) Villoldo, Gustavo Martín et al. “Histologic changes after urethroplasty using small intestinal submucosa unseeded with cells in rabbits with injured urethra.” Urology vol. 81,6 (2013): 1380.e1-5. doi:10.1016/j.urology.2013.02.023

22) Versteegden, Luuk R M et al. “Tissue Engineering of the Urethra: A Systematic Review and Meta-analysis of Preclinical and Clinical Studies.” European urology vol. 72,4 (2017): 594-606. doi:10.1016/j.eururo.2017.03.026

23) Simsek, Abdulmuttalip et al. “Overcoming scarring in the urethra: Challenges for tissue engineering.” Asian journal of urology vol. 5,2 (2018): 69-77. doi:10.1016/j.ajur.2018.02.002

24) Andersen, H L et al. “An experimental model for stricture studies in the anterior urethra of the male rabbit.” Urological research vol. 31,6 (2003): 363-7. doi:10.1007/s00240-003-0333-2

25) Faydaci, Gökhan et al. “Comparison of two experimental models for urethral stricture in the anterior urethra of the male rabbit.” Urology vol. 80,1 (2012): 225.e7-11. doi:10.1016/j.urology.2012.04.025

26) Meria, P et al. “An experimental model of bulbar urethral stricture in rabbits using endoscopic radiofrequency coagulation.” Urology vol. 53,5 (1999): 1054-7. doi:10.1016/s0090-4295(98)00642-6

27) Chen Q, Cheng W, Cao J, Li JP, Dai SJ, Deng WL, Shen Y: An experimental model for stricture studies in the anterior urethra of the male canine. J Mod Urol 2008;13:303-305.

28) Zhang, B. H., et al. "Establishment of a model of bulbar urethral stricture in male rabbits by bombing." Chin J Traumatol 3 (2007): 225-8.

29) Hu, Wei-Feng et al. “An experimental model of urethral stricture in rabbits using holmium laser under urethroscopic direct visualization.” Urologia internationalis vol. 93,1 (2014): 108-12. doi:10.1159/000355353

30) Chung, Yeun Goo et al. “Acellular bi-layer silk fibroin scaffolds support tissue regeneration in a rabbit model of onlay urethroplasty.” PloS one vol. 9,3 e91592. 14 Mar. 2014, doi:10.1371/journal.pone.0091592

31) Algarrahi, Khalid et al. “Repair of injured urethras with silk fibroin scaffolds in a rabbit model of onlay urethroplasty.” The Journal of surgical research vol. 229 (2018): 192-199. doi:10.1016/j.jss.2018.04.006

32) Tasker, Louisa et al. “Exploring the Gaps in Practical Ethical Guidance for Animal Welfare Considerations of Field Interventions and Innovations Targeting Dogs and Cats.” Animals : an open access journal from MDPI vol. 8,2 19. 27 Jan. 2018, doi:10.3390/ani8020019

33. Algarrahi K., Affas S., Sack B.S., Yang X., Costa K., Seager C., et al. Repair of injured urethras with silk fibroin scaffolds in a rabbit model of onlay urethroplasty. J Surg Res. 2018;229:192–199.

34. Chung Y.G., Tu D., Franck D., Gil E.S., Algarrahi K., Adam R.M., et al. Acellular bi-layer silk fibroin scaffolds support tissue regeneration in a rabbit model of onlay urethroplasty. PloS One. 2014;9

35. Sievert K.D., Selent-Stier C., Wiedemann J., et al. Introducing a large animal model to create urethral stricture similar to human stricture disease: a comparative experimental microscopic study. J Urol. 2012;187:1101–1109.

36. Dass N., McMurray G., Greenland J.E., Brading A.F. Morphological aspects of the female pig bladder neck and urethra: quantitative analysis using computer assisted 3-dimensional reconstructions. *J Urol.* 2001;165:1294–1299.

37. Ragionieri L., Ravanetti F., Gazza F., Botti M., Ivanovska A., Cacchioli A. Morphological analysis of the urethral muscle of the male pig with relevance to urinary continence and micturition. *J Anat.* 2016;228:511–519.

38. Toglia M.R. Pathophysiology of anorectal dysfunction. *Obstet Gynecol Clin North Am.* 1998;25:771–781.

39. Andersen H.L., Duch B.U., Nielsen J.B., Joergensen B., Ledet T. An experimental model for stricture studies in the anterior urethra of the male rabbit. *Urol Res.* 2003;31:363–367.

40. Singh M., Blandy J.P. The pathology of urethral stricture. *J Urol.* 1976;115:673–676.

41. Hadidi, A.T. Functional Urethral Obstruction (FUO). Hypospadias Surgery 2nd ed. (NY): Springers Publishing; 2022.

42. Sutherland M.A., Davis B.L., Brooks T.A., McGlone J.J. Physiology and behavior of pigs before and after castration: effects of two topical anesthetics. Animal. 2010;4:2071–2079.

43. Hofer M.D., Cheng E.Y., Bury M.I., Xu W., Hong S.J., Kaplan W.E., et al. Androgen supplementation in rats increases the inflammatory response and prolongs urethral healing. Urology. 2015;85:691–697.

44. Goel A., Gupta A., Dalela D. Antegrade urethrogram: a technique to visualize the proximal bulbous urethral segment in anterior urethral stricture. Indian J Urol. 2009;25:415–416.

Chapter 3: Silk Fibroin Conduits for Urinary Diversion in Swine

3.1 Objective

We will evaluate the efficacy of acellular, tubular BLSF grafts to function as urinary conduits in a porcine model of urinary diversion.

3.2 Methods

3.2.1 Biomaterials

BLSF scaffolds were constructed from aqueous silk fibroin solutions derived from Bombyx mori silkworm cocoons using a solvent-casting/salt-leaching procedure in combination with silk fibroin (SF) film casting as previously described.[24] The mechanical and structural properties of the matrix have been reported in published studies.[24] Biomaterials were sterilized with an autoclave before surgical procedures. Prior to implantation, BLSF grafts were tubularized under aseptic conditions using interrupted, nonabsorbable 5-0 sutures to create a urinary conduit (inner diameter, ~1 cm; length 3-4 cm) (**Figure 1A, insert**).

Figure 1: Porcine Unilateral Urinary Diversion Model

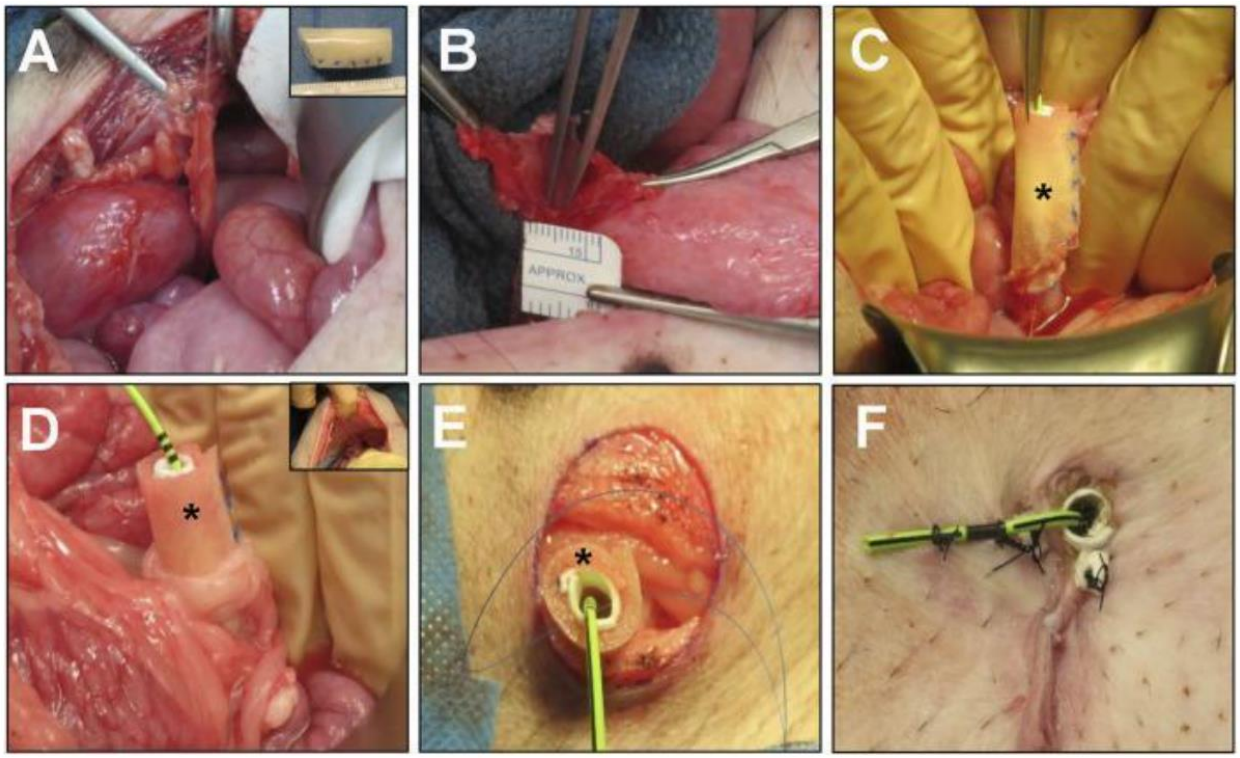

[A] Isolation of the right ureter with vascular supply preservation. **Inset:** BLSF tubular conduit. **[B]** Spatulation of the right ureter for construct implantation. **[C]** Oblique end-to-end anastomosis of BLSF conduit to the right ureter. **[D]** An omental flap was wrapped around the anastomosis and proximal half of the conduit to support de novo vascularization. **Inset:** Insertion of conduit through abdominal wall with omental wrap covering. The ureter-conduit anastomosis line was 3–5 mm away from the conduit insertion site at the abdominal wall. **[E]** Stomal creation and BLSF conduit placement at skin level. **[F]** Distal end of the BLSF construct with conduit and ureteral stent deployed and anchored to skin. (*) = BLSF tubular conduit in situ. BLSF, bi-layer silk fibroin scaffold. Source: Gundogdu, Gokhan et al. Frontiers in bioengineering and biotechnology vol. 11 (2023). Used with permission.

3.2.2 Surgical Procedures

Surgical, imaging and animal husbandry protocols were evaluated and approved by the University of California, Irvine Animal Care and Use Committee in accordance with protocol AUP-20–167. All animal procedures were carried out in compliance with the National Institutes of Health's Guidelines for the Care and Use of Laboratory Animals and ARRIVE guidelines (https://arriveguidelines.org). Urinary diversion with BLSF conduits was performed in five adult female, Yucatan mini-swine (30–40 kg, ~24 weeks of age, Premier BioSource, Ramona, CA) utilizing a uretero-cutaneous approach to create an incontinent urostomy (**Figure 1**). Male swine were omitted from the study to avoid

incisional complications with penile anatomy during abdominal exploration and conduit formation.

Prior to surgery, animals were fasted overnight with unabated access to water. General anesthesia was induced and maintained in swine as previously described.[25] Animals were then fixed in the supine position and renal sonography was performed as described below. The surgical area was scrubbed with povidone iodine and 70% ethanol three times and draped sterilely. The right ureter was accessed through a midline vertical lower abdominal incision followed by exposure of the retroperitoneum. The distal end of the right ureter was then ligated and dissected from the bladder with preservation of the vascular supply (**Figure 1A**) while the left ureter was left intact. The right ureter was spatulated to accommodate the circumference of the BLSF conduit (**Figure 1B**). Next, a 4.7 French, 24 cm double pigtail ureteral stent (Inlay Optima; BARD Inc., Covington, GA, United States) was introduced into the right ureter and the uretero-conduit anastomosis was completed using interrupted, 5–0 monofilament poliglecaprone sutures. The proximal end of the BLSF conduit was anastomosed to the spatulated ureter using an end-to-end approach in Pig 1 while an oblique end-to-end anastomosis was utilized in Pigs two to five to mitigate angulation between the conduit and the ureter (**Figure 1C**). In all animals, the anastomotic line was marked by 4 non-absorbable nylon sutures and two small radiopaque rings to identify the original conduit implantation area. An omental flap was wrapped around the anastomosis to support de novo vascularization and prevent potential anastomotic leakage (**Figure 1D**). Anterior-posterior, abdominal X-rays were acquired to confirm proper ureteral stent position as described below.

A conduit stoma was created at the lateral (Pig 1) or lower abdominal wall (Pigs 2–5) adjacent to the right hind leg. Briefly, a circular incision ~15 mm in diameter was made at the skin level and abdominal wall layers were dissected to create the conduit track. The BLSF conduit was delivered through the abdominal wall defect and then sutured to surrounding tissues to prevent parastomal herniation (**Figure 1E**). The distal end of the conduit was adjusted to protrude beyond the skin level by 2–3 mm and was then sutured to the skin with 4–0 interrupted, monofilament poliglecaprone sutures (**Figure 1F**). The distal end of the double pig-tail stent was subsequently trimmed and anchored to the skin with nylon sutures to mitigate stent dislodgement. Abdominal wall layers and skin were closed separately with absorbable sutures. In Pigs two to five, a short silicone stent (inner diameter, 6 mm; length 2.5 cm) was placed down to the distal end of the BLSF conduit to prevent acute stomal stenosis. This stent was fixed to the stoma edges with two additional nylon sutures. Both ureteral and conduit stents were replaced in all swine at 1 and 2 months post-operatively or at intermediate timepoints if stent dislodgement occurred, using standard procedures.[25] Briefly, an 8.5 French, 90 cm single J stent (Gyrus Medical Ltd., Wokingham, United Kingdom) was deployed into the renal pelvis using guidewire assistance and conduit stents were replaced as previously described. In addition, an 18 French, 15 mm segment of a urinary catheter (Covidien, Dublin, Ireland) was also positioned into the distal conduit and fixed to both conduit and ureteral stents to mitigate stoma stenosis.

Post-operative pain control and antibiotic regimens were executed in swine following the protocols previously described by Gundogdu and others.[25] Pig 1 was maintained with a ureteral stent alone for the duration of the study and developed stomal

stenosis as described below. Therefore, Pigs two to five were supported with both a silicone stomal stent and ureteral stent for the entire study period.

Longitudinal imaging analyses were performed prior to graft implantation and at 1, 2, and 3 months post- op to monitor urinary conduit and ureteral continuity, kidney morphology, and indwelling catheter position. These assessments included ultrasonography (USG), retrograde ureteropyelogram (RUPG) and video-endoscopy (cystoscopy, ureterorenoscopy) as described in the following sections. All swine were maintained for a total of 3 months and then sacrificed with an intravenous 0.2 ml/kg pentobarbital sodium and phenytoin sodium euthanasia solution (Euthasol; Virbac AH, Westlake, TX, United States). Following necropsy, the urinary conduit as well as right (operated) and left (unoperated) ureters were harvested from the urinary tract. The urinary conduit was divided axially into 4 circumferential rings (~0.6 cm in length) including the proximal anastomosis (adjacent to the host ureter), stomal region, and two central zones of neotissues (proximal and distal conduit). Conduit and ureteral specimens were evaluated with histological, immunohistochemical (IHC), and histomorphometric analyses.

3.2.3 Imaging Studies

USG was executed on all animals at selected timepoints and hydronephrosis was scored using previously reported methods.[25,26] Ureteral stent deployment and luminal conduit assessments were performed with a flexible uretero-renoscope (URS) (Flex-X2S; Karl Storz, Tuttlingen, Germany). Neotissue anastomotic borders were located with radiopaque markers placed following scaffold implantation. Images were captured with a

video processor system (Image 1 HUB; Karl Storz, Tuttlingen, Germany). Contrast imaging of the conduit and urinary tract was performed by infusing 1:1 diluted iohexol contrast agent (Omniopaque 300; GE Healthcare, Milwaukee, WI, United States) through the conduit stoma orifice. The conduit and anastomosis line were evaluated with anterior-posterior, lateral and oblique images following stent removal and acquired with standard fluoroscopy methods from our published reports.[27]

3.2.4 Histological, IHC, and histomorphometric analyses

Conduit (proximal anastomosis, stoma, proximal conduit, distal conduit, N = 5 animals per region) and ureteral (non-operated left and operated right ureters, N = 5 animals per region) specimens were fixed in 10% neutral-buffered formalin, dehydrated in alcohol solutions, and paraffin embedded. Five micron sections were cut and stained with Masson's trichrome (MTS) utilizing routine histological protocols. Parallel specimens were subjected to IHC evaluations following antigen retrieval in sodium citrate buffer (10 mM, pH 6.0) and incubation in blocking buffer containing phosphate-buffered saline, 5% fetal bovine serum, 1% bovine serum albumin, and 0.3% Triton X-100 for 1 h at ~25°C. Samples were independently incubated for 12 h at 4°C with the following primary antibodies: anti-α-smooth muscle actin (SMA) (1:200 dilution; Sigma-Aldrich, St. Louis, MO), anti-SM22α (1:200 dilution, Abcam, Cambridge, MA), anti-pan-cytokeratin (CK) (1:150 dilution; Dako, Carpinteria, CA), anti-uroplakin (UP) 3A (1:10 dilution, Fitzgerald, North Acton, MA), and anti-CD31 (1:100 dilution; Abcam). Following primary antibody incubation, samples were then probed with species-matched Alexa Fluor 647-conjugated secondary antibodies (Thermo Fisher Scientific, Waltham, MA). Nuclear counterstain was subsequently

performed with 4′, 6-diamidino-2-phenyllindole (DAPI). Sample visualization was carried out with a Zeiss Axio Imager M2 model (Carl Zeiss MicroImaging, Thornwood, NY) and representative fields of interest were captured with Zen software (version 3.1). Negative controls were stained in parallel with secondary antibodies alone and generated no detectable signal above background levels.

Histomorphometric analyses (N = 5 animals per region) were performed on global 5X microscopic fields encompassing the entire circumference of the tissue specimen using published protocols.[27] Imaging thresholding and area measurements were carried out with ImageJ software (version 1.47) to calculate the percentage of tissue area stained for pan-CK, α-SMA, and SM22α per total field area acquired. Quantitation of CD31+vessels was determined across four independent microscopic fields (20X) per specimen equally dispersed along the neotissue circumference using similar procedures and normalized to total field area to yield vascular density. Quantitation of CD31+vessel diameters in control and experimental replicates (170 ± 50 vessels per group) was performed in parallel using similar methodology.

3.2.5 Statistical Analysis

Quantitative data were analyzed with the Kruskal–Wallis test in combination with the post hoc Dunn's test for pairwise evaluations with $p < 0.05$ defined as significant. Quantitative data were presented as mean ± standard deviation (SD).

3.3 Results

Unilateral incontinent urinary diversion with BLSF conduits was carried out in five swine in combination with ureteral (Pigs 1–5) and conduit (Pigs 2–5) stenting (**Table 1**). Stenting procedures were employed to reinforce the mechanical integrity of remodeling neotissues and alleviate potential ureteral and stomal stenosis. A unilateral approach for urinary diversion was chosen to minimize the rate of animal mortality from potential conduit failure and renal damage. Fluoroscopic, URS and USG assessments were performed throughout the study period to monitor kidney function and urinary tract continuity. (**Figure 2**). There were no intraoperative or immediate postoperative complications encountered during BLSF conduit implantation and all animals were successfully recovered from anesthesia and survived to scheduled euthanasia at 3 months post-operative. External urine flow from the urinary conduit was evident in all animals across all study timepoints.

Table 1: Surgical Outcomes of Urinary Diversion with BLSF Conduits. Representative data from Pigs 1–5

Animal	Urinary Diversion Approach and Stent Strategy	Ultrasonography (Hydronephrosis Grade)				Complications and Management	Terminal Outcomes
		Pre-OP	1 month	2 months	3 months		
Pig 1	Incontinent urinary diversion with lateral urostomy and ureteral stenting for 3 months	0	2	2	2	Stent dislodgement and reinsertion: (post-op days 15 and 35). Diverticula at ureteral anastomosis observed at 1 month post-op.	Patent tubular neotissue with no conduit or ureteral strictures. External urinary drainage detected. Stomal occlusion around the ureteral stent.
Pig 2	Incontinent urinary diversion with lower abdominal wall urostomy and ureteral/conduit stenting for 3 months	0	1	2	3	Stent dislodgement and reinsertion: (post-op days 18, 32, 44, 53, 59, 75).	Patent tubular neotissue with no conduit or ureteral strictures. Perirenal cyst observed. External urinary drainage detected. Stomal area was 24 mm^2
Pig 3	Incontinent urinary diversion with lower abdominal wall urostomy and ureteral/conduit stenting for 3 months	0	0	0	3	Stent dislodgement and reinsertion: (post-op days 59 and 75).	Patent tubular neotissue with no conduit or ureteral strictures. External urinary drainage detected. Stomal area was 87 mm^2
Pig 4	Incontinent urinary diversion with lower abdominal wall urostomy and ureteral/conduit stenting for 3 months	0	2	2	1	Stent dislodgement and reinsertion: (post-op days 31 and 63).	Patent tubular neotissue with no conduit or ureteral strictures. External urinary drainage detected. Stomal area was 63 mm^2
Pig 5	Incontinent urinary diversion with lower abdominal wall urostomy and ureteral/conduit stenting for 3 months	0	2	3	3	Stent dislodgement and reinsertion: (post-op days 38, 51, and 62).	Patent tubular neotissue with no conduit or ureteral strictures. External urinary drainage detected. Stomal area was 75 mm^2

Source: Gundogdu, Gokhan et al. Frontiers in bioengineering and biotechnology vol. 11 (2023). Used with permission.

Figure 2: Imaging Evaluations of Neoconduits and Upper Urinary Tract in Reconstructed Animals

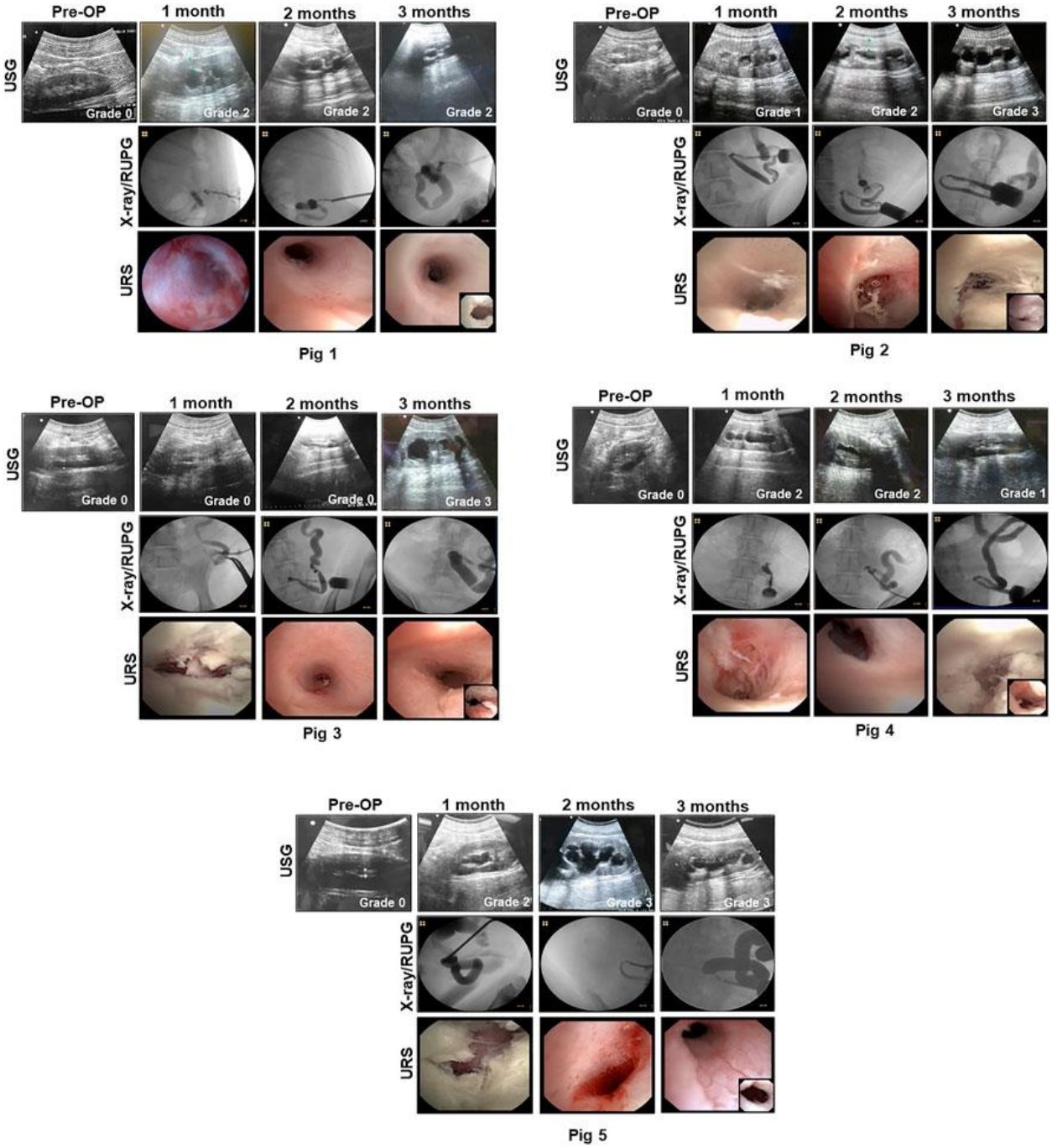

Representative data for Pigs 1–5. USG (top row with hydronephrosis scores), X-ray/RUPG (second row), and URS evaluations of central neoconduits (bottom row, insets showing proximal ureteral anastomosis) were performed at various experimental timepoints. USG, ultrasonography, retrograde ureteropyelogram (RUPG), and uretero-renoscope (URS). Source: Gundogdu, Gokhan et al. Frontiers in bioengineering and biotechnology vol. 11 (2023). Used with permission.

Pig 1 demonstrated diverticular formation at the ureteral-conduit anastomosis at 1 month post-operative and therefore an oblique anastomosis approach was adopted in

subsequent animals which eliminated this problem. Ureteral stent dislodgement and reinsertion occurred 3 times over the course of the implantation period due to hind leg scratching and hence the stomal orifice was repositioned in Pigs two to five to promote stent retention. Extrusion of the BLSF conduit from the stoma occurred at 1 month post-operative in Pig 1 and URS/RUPG evaluations revealed formation of a tubular neotissue. However, stenosis of the stomal orifice was evident at this timepoint as it was fully strictured around the ureteral stent at 3 months resulting in ureteral dilation. Grade 2 hydronephrosis was observed in Pig 1 from 1 to 3 months post-operative in the reconstructed urinary tract putatively due to stomal occlusion. In Pigs two to five, additional conduit stenting approaches were utilized to ameliorate stomal stenosis including placement of a silicone stent during conduit implantation and deployment of a urinary catheter in the distal conduit from 1-3 months post-operative.

Modifications to our initial surgical approach in Pigs two to five had minimal impact on the rate of ureteral and conduit stent dislodgement. Swine required unscheduled stent reinsertion procedures 2–6 times across the study period. However, the use of primary and secondary conduit stents in this cohort did lead to substantial preservation of stomal area with mean values at 3 months post-operative reflecting 65% of the original area. BLSF conduit extrusion from the stomal orifice also occurred in Pigs two to five during 1 month stent exchanges and URS/RUPG analyses demonstrated the presence of tubular neotissues at the original graft site comparable to Pig 1 at this timepoint. Hydronephrosis and ureteral dilation were also detected in Pigs two to five from 1 to 3 months.

Necropsy assessments (**Figure 3**) at 3 months harvest revealed host tissue ingrowth throughout the original graft site in all swine. Neotissues exhibited minimal axial contraction between the proximal/distal marking sutures and no mucosal ulceration was detected. No gross incidence of urinary stone formation or residual bulk biomaterial remnants were observed in the lumen of neotissues. Examination of the reconstructed collecting systems confirmed imaging results and revealed hydronephrosis in all animals with dilation of renal calyces and pelvises as well as hydroureters. A non-communicating perirenal cyst was also identified in Pig 2. These data were in contrast with the unoperated collecting system which demonstrated normal anatomy and no hydronephrosis.

Figure 3: Necropsy Assessments of Neoconduits and Reconstructed Collecting Systems

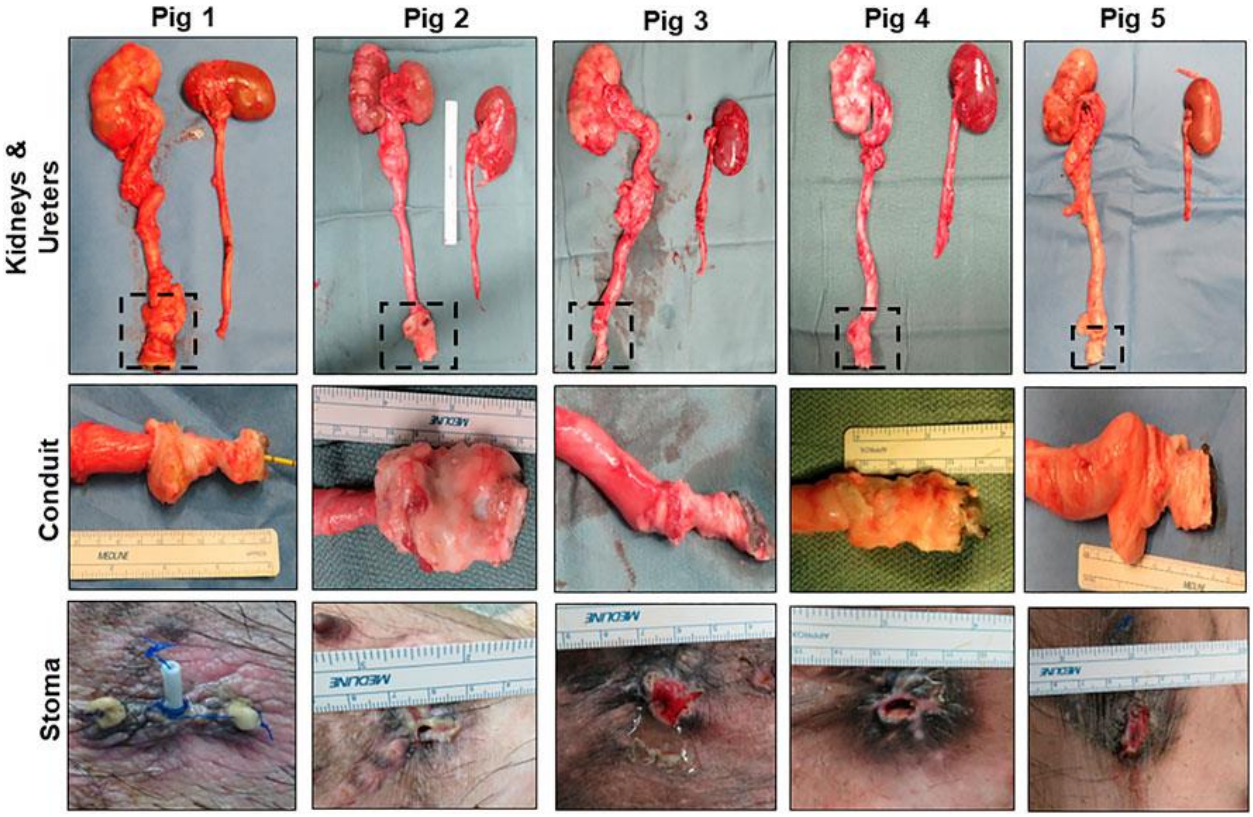

Top row: Photomicrographs of collecting systems and neoconduits (boxed) in Pigs one to five following 3 months of biomaterial implantation as well as parallel non-operated control ureters and kidneys. **Second row:** Magnified axial

view of neoconduits from initial graft regions at harvest. **Bottom row:** Stomal orifice at 3 months post-operative. Source: Gundogdu, Gokhan et al. Frontiers in bioengineering and biotechnology vol. 11 (2023). Used with permission

In all five swine, global histological (MTS) evaluations of neoconduit architecture (**Figure 4**) demonstrated the formation of a collagenous, fibrovascular tube spanning from the ureteral anastomosis to the stoma orifice. Mononuclear inflammatory cells as well as fibroblastic cell types were dispersed throughout the de novo conduit wall. IHC assessments (**Figure 5**) revealed neoconduits contained concentric α-SMA + SM22α+ smooth muscle layers stretching along the entire axial length of the regenerated tissues. However, smooth muscle maturation in neotissues was underdeveloped and consisted of poorly organized, nascent bundles suggesting an ongoing state of tissue remodeling. Indeed, histomorphometric assessments revealed relative immunoreactivity of SM22α and α-SMA expression in stomal and distal regions of neoconduits which was significantly lower in respect to ureteral controls. Sporadic pan-CK + urothelial colonies were detected in the lumen of 4/5 neotissues scattered along the proximal and distal conduit regions. Urothelial differentiation in all neotissues was immature and incompletely stratified with weak UP3A expression in comparison to ureteral controls. Luminal infiltration of pan-CK + skin keratinocytes was also apparent in the distal regions of regenerated segments. In addition, neoconduits were highly vascularized with blood vessels lined with CD31+ endothelial cells apparent throughout all regions of de novo tissues to similar extents and with comparable diameters.

Figure 4: Histological Evaluations of Tissue Regeneration in Neoconduits

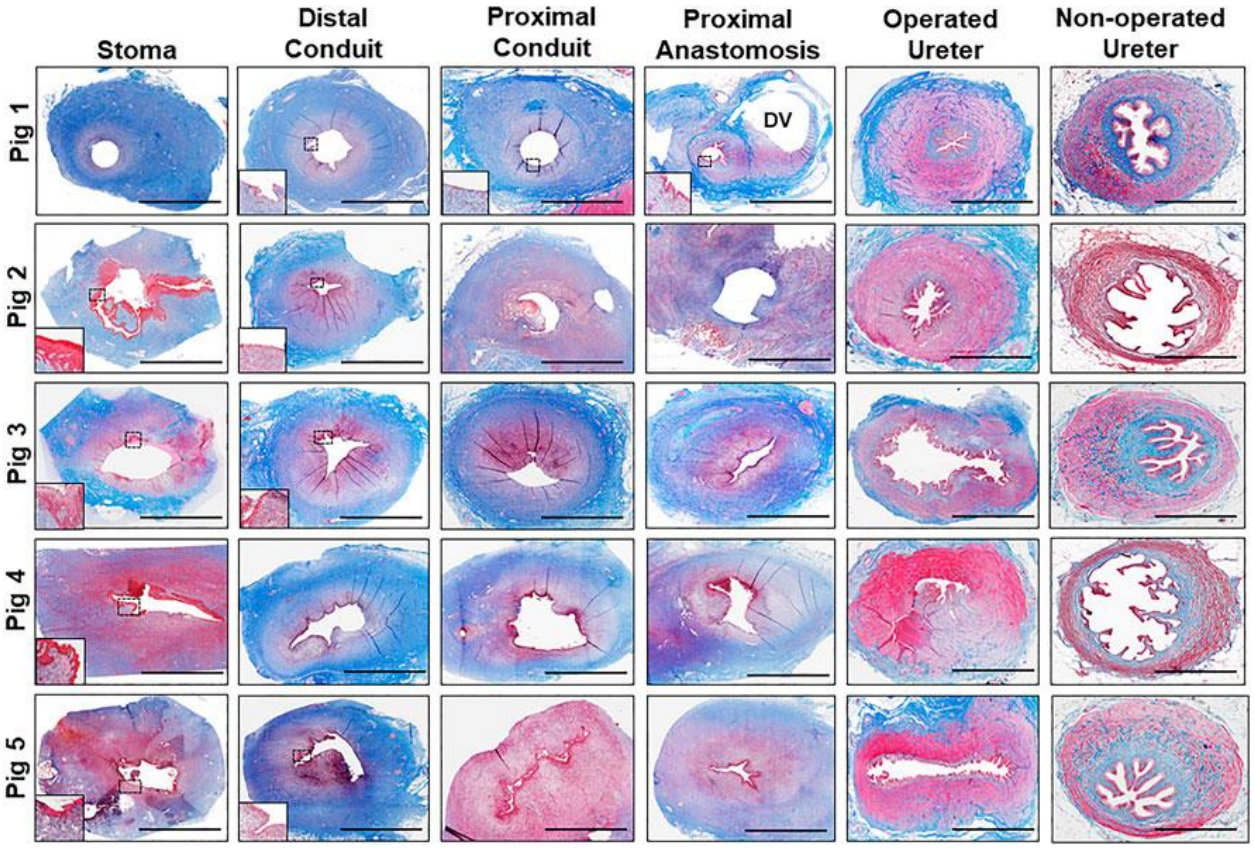

Photomicrographs of neoconduit cross-sections along the axial length (stoma, proximal/distal conduit, proximal anastomosis) as well as control tissues (operated and non-operated ureters) from Pigs one to five stained with Masson's trichrome. Boxed regions denote regions of de novo epithelialization with insets presenting magnified views of neoepithelia. DV denotes diverticula formation in Pig 1. Scale bars for all panels = 1 cm. Source: Gundogdu, Gokhan et al. Frontiers in bioengineering and biotechnology vol. 11 (2023). Used with permission

Figure 5: Immunohistochemical and Histomorphometric Analyses of Neoconduit Maturation

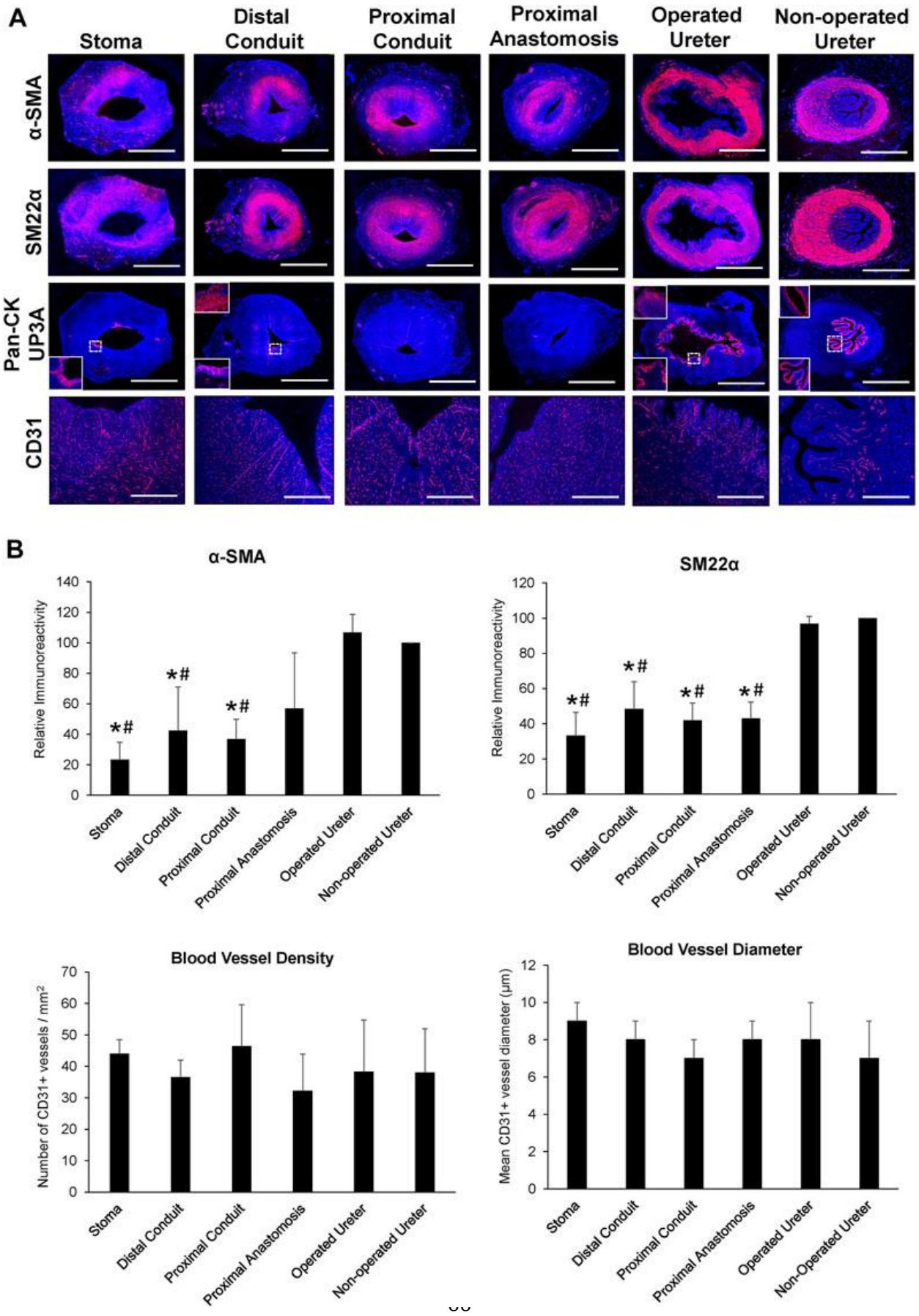
A
Stoma
Distal Conduit
Proximal Conduit
Proximal Anastomosis
Operated Ureter
Non-operated Ureter
α-SMA
SM22α
Pan-CK UP3A
CD31
B
α-SMA
Relative Immunoreactivity
SM22α
Relative Immunoreactivity
Blood Vessel Density
Number of CD31+ vessels / mm²
Blood Vessel Diameter
Mean CD31+ vessel diameter (μm)
Stoma
Distal Conduit
Proximal Conduit
Proximal Anastomosis
Operated Ureter
Non-operated Ureter
Non-Operated Ureter

[A] Representative photomicrographs of selective protein expression in neoconduit regions (stoma, proximal/distal conduit, proximal anastomosis) and control tissues (operated and non-operated ureters) from Pig 3. Markers include smooth muscle contractile proteins (first and second rows: α-SMA, SM22α), epithelial proteins (third row: pan-CK, global images and bottom insets magnified from boxed area; UP3A: top insets), and vascular endothelial CD31 (fourth row). For all panels, respective marker expression is labeled in red (Alexa Fluor 594 labeling) with DAPI nuclear counterstain displayed in blue. Scale bars = 1 cm for each panel. α-SMA, a-smooth muscle actin; CK, cytokeratin; DAPI, 4′, 6-diamidino-2-phenyllindole; UP3A, uroplakin 3A. **[B]** Quantitative evaluations of markers detailed in panel A for Pigs 1–5. Data are presented as means ± SD. Results from all cohorts were analyzed with Kruskal–Wallis and post hoc Dunn's tests. P⟨ 0.05 relative to respective operated (*) and non-operated (#) ureteral controls. Source: Gundogdu, Gokhan et al. Frontiers in bioengineering and biotechnology vol. 11 (2023). Used with permission

3.4 Discussion

Current urinary diversion techniques require harvesting and incorporation of autologous GI tissues into the urinary tract which can lead to undesirable acute and chronic complications while negatively impacting upon a patient's quality of life.[27,29] To date, despite years of research into the utility of acellular and cell-seeded grafts as tissue engineered alternatives, there is no FDA-approved medical device for urinary diversion. Conventional decellularized tissue matrices and synthetic meshes have been explored in past reports as candidates for TEUC, however suboptimal material properties have led to chronic inflammatory reactions, scar tissue formation, stomal stenosis and conduit strictures, thus precluding clinical translation.[10,15,16,18,19] BLSF grafts have shown promise for hollow organ reconstruction in preclinical studies and demonstrated superior regenerative outcomes relative to commercial SIS matrices previously deployed as urinary conduits.[30,31] Therefore, the goal of this study was to determine the feasibility of tubular BLSF biomaterials to serve as a urinary conduit in a porcine model of urinary diversion. Longitudinal imaging was conducted to monitor upper urinary tract function and neoconduit performance, while histological and IHC analyses were deployed to characterize the extent of tissue regeneration in reconstructed areas over the course of 3 months of implantation.

Overall, our data provide evidence that BLSF constructs in combination with ureteral/conduit stenting can support formation of vascularized, retroperitoneal tubes capable of facilitating external urinary drainage. However, the degree of tissue maturation in neoconduits at harvest at 3 months was incomplete with discontinuous smooth muscle layers and sparse epithelialization relative to ureteral controls. Moderate hydronephrosis and hydroureters were detected in all reconstructed animals and may be linked to deficiencies in neoconduit peristalsis as a result of limited smooth muscle regeneration. In addition, partial urinary tract obstruction from the presence of the conduit stent as well as aperistalsis from prolonged ureteral stenting may have also contributed to observed kidney and ureteral pathologies. Similar to our past studies in a porcine tubular ureteroplasty model, de novo tissue formation originated from ureteral tissue ingrowth which propagated along the exterior of the BLSF graft wall from the anastomotic border to the stomal orifice. Following bulk scaffold extrusion at 1 month, URS findings showed neomucosa spanning the entire surface of reconstructed segments suggesting neotissue expansion into implant sites led to matrix displacement and prolapse into the lumen. Comparable wound healing patterns have been reported with the use of stented PGLA-coated, PGA scaffolds as acellular urinary conduits in porcine models.[12] BLSF biomaterials remained grossly intact in vivo, but could be easily extruded from the stomal orifice after neotissue formation potentially diminishing the risk of chronic foreign body reactions and urinary tract obstruction. Previous assessments of BLSF grafts for tubular ureteroplasty demonstrated similar degrees of degradation, however graft persistence in distal segments resulted in urinary blockage and severe renal damage.[25]

Stenting of acellular urinary conduits has been reported to mitigate stomal stenosis and maintain patency of regenerated tissues by reinforcing luminal mechanical integrity during tissue remodeling.[12] These results are comparable to our current findings wherein conduit stenting reduced stomal occlusion relative to untreated controls and preserved 65% of the original stomal area. Stent dislodgement occurred frequently in our animal model necessitating periodic stent exchanges to maintain stomal caliber. These manipulations may have disrupted urothelial growth and stratification in regenerated tissues due to mucosal abrasions acquired during stent deployment. Future improvements in our matrix design will focus on increasing the radial force exerted by BLSF constructs to improve graft retention and prevent stomal stenosis in the absence of stenting. Material properties including initial SF content and scaffold pore size have been implicated as significant regulators of compressive strength and stiffness in aqueous-based SF foams.[32] These findings suggest that the radial strength and stiffness of the foam compartment of BLSF grafts may be enhanced to prevent stenotic events by increasing the concentration of SF used during casting or by reducing matrix pore size via modulation of porogen diameter. In addition, SF biomaterials have also been reported to serve as targeted drug delivery systems both in vivo and in vitro for a variety of agents including small molecules, cytokines, nucleic acids, and antibodies.[33] The creation of next-generation, BLSF conduits with the capacity to stimulate smooth muscle and urothelial formation via controlled release of respective differentiation agonists such as bone morphogenetic protein-4[34] and retinoic acid[35] may promote increased levels of functional tissue regeneration in neoconduits.

3.5 References

1) Kates, Max et al. “Tissue-engineered urinary conduits.” Current urology reports vol. 16,3 (2015): 8. doi:10.1007/s11934-015-0480-3

2) Adamowicz, Jan et al. “Constructing artificial urinary conduits: current capabilities and future potential.” Expert review of medical devices vol. 16,2 (2019): 135-144. doi:10.1080/17434440.2019.1562901

3) Lee, Richard K et al. “Urinary diversion after radical cystectomy for bladder cancer: options, patient selection, and outcomes.” BJU international vol. 113,1 (2014): 11-23. doi:10.1111/bju.12121

4) Stein, Raimund, and Peter Rubenwolf. “Metabolic consequences after urinary diversion.” Frontiers in pediatrics vol. 2 15. 10 Mar. 2014, doi:10.3389/fped.2014.00015

5) Dobruch, Jakub et al. “Gender and Bladder Cancer: A Collaborative Review of Etiology, Biology, and Outcomes.” European urology vol. 69,2 (2016): 300-10. doi:10.1016/j.eururo.2015.08.037

6) van Hemelrijck, Mieke et al. “Risk of in-hospital complications after radical cystectomy for urinary bladder carcinoma: population-based follow-up study of 7608 patients.” BJU international vol. 112,8 (2013): 1113-20. doi:10.1111/bju.12239

7) Falagas, Matthew E, and Paschalis I Vergidis. “Urinary tract infections in patients with urinary diversion.” American journal of kidney diseases : the official journal of the National Kidney Foundation vol. 46,6 (2005): 1030-7. doi:10.1053/j.ajkd.2005.09.008

8) Okhunov, Zhamshid et al. “Management of urolithiasis in patients after urinary diversions.” BJU international vol. 108,3 (2011): 330-6. doi:10.1111/j.1464-410X.2011.10194.x

9) Stein, Raimund et al. “Urinary diversion--approaches and consequences.” Deutsches Arzteblatt international vol. 109,38 (2012): 617-22. doi:10.3238/arztebl.2012.0617

10) Sloff, Marije et al. “Tissue engineering in animal models for urinary diversion: a systematic review.” PloS one vol. 9,6 e98734. 25 Jun. 2014, doi:10.1371/journal.pone.0098734

11) Bodin, Aase et al. “Tissue-engineered conduit using urine-derived stem cells seeded bacterial cellulose polymer in urinary reconstruction and diversion.” Biomaterials vol. 31,34 (2010): 8889-901. doi:10.1016/j.biomaterials.2010.07.108

12) Basu, Joydeep et al. “Regeneration of native-like neo-urinary tissue from nonbladder cell sources.” Tissue engineering. Part A vol. 18,9-10 (2012): 1025-34. doi:10.1089/ten.TEA.2011.0569

13) Drewa, Tomasz et al. “Tissue engineering for the oncologic urinary bladder.” Nature reviews. Urology vol. 9,10 (2012): 561-72. doi:10.1038/nrurol.2012.158

14) Geutjes, Paul et al. “Tissue engineered tubular construct for urinary diversion in a preclinical porcine model.” The Journal of urology vol. 188,2 (2012): 653-60. doi:10.1016/j.juro.2012.03.119

15) Liao, Wenbiao et al. “Tissue-engineered tubular graft for urinary diversion after radical cystectomy in rabbits.” The Journal of surgical research vol. 182,2 (2013): 185-91. doi:10.1016/j.jss.2012.10.024

16) Liao, Wen-Biao et al. “Tissue-engineered conduit using bladder acellular matrix and bladder epithelial cells for urinary diversion in rabbits.” Chinese medical journal vol. 126,2 (2013): 335-9.

17) Reinfeldt Engberg, Gisela et al. “Transplantation of autologous minced bladder mucosa for a one-step reconstruction of a tissue engineered bladder conduit.” BioMed research international vol. 2013 (2013): 212734. doi:10.1155/2013/212734

18) Bivalacqua, T., et al. "178 Pre-clinical and clinical translation of a tissue engineered neo–urinary conduit using adipose derived smooth muscle cells for urinary reconstruction." European Urology Supplements 1.13 (2014): e178.

19) Bivalacqua, Trinity, et al. "MP61-16 PRE-CLINICAL AND CLINICAL TRANSLATION OF A TISSUE ENGINEERED NEO– URINARY CONDUIT USING ADIPOSE DERIVED SMOOTH MUSCLE CELLS FOR URINARY RECONSTRUCTION." The Journal of Urology 191.4S (2014): e689-e689.

20) Sloff, Marije et al. “Tubular Constructs as Artificial Urinary Conduits.” The Journal of urology vol. 196,4 (2016): 1279-86. doi:10.1016/j.juro.2016.04.092

21) Singh, Anirudha et al. “Tissue-Engineered Neo-Urinary Conduit from Decellularized Trachea.” Tissue engineering. Part A vol. 24,19-20 (2018): 1456-1467. doi:10.1089/ten.TEA.2017.0436

22) Jundziłł, Arkadiusz et al. “A tissue-engineered urinary conduit in a porcine urinary diversion model.” Scientific reports vol. 11,1 16754. 18 Aug. 2021, doi:10.1038/s41598-021-94613-7

23) Casarin, Martina et al. “Porcine Small Intestinal Submucosa (SIS) as a Suitable Scaffold for the Creation of a Tissue-Engineered Urinary Conduit: Decellularization, Biomechanical and Biocompatibility Characterization Using New Approaches.” International journal of molecular sciences vol. 23,5 2826. 4 Mar. 2022, doi:10.3390/ijms23052826

24) Seth, Abhishek et al. “The performance of silk scaffolds in a rat model of augmentation cystoplasty.” Biomaterials vol. 34,20 (2013): 4758-65. doi:10.1016/j.biomaterials.2013.03.038

25) Gundogdu, Gokhan et al. “Evaluation of Bi-Layer Silk Fibroin Grafts for Tubular Ureteroplasty in a Porcine Defect Model.” Frontiers in bioengineering and biotechnology vol. 9 723559. 17 Sep. 2021, doi:10.3389/fbioe.2021.723559

26) Onen, Abdurrahman. “An alternative grading system to refine the criteria for severity of hydronephrosis and optimal treatment guidelines in neonates with primary UPJ-type

hydronephrosis." Journal of pediatric urology vol. 3,3 (2007): 200-5. doi:10.1016/j.jpurol.2006.08.002

27) Rangarajan, Karan, and Bhaskar K Somani. "Trends in quality of life reporting for radical cystectomy and urinary diversion over the last four decades: A systematic review of the literature." Arab journal of urology vol. 17,3 181-194. 14 Apr. 2019, doi:10.1080/2090598X.2019.1600279

28) Affas, Saif et al. "Augmentation Cystoplasty of Diseased Porcine Bladders with Bi-Layer Silk Fibroin Grafts." Tissue engineering. Part A vol. 25,11-12 (2019): 855-866. doi:10.1089/ten.TEA.2018.0113

29) Anderson, Christopher B, and James M McKiernan. "Surgical Complications of Urinary Diversion." The Urologic clinics of North America vol. 45,1 (2018): 79-90. doi:10.1016/j.ucl.2017.09.008

30) Chung, Yeun Goo et al. "Acellular bi-layer silk fibroin scaffolds support tissue regeneration in a rabbit model of onlay urethroplasty." PloS one vol. 9,3 e91592. 14 Mar. 2014, doi:10.1371/journal.pone.0091592

31) Chung, Yeun Goo et al. "The use of bi-layer silk fibroin scaffolds and small intestinal submucosa matrices to support bladder tissue regeneration in a rat model of spinal cord injury." Biomaterials vol. 35,26 (2014): 7452-9. doi:10.1016/j.biomaterials.2014.05.044

32) Kim, Ung-Jin et al. "Three-dimensional aqueous-derived biomaterial scaffolds from silk fibroin." Biomaterials vol. 26,15 (2005): 2775-85. doi:10.1016/j.biomaterials.2004.07.044

33) Wani, Shahid Ud Din, and Gangadharappa Hosahalli Veerabhadrappa. "Silk Fibroin Based Drug Delivery Applications: Promises and Challenges." Current drug targets vol. 19,10 (2018): 1177-1190. doi:10.2174/1389450119666171227205525

34) Wang, Gerald J et al. "Antagonism of BMP4 signaling disrupts smooth muscle investment of the ureter and ureteropelvic junction." The Journal of urology vol. 181,1 (2009): 401-7. doi:10.1016/j.juro.2008.08.117

35) Gandhi, Devangini et al. "Retinoid signaling in progenitors controls specification and regeneration of the urothelium." Developmental cell vol. 26,5 (2013): 469-482. doi:10.1016/j.devcel.2013.07.017

Chapter 4: Silk Fibroin Matrices for Onlay Vaginoplasty in Rats

4.1 Objective

The objective of this study to evaluate the efficacy of BLSF grafts for focal vaginal tissue repair in a rat model.

4.2 Methods

4.2.1 Biomaterials

BLSF biomaterials were manufactured from aqueous silk fibroin solutions using established protocols.[13] Briefly, sericin-depleted, silk fibroin solutions (8% weight/volume) derived from Bombyx mori cocoons were dried for 48 hours at room temperature in a casting container under laminar flow to create a silk fibroin film. A 6% weight/volume silk fibroin solution was then mixed with sieved granular NaCl (500–600 μM, average crystal diameter) in a ratio of 2 g NaCl per ml of silk fibroin solution and deposited on top of the silk fibroin film. The resultant solution was allowed to undergo self-assembly and fuse to the silk fibroin film for 48 hours at 37 °C to create the BLSF matrix. NaCl was removed thereafter by rinsing the scaffold for 72 hours in distilled water. BLSF grafts were trimmed and steam sterilized in an autoclave prior to implantation. Commercially available, SIS scaffolds (Biodesign 4-Layer Tissue Graft; Cook Medical, Bloomington, IN, United States) were evaluated in parallel animal studies as points of comparison.

4.2.2 Study Design

All animal procedures were performed in compliance with the National Institutes of Health's Guidelines for the Care and Use of Laboratory Animals and were reviewed and approved by the University of California, Irvine Animal Care and Use Committee in accordance with protocol AUP-22-009. Forty-two adult, virgin female Sprague-Dawley rats (240-280 g, Charles River Laboratories, Charles River Laboratories, Wilmington, MA) were randomized across 2 implant groups and subjected to inlay vaginoplasty (**Figure 1**) with either BLSF (N=21) or SIS (N=21) grafts as described below. Animals in both scaffold groups were harvested for outcome analyses at 1 day (N=3 per implant), 1 week (N=4 per implant), 1 month (N=5 per implant) and 2 months (N=5 per implant) post-operatively to determine longitudinal wound healing and host tissue responses. Nonsurgical controls (NSC) (N=4) were analyzed in parallel and served as positive controls. In addition, breeding experiments were carried out with rats from both matrix groups (N=4 per implant) 2 months following vaginal reconstruction to assess copulation and delivery functions as detailed in subsequent sections.

Figure 1: Rat Inlay Vaginoplasty

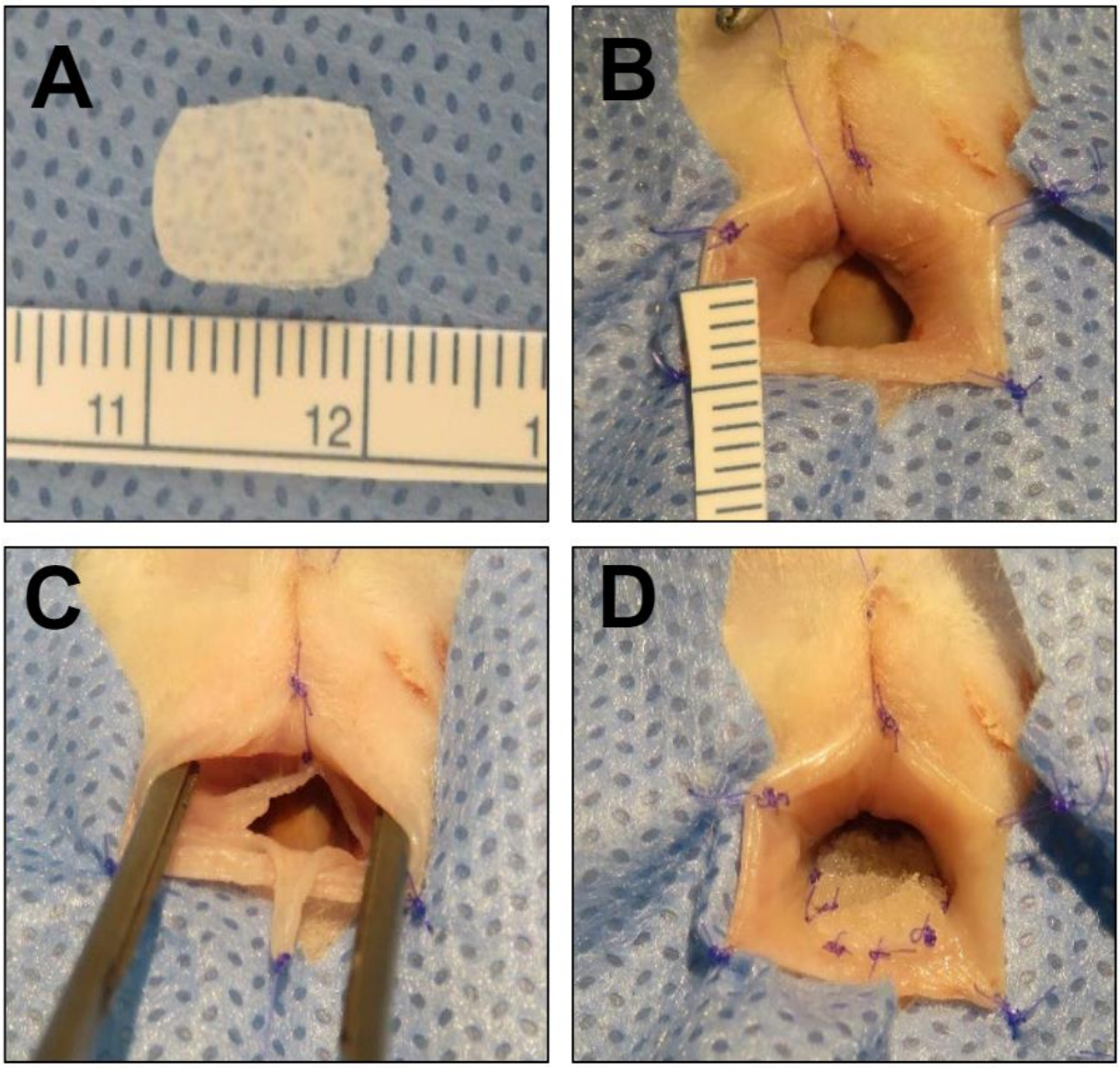

[A] Photomicrograph of BLSF graft prior to vaginal implantation. **[B]** Suture retraction of the vaginal introitus exposing the posterior vaginal wall. **[C]** Creation of vaginal defect in the posterior vagina. **[D]** Vaginal reconstruction with BLSF graft.

4.2.3 Inlay vaginoplasty

General anesthesia was induced and maintained by inhalation with 2–4% isoflurane. Rats were placed in a supine position and the perineum was shaved and sterilely draped. The vaginal introitus was retracted with stay sutures and a full thickness defect

(10 x 5 mm2) was created in the posterior vaginal wall 1-2 mm proximal from the orifice. A graft of equal size was incorporated into the defect area with 7-0 polyglactin interrupted sutures. Nonabsorbable 7-0 polypropylene sutures were placed along the anastomotic perimeter for delineation of matrix borders following sacrifice. Postoperative pain control was accomplished by a single subcutaneous injection of 1.2 mg/kg Buprenorphine SR (ZooPharm, Laramie, WY, United States) immediately following surgery with subcutaneous injections of 2.5 mg/kg Banamine (Merck Animal Health, Kenilworth, NJ, United States) carried out for 3 days post-operatively. In addition, Enrofloxacin (Baytril®100; Bayer Healthcare LLC, KA, United States) was administered subcutaneously before surgery and continued for 2 postoperative days to prevent infection. At selected timepoints, rats were subjected to imaging and/or breeding analyses and then euthanized by CO2 asphyxiation for histological and immunohistochemical (IHC) assessments.

4.2.4 Micro–computed tomography

Micro–computed tomography (μCT) was performed on NSC (N = 4) and implant groups (N=5 per scaffold) at 2 months following vaginoplasty to evaluate organ continuity and structure. Under isofluorane anesthesia, rats were placed in the supine position and a purse string was placed at the skin level of the vaginal introitus using a 5-0 nonabsorbable suture. A 14 gauge IV cannula was then introduced into the vagina and secured with a purse string. Contrast medium (Omnipaque 300; GE Healthcare Inc., Marlborough, MA, USA) diluted with 1:1 saline was infused into the vagina followed by cannula removal and closure of the vaginal orifice. Lower abdomen scans were acquired with a Siemens Inveon(r) Multi-Modality System PET/CT (Siemens Healthcare, Erlangen, Germany) and 3-

D images of the vaginal lumen were created using Inveon Research Workplace (Siemens Healthcare) 3D Analysis software.

4.2.5 Breeding and live birth assessments

Following 2 months of scaffold implantation, rats subjected to vaginal repair with BLSF and SIS matrices (N=4 per matrix) were evaluated for their ability to copulate, achieve pregnancy and deliver live births. Each female was co-housed with one male rat for 2 weeks to allow for mating. Pregnancy was confirmed by monitoring abdominal distension, weight and breast development over the gestational period. The rate of pregnancy and number of live births were quantified across groups.

4.2.6 Histological, IHC, and histomorphometric analyses

Following euthanasia, reconstructed vaginal segments (N=3-5 per timepoint) as well as NSC replicates (N=4) were formalin fixed for 12 hours, dehydrated in graded alcohols and embedded in paraffin for sectioning. Specimens (5 μm) were stained with Masson's trichrome (MTS), digitally imaged and total collagen content was determined in control and implant regions with ImageJ software (version 1.47) using published methods to quantify blue-stained color elements representative of collagen deposition.[14] Total collagen content was calculated as the percentage of blue-stained area per total field area and normalized to NSC levels. IHC analyses were carried out on parallel tissue sections following antigen retrieval (pH 6.0, 10 mm sodium citrate buffer) and incubation in phosphate-buffered saline with 0.3% Triton X-100, 5% fetal bovine serum, and 1% bovine serum albumin for 1 hour at room temperature. Sections were probed at 4ºC overnight with primary antibodies including anti-α-smooth muscle actin (SMA) (1:200 dilution;

Sigma-Aldrich, St. Louis, MO), anti-SM22α (1:200 dilution, Abcam, Cambridge, MA), anti-pan-cytokeratin (CK) (1:150 dilution; Dako, Carpinteria, CA), anti-CD31 (1:100 dilution; Abcam) and vimentin (1:100 dilution; Abcam). Samples were then stained with species-matched Alexa Fluor 647 and 488-conjugated secondary antibodies (Thermo Fisher Scientific) and nuclear counterstained with 4′, 6-diamidino-2-phenyllindole (DAPI). Specimen visualization was performed with an Axioplan-2 microscope (Carl Zeiss MicroImaging, Thornwood, NY) and representative fields were acquired with Axiovision software (version 4.8). Negative controls were stained in parallel with secondary antibodies alone and generated no detectable signal above background. Histomorphometric evaluations were performed on NSC (N=4) and neotissues (N=3-5 per timepoint) utilizing 6-8 independent microscopic fields (10X magnification). Stained elements were quantified from specimen cross-sections with published protocols using ImageJ software.[15] Relative immunoreactivities of α-SMA, SM22α, vimentin and pan-CK were presented as the percentage of stained area per total field area relative to NSC values. Vascular densities were determined similarly by quantifying the number of CD31+ vessels per target field area.

4.2.7 Statistical Evaluations

Multi-group comparisons were carried out with the Kruskal Wallis test followed by pairwise evaluations with the post hoc Dunn's test. For two group comparisons of live birth data, the Mann-Whitney U test was utilized. For all statistical tests, $p<0.05$ was defined as significant. All quantitative data were displayed as means ± standard deviation (SD).

4.3 Results

Animals in both implant cohorts exhibited 100% survival rates until scheduled euthanasia. In addition, there was no evidence of serve intraoperative or postoperative complications following vaginoplasty in either group over the course of the study, however mild hematomas were detected at the reconstructed sites in 3 rats prior to sacrifice (BLSF: N=2, 1 day post-op; SIS: N=1, 2 months post-op). At 2 months post-op, μCT imaging revealed normal vaginal anatomy in both graft groups similar to NSC with no signs of contrast extravasation, strictures or fistula formation (**Figure 2**). These observations were confirmed during parallel necropsy evaluations wherein patent vaginal canals with wide calibers were evident in both BLSF and SIS groups. Residual scaffold fragments were found in the vaginal lumens of both biomaterial cohorts up to 1 month post-reconstruction, but were undetectable by the 2 month timepoint. Host tissue ingrowth was apparent throughout the original reconstructed areas in both experimental groups by 1 week post-op with negligible tissue contraction detected between proximal/distal or lateral marking sutures at harvest (**Figure 2**). These results demonstrate that BLSF grafts are capable of supporting consolidation of focal vaginal defects and restoring organ continuity to similar extents as conventional SIS matrices.

Figure 2: Necropsy and μCT Analyses of Neotissue Formation and Vaginal Continuity

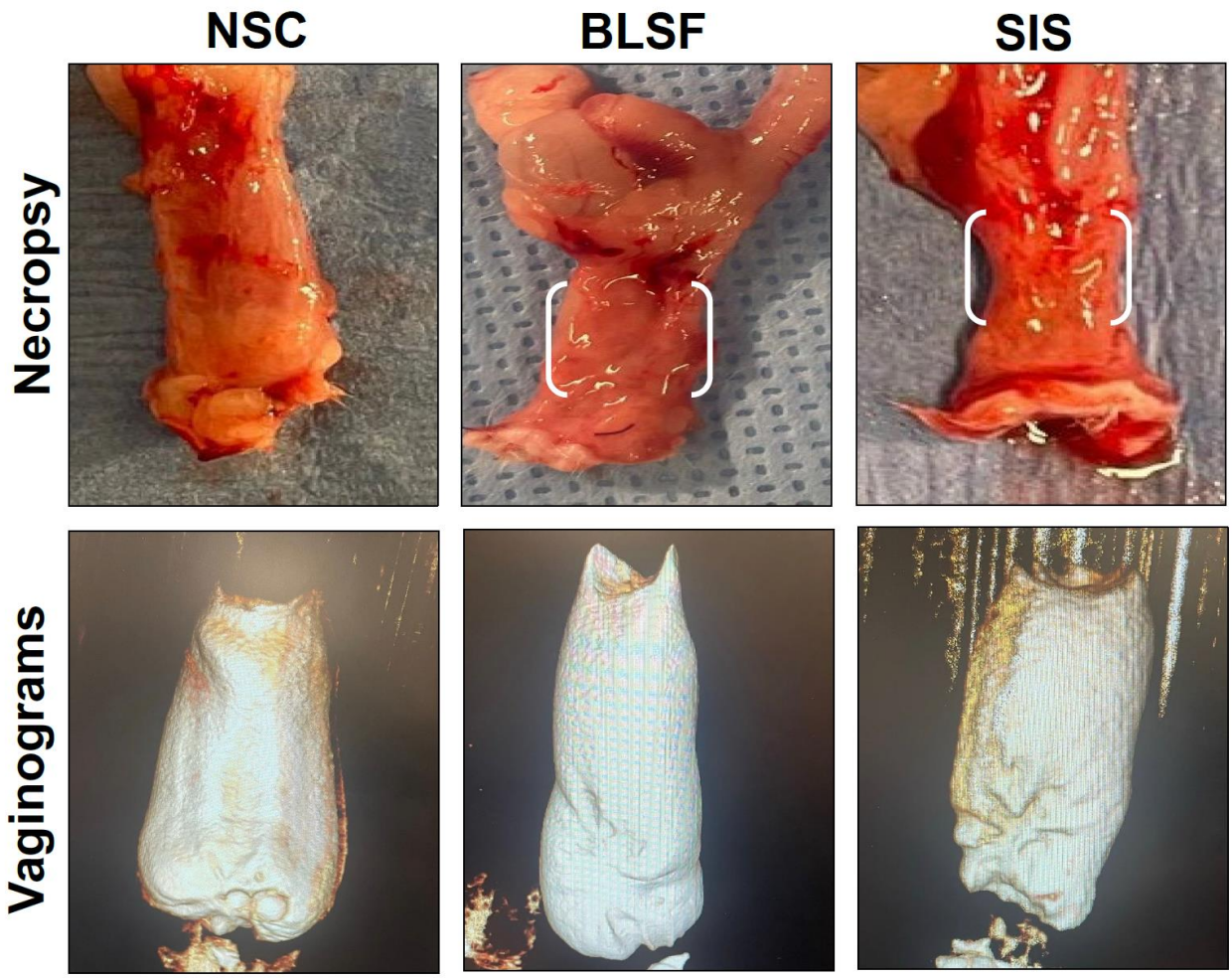

[Top row] Gross tissue assessments of vaginas reconstructed with BLSF or SIS grafts following 2 months of implantation in comparison to NSC. Boxed regions denote original implant site. **[Bottom row]** Representative 3-D images of vaginas in NSC and scaffold groups detailed in [A] following contrast instillation and μCT imaging.

Characterization of host tissue responses and wound healing outcomes were performed on control and implant groups across the study period with histologic, IHC and histomorphometric analyses (**Figure 3 and 4**). Baseline evaluations of vaginal cross-sections in NSC revealed native tissue architecture composed of a luminal, stratified squamous, keratinizing epithelium with pan-CK expression, an extra-cellular matrix (ECM)-rich lamina propria populated with vimentin+ fibroblasts and an outer muscularis layer consisting of circular and longitudinal smooth muscle bundles displaying contractile proteins, α-SMA and SM22α. By 1 day post-op, MTS evaluations demonstrated that

reconstructed regions in each scaffold group exhibited nascent ECM formation and were infiltrated with mononuclear inflammatory cells, neutrophils, and fibroblasts. Prominent extrusion of bulk scaffold fragments into the vaginal lumen was also observed in each group at this phase of repair. At 1 week post-op, neotissues in each experimental group had developed a vascularized lamina propria lined by a pan-CK+ stratified squamous, keratinizing epithelium similar to NSC. Transient myofibroblast differentiation was also detected in remodeling vaginal walls at this stage exemplified by significant upregulation of vimentin expression compared to NSC and co-expression of α-SMA and SM22α proteins in this population. Maturation of neotissues in each implant cohort continued to progress between 1 week and 2 months with the formation of α-SMA+SM22α+ smooth muscle bundles coupled with a parallel decline in vimentin+myfibroblasts to baseline levels. Reconstructed tissues also displayed similar degrees of collagen content compared to NSC by 1 and 2 months post implantation. In addition, no evidence of chronic inflammatory reactions or foreign body responses were observed in either neotissue at study timepoints.

Figure 3: Histological Assessments of Vaginal Tissue Regeneration

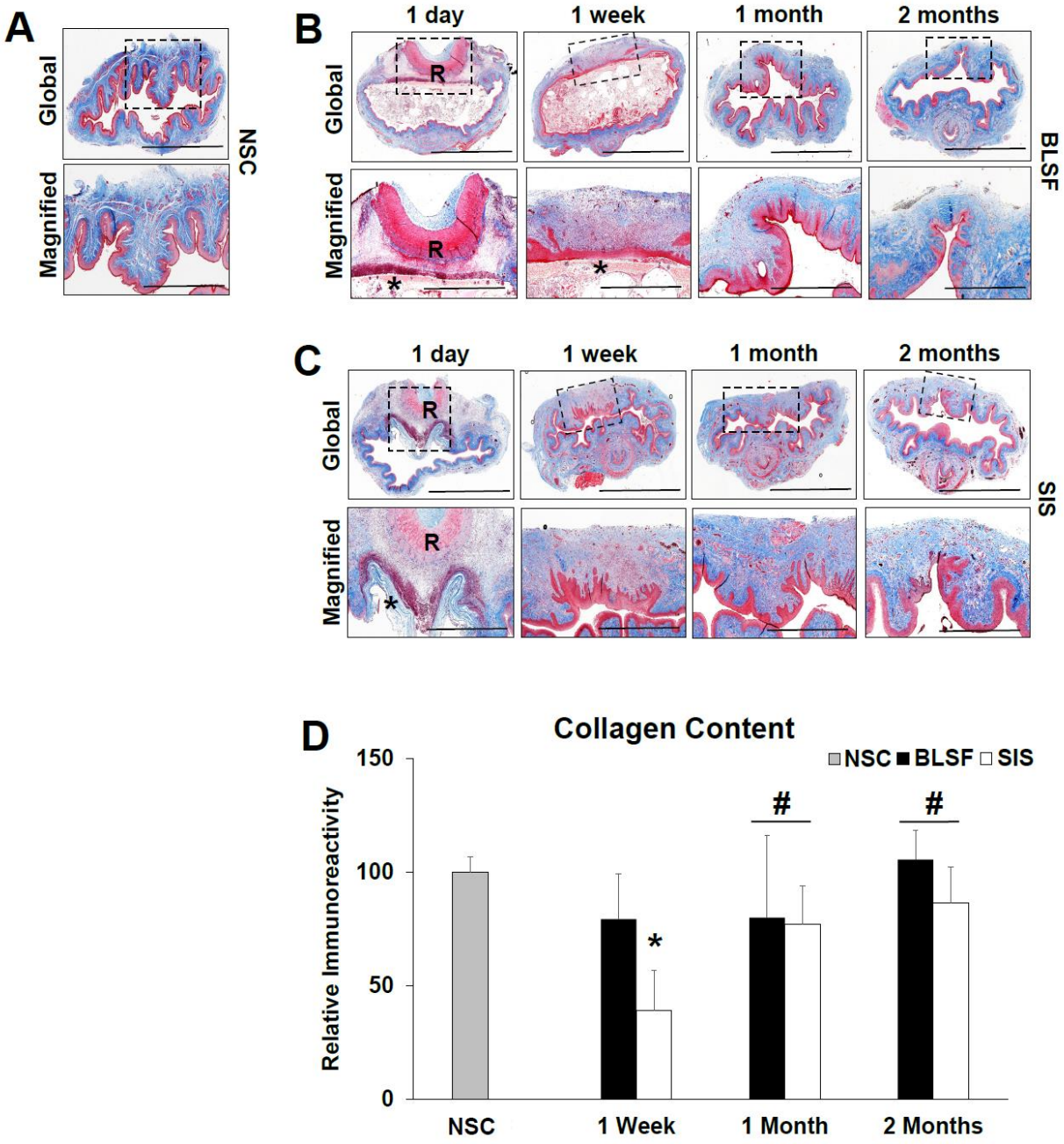

[A-C] Photomicrographs of global (top rows) and magnified (bottom rows) cross-sections of MTS-stained, vaginas in NSC **[A]** and in animals repaired with BLSF **[B]** and SIS grafts **[C]** at selective post-operative timepoints containing the original implant site (boxed). For panels [A-C], scale bars are 2.5 mm and 1 mm in top and bottom rows, respectively. R denotes rectum. Asterisks denote residual scaffold fragments. **[D]** Quantitation of collagen content in MTS-stained vaginal neotissues and NSC displayed in [A-C]. N=3-5 rats per group were assessed per data point. Data are displayed as means ± SD. Data from all cohorts were analyzed with Kruskal–Wallis and post hoc Dunn's tests. (*) = $p<0.05$ compared to NSC. (#) = $p<0.05$ compared to NSC.

Figure 4: Immunohistochemical and Histomorphometric Evaluations of Vaginal Neotissues and Controls

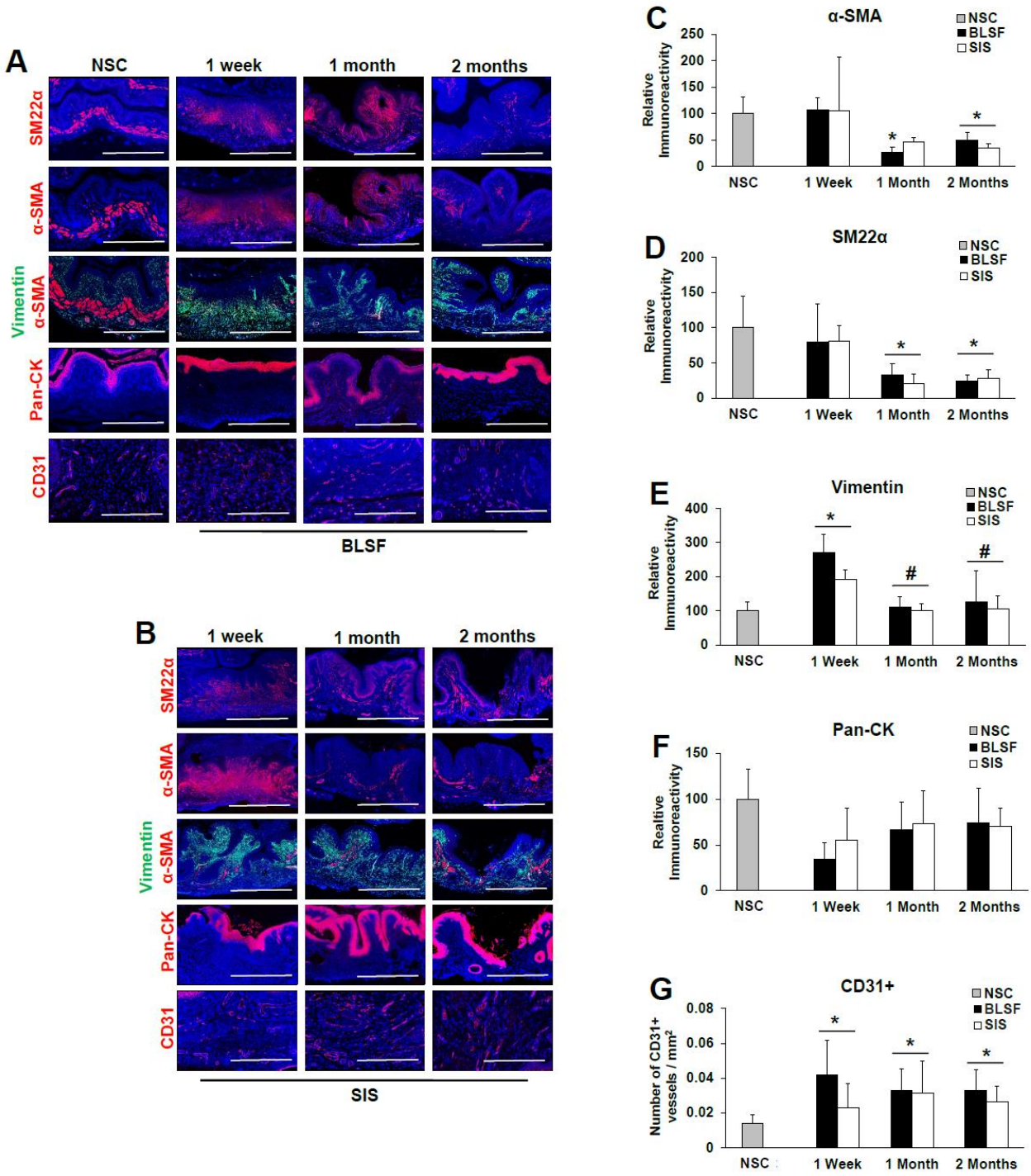

[A-B] Photomicrographs of vaginal protein expression in NSC and regenerated tissues following vaginoplasty with BLSF **[A]** and SIS **[B]** biomaterials at selective stages of repair. For all images, respective marker expression is labeled in red (Alexa Fluor 647 labeling) or green (Alexa Fluor 488 labeling) with blue DAPI nuclear counterstain. Scale bars for all panels = 200 μm. **[C-G]** Histomorphometric assessments of marker expression in specimens described in **[A-B]**. N=3-5 rats per group were assessed per data point. Data are displayed as means ± SD. Results from all groups were evaluated with Kruskal–Wallis and post hoc Dunn's tests. (*) = $p<0.05$ compared to NSC. (#) = $p<0.05$ compared to respective 1 week timepoint.

Overall, no significant differences in regenerative outcomes were found between SIS and BLSF groups suggesting vaginal wound healing patterns were conserved across these implant configurations. However, neotissues from each scaffold cohort were still underdeveloped at 2 months and displayed 25-50% smooth muscle content relative to NSC as well as significantly higher vascular densities consistent with ongoing phases of tissue remodeling. Nevertheless, breeding assessments (**Figure 5**) revealed that animals repaired with both BLSF and SIS biomaterials were capable of copulation with 100% pregnancy rates and similar amounts of live births. These data provide evidence that BLSF grafts can promote functional vaginal tissue regeneration sufficient to support sexual intercourse and delivery of live offspring.

Figure 5: Breeding and Live Birth Evaluations in Implant Groups

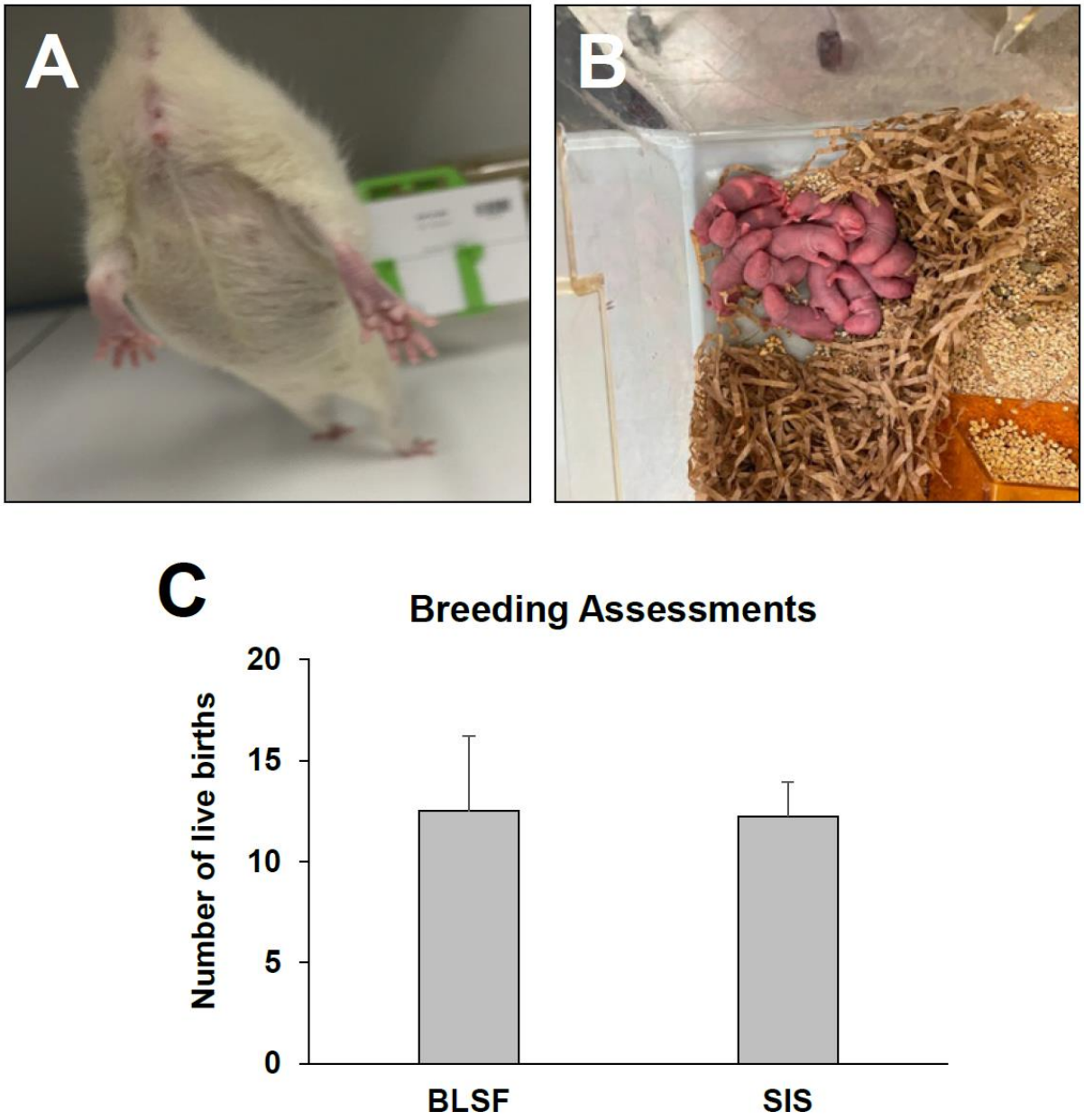

[A] Representative photomicrograph of a pregnant rat exhibiting abdominal distension and breast development following vaginal repair with a BLSF graft. **[B]** Live neonatal rat pups delivered from rats described in **[A]**. **[C]** Quantitation of live births from each implant group. N=4 per data point. Data are displayed as means ± SD. Results were analyzed with the Mann–Whitney U test yielding p=0.89.

4.4 Discussion

The aims of this study were to evaluate the feasibility of acellular BLSF grafts for vaginal reconstruction and compare functional and wound healing responses to

decellularized SIS biomaterials previously deployed in the clinic. Adult rats were chosen as a model species due to their low cost as well as their similarities in organ anatomy and reproductive cycle relative to humans.[16] The regenerative potential of study biomaterials was investigated in an inlay vaginoplasty model which mimics the repair of focal vaginal defects encountered in patients following resection of urogenital malignancies[17,18] or those with severe obstetric lacerations after childbirth.[19] BLSF and SIS grafts were found to induce similar constructive remodeling patterns in patch vaginal defects and were histologically equivalent in their ability to support the formation of vascularized neotissues containing stratified squamous, keratinizing epithelia as well as smooth muscle layers. However, smooth muscle content was significantly lower in neotissues relative to NSC suggesting longer implantation periods or scaffold-mediated, delivery of pro-myogenic compounds such as platelet derived growth factor[20] may be necessary to improve smooth muscle growth. Functional evaluations of vaginas reconstructed with BLSF and SIS biomaterials confirmed their ability to support copulation and live births thus providing evidence that these matrix configurations can reestablish organ continuity sufficient for reproduction.

Currently, patients with congenital vaginal abnormalities such as Mayer-Rokitansky-Küster-Hauser Syndrome (MRKHS) as well as male-to-female transgenders require the creation of tubular neovaginas from autologous tissues to restore sexual function.[21] Decellularized tissues grafts such as SIS have been previously explored as an biomaterial substitutes for tubular vaginoplasty in MRKHS individuals, however suboptimal outcomes including relatively short neovaginas (<7 cm for 46.4% of patients), excessive vaginal discharge and chronic bacterial infections were observed.[22] Moreover,

preclinical assessments of decellularized tissue matrices for tubular vaginoplasty have also noted frequent graft contracture and luminal collapse in rodent neovaginas.[23] BLSF matrices possess a number of potential advantages relative to decellularized tissue biomaterials for the design of tubular implants for vaginoplasty. In particular, the mechanical, structural and degradative properties of BLSF scaffolds can be adjusted by manipulating processing parameters such as porogen size and silk fibroin content to create constructs with biomechanical features sufficient for maintaining hollow organ integrity.[24-26] Indeed, these matrix configurations have been previously reported to serve as urinary conduits[27] as well as facilitate functional repair of tubular defects in both the ureter and esophagus.[15,28] In contrast, the physical characteristics of decellularized tissue grafts are dependent upon the attributes of the source tissue as well as decellularization protocols[29] and therefore have limited capacity to modulate structural integrity to prevent stenotic events. Future in vivo studies will investigate the efficacy of tubular BLSF grafts for neovagina formation.

4.5 References

1) Fontana, L et al. “Genetics of Mayer-Rokitansky-Küster-Hauser (MRKH) syndrome.” Clinical genetics vol. 91,2 (2017): 233-246. doi:10.1111/cge.12883

2) Kamal, El Moussaoui et al. “Management of a transverse vaginal septum complicated with hematocolpos in an adolescent girl: Case report.” International journal of surgery case reports vol. 77 (2020): 748-752. doi:10.1016/j.ijscr.2020.11.098

3) Fei, Y Frances et al. “Distal Vaginal Atresia with Spontaneous Perforation: A Case Report.” Journal of pediatric and adolescent gynecology vol. 35,3 (2022): 383-386. doi:10.1016/j.jpag.2021.10.018

4) Raya-Rivera, Atlántida M et al. “Tissue-engineered autologous vaginal organs in patients: a pilot cohort study.” Lancet (London, England) vol. 384,9940 (2014): 329-36. doi:10.1016/S0140-6736(14)60542-0

5) Edmonds, D Keith. “Congenital malformations of the genital tract and their management.” Best practice & research. Clinical obstetrics & gynaecology vol. 17,1 (2003): 19-40. doi:10.1053/ybeog.2003.0356

6) Ismail-Pratt, Ida S et al. “Normalization of the vagina by dilator treatment alone in Complete Androgen Insensitivity Syndrome and Mayer-Rokitansky-Kuster-Hauser Syndrome.” Human reproduction (Oxford, England) vol. 22,7 (2007): 2020-4. doi:10.1093/humrep/dem074

7) Liao, L- M et al. “Dilation as treatment for vaginal agenesis and hypoplasia: a pilot exploration of benefits and barriers as perceived by patients.” Journal of obstetrics and gynaecology : the journal of the Institute of Obstetrics and Gynaecology vol. 26,2 (2006): 144-8. doi:10.1080/01443610500443527

8) Liao, L- M et al. “Dilation as treatment for vaginal agenesis and hypoplasia: a pilot exploration of benefits and barriers as perceived by patients.” Journal of obstetrics and gynaecology : the journal of the Institute of Obstetrics and Gynaecology vol. 26,2 (2006): 144-8. doi:10.1080/01443610500443527

9) Ferrando, Cecile A. “Vaginoplasty Complications.” Clinics in plastic surgery vol. 45,3 (2018): 361-368. doi:10.1016/j.cps.2018.03.007

10) Davies, Melissa C et al. “The pitfalls of vaginal construction.” BJU international vol. 95,9 (2005): 1293-8. doi:10.1111/j.1464-410X.2005.05522.x

11) Peng, Wei et al. “Review of Plastic Surgery Biomaterials and Current Progress in Their 3D Manufacturing Technology.” Materials (Basel, Switzerland) vol. 13,18 4108. 16 Sep. 2020, doi:10.3390/ma13184108

12) Raya-Rivera, Atlántida M et al. “Tissue-engineered autologous vaginal organs in patients: a pilot cohort study.” Lancet (London, England) vol. 384,9940 (2014): 329-36. doi:10.1016/S0140-6736(14)60542-0

13) Seth A, Chung YG, Gil ES, Tu D, Franck D, Di Vizio D, et al. The performance of silk scaffolds in a rat model of augmentation cystoplasty. Biomaterials. 2013;34:4758-65.

14) Affas S, Schäfer FM, Algarrahi K, Cristofaro V, Sullivan MP, Yang X, et al. Augmentation Cystoplasty of Diseased Porcine Bladders with Bi-Layer Silk Fibroin Grafts. Tissue Eng Part A. 2019;25:855-66

15) Gundogdu G, Okhunov Z, Cristofaro V, Starek S, Veneri F, Orabi H, et al. Evaluation of Bi-Layer Silk Fibroin Grafts for Tubular Ureteroplasty in a Porcine Defect Model. Front Bioeng Biotechnol. 2021;9:723559.

16) McCracken JM, Calderon GA, Robinson AJ, Sullivan CN, Cosgriff-Hernandez E, Hakim JCE. Animal Models and Alternatives in Vaginal Research: a Comparative Review. Reprod Sci. 2021;28:1759-73.

17) Parsons JK, Tufaro A, Chang B, Schoenberg MP. Rectus abdominis vaginoplasty after anterior exenteration for urologic malignancy. Urology. 2003;61:1249-52.

18) Thomas JC, Brock JW 3rd. Vaginal substitution: attempts to create the ideal replacement. J Urol. 2007;178:1855-59.

19) Committee on Practice Bulletins–Obstetrics. ACOG practice bulletin no. 198: prevention and management of obstetric lacerations at vaginal delivery. Obstet Gynecol. 2018;132:e87-e102.

20) Wang Y, Wu T, Zhang J, Feng Z, Yin M, Mo X. A bilayer vascular scaffold with spatially controlled release of growth factors to enhance in situ rapid endothelialization and smooth muscle regeneration, Materials & Design, 2021; Volume 204, 109649, ISSN 0264-1275.

21) Sueters J, Groenman FA, Bouman MB, Roovers JPW, de Vries R, Smit TH, et al. Tissue Engineering Neovagina for Vaginoplasty in Mayer-Rokitansky-Küster- Hauser Syndrome and Gender Dysphoria Patients: A Systematic Review. Tissue Eng Part B Rev. 2023;29:28-46.

22) Ding JX, Chen LM, Zhang XY, Zhang Y, Hua k. Sexual and functional outcomes of vaginoplasty using acellular porcine small intestinal submucosa graft or laparoscopic peritoneal vaginoplasty: A comparative study. Hum Reprod 2015;30:581–9.

23) Ding JX, Chen LM, Zhang XY, Zhang Y, Hua k. Sexual and functional outcomes of vaginoplasty using acellular porcine small intestinal submucosa graft or laparoscopic peritoneal vaginoplasty: A comparative study. Hum Reprod 2015;30:581–9.

24) Ding JX, Chen LM, Zhang XY, Zhang Y, Hua k. Sexual and functional outcomes of vaginoplasty using acellular porcine small intestinal submucosa graft or laparoscopic peritoneal vaginoplasty: A comparative study. Hum Reprod 2015;30:581–9.

25) Ding JX, Chen LM, Zhang XY, Zhang Y, Hua k. Sexual and functional outcomes of vaginoplasty using acellular porcine small intestinal submucosa graft or laparoscopic peritoneal vaginoplasty: A comparative study. Hum Reprod 2015;30:581–9.

26) Tu DD, Chung YG, Gil ES, Seth A, Franck D, Cristofaro V, et al. Bladder tissue regeneration using acellular bi-layer silk scaffolds in a large animal model of augmentation cystoplasty. Biomaterials. 2013;34:8681-8689.

27) Gundogdu G, Nguyen T, Hosseini Sharifi SH, Starek S, Costa K, Jones CE, et al. Evaluation of silk fibroin-based urinary conduits in a porcine model of urinary diversion. Front Bioeng Biotechnol. 2023;11:1100507.

28) Gundogdu G, Nguyen T, Hosseini Sharifi SH, Starek S, Costa K, Jones CE, et al. Evaluation of silk fibroin-based urinary conduits in a porcine model of urinary diversion. Front Bioeng Biotechnol. 2023;11:1100507.

29) Brown BN, Badylak SF. Extracellular matrix as an inductive scaffold for functional tissue reconstruction. Transl Res. 2014;163:268-285.

Chapter 5: Epilogue

5.1 Recapitulation

This dissertation addresses several disadvantages in conventional treatment modalities for urogenital tissue reconstruction as well as limitations in current animal models of urologic disease. The development of preclinical animal models which simulate human conditions are essential to understanding disease mechanisms and screening potential therapeutic interventions. Specifically, my thesis work has led to the creation of novel rabbit and porcine models of acute Peyronie's disease and urethra stricture disease, respectively. My research has also characterized the efficacy of BLSF scaffolds to serve as alternative substitutes for autologous tissue grafts for urinary conduit fabrication and vaginoplasty.

Future work will focus on establishing a chronic Peyronie's disease model in rabbits via optimization of dosage and frequency of fibrotic insults such as TGF-β1 in order to create a model that recapitulates clinical-based outcomes such as severe penile angulation. Porcine urethral stricture models will be used to determine the feasibility of BLSF biomaterials for long urethral stricture repair and their regenerative and functional responses will be compared to conventional buccal mucosal grafts. Finally, tubular BLSF conduits will also be evaluated in rabbit vaginoplasty models to ascertain their utility for neovagina creation.